THE RADIO AND ELECTRONIC ENGINEER

The Journal of the Institution of Electronic and Radio Engineers

FOUNDED 1925 INCORPORATED BY ROYAL CHARTER 1961

"To promote the advancement of radio, electronics and kindred subjects by the exchange of information in these branches of engineering."

VOLUME 30 OCTOBER 1965 NUMBER 4

SHORT—AND TO THE POINT

MOST engineers would personally disagree with the claims of sociologists that in this age of affluence and automation too much leisure is becoming a problem. Certainly the time which the average engineer is able to devote to keeping up with current literature in his own and associated fields is strictly limited—as are to an even greater extent the opportunities for producing technical papers. Both sides of this problem are of considerable importance and, because it is one of the functions of the Institution to promote the exchange of information on radio and electronic engineering, ways of helping to solve it have been discussed by the Papers Committee.

Many an engineer will from time to time find himself in the position of having made a small advance or engineering development in the techniques of his particular specialization—an advance perhaps so small that, apart from the time not being available, his innate modesty deters him from sitting down to produce a paper for his professional journal. Nevertheless, to hide this small light 'under the bushel' could be regarded as being both selfish and shortsighted: shortsighted because of the likelihood of arousing constructive comment from other engineers concerned with the same or similar problems, and selfish because the sharing of knowledge is one of the basic tenets of the profession.

In re-emphasizing its wish to receive short papers for publication in *The Radio and Electronic Engineer*, the Papers Committee has considered another class of short contribution which is very relevant to the *Journal*. Most short papers are complete in themselves—at least to the extent that *any* paper in these days can be independent of other published work. Often, however, a worthwhile contribution may be made by commenting upon a specific paper published previously; it is proposed that this second category should be regarded as a 'Letter to the Editor'. These letters will in effect represent written discussion on papers which may not have been read at a meeting but which are nevertheless provocative of comment, preferably constructive although well-founded criticism of theoretical statements can also be considered for publication. In both these broad groups it is intended to ensure rapid publication by simplifying the refereeing procedure and Committee consideration which is necessary for full papers.

Similar short articles are invited for consideration for publication in the *Proceedings* of the I.E.R.E., as well as 'Letters to the Editor' commenting on papers and articles which have appeared within its pages. This kind of short contribution and letter will similarly be invited by the Editors of the Institution's Divisional *Proceedings*.

An essential feature of all these contributions, to *Journal* and *Proceedings*, will be brevity. For just as time is at a premium when writing a paper, so also is it even more important where the time of thousands of engineers is involved in reading about developments in fields other than their own immediate interests. The guiding principle will be that they should be short and to the point! Both members and non-members are therefore cordially invited to submit suitable material.

A. G. W.

INSTITUTION NOTICES

Symposium on "Electronics, Measurement and Control in Ships and Shipbuilding"

Information and registration forms are now ready for the Symposium on "Electronics, Measurement and Control in Ships and Shipbuilding", which is being organized by the Scottish Section of the Institution and the Scottish Electronics and Control Section of the Institution of Electrical Engineers, in collaboration with the Institution of Engineers and Shipbuilders in Scotland.

The Symposium will open on Tuesday, 12th April and will last until Friday, 15th April 1966. Sessions, some of which will take place concurrently, will deal with shipbuilding, navigation, data logging, cargo handling, propulsion and ship management.

The Symposium will be held at the University of Strathclyde, Glasgow, and there will be residential accommodation in one of the University's Halls of Residence.

Further information may be obtained from the Joint Organizing Secretaries: K. A. Murphy, A.M.I.E.E., A.M.I.E.R.E., 50 Holeburn Road, Newlands, Glasgow, S.3; and R. D. Pittilo, A.M.I.E.R.E., 35 Crawfurd Road, Burnside, Rutherglen, Glasgow.

Conference on "Applications of Thin Films in Electronic Engineering"

A four- to five-day international conference on the above theme is being organized by the Institution in conjunction with the Institution of Electrical Engineers, to take place at the Imperial College of Science and Technology, University of London, between 11th and 15th July 1966.

It is intended to deal with the subject in depth and each group of papers will be preceded by a keynote or review paper. The Joint Organizing Committee, which is under the chairmanship of Professor J. C. Anderson, will welcome offers of papers dealing with the following or associated topics:

Preparation of Thin Films

The keynote paper will review current methods of thin film preparation with special emphasis on those appropriate for large scale production processes. Contributed papers will be expected to deal with thin film production processes, including electron beam machining, although papers on new techniques only at the laboratory stage are acceptable.

Thin Film Elements and Integrated Circuits

The keynote paper will review the applications for integrated thin film circuits emphasizing the advantages offered in terms of cheapness, reliability and versatility. It will review the present status of techniques. Contributed papers will cover (*a*) passive circuit elements such as capacitors and resistors, (*b*) progress in the development of active elements, especially the thin film field effect transistor, (*c*) complete circuits.

Computer Applications

(*a*) *Magnetic Films.* The review paper will cover storage and switching properties of magnetic films, covering problems like creep, ageing, partial switching and the like. Contributions will cover practical applications, including actual computer memory stores.

(*b*) *Cryogenic Films.* The review paper will cover the basic principles of superconductivity and their application to thin films and will discuss the merits of the cryogenic storage element. Contributed papers will necessarily be on present research, there being no important successful applications as yet.

Other Applications

Contributions in this group would include, for example: magnetoresistive films as strain gauges; thermoelectric thin film devices; luminescence in thin films; space charge limited currents in dielectric thin films; hybrid thin-film/semiconductor circuits.

Offers of papers, which should be accompanied by a synopsis, should be sent to: The Secretary, Joint Conference on Thin Films, I.E.R.E., 8–9 Bedford Square, London, W.C.1. Synopses should be about 200 words in length and are requested to be submitted by 30th November (31st December from intending contributors outside Great Britain).

International Conference on U.H.F. Television

The Joint Conference on "U.H.F. Television" sponsored by the I.E.R.E., the Institution of Electrical Engineers (Electronics Division), the Institute of Electrical and Electronics Engineers (United Kingdom and Eire Section) and the Television Society, takes place on 22nd and 23rd November 1965 at the I.E.E., Savoy Place, London, W.C.2. The outline programme is given on page xiii of this issue and application forms and fuller details, including particulars of visits being arranged in conjunction with the Conference, may be obtained from The Joint Conference Secretariat, I.E.R.E., 8–9 Bedford Square, London, W.C.1.

Canadian Division

Members in the United States and Canada are advised that correspondence on Institution matters should be addressed to the I.E.R.E. office in Ottawa. The address is:

The Institution of Electronic and Radio Engineers,
504 Royal Trust Building, Albert Street,
Ottawa, Ontario.

U.D.C. 621.372.853.1

Dielectric Loaded Waveguides—a Review of Theoretical Solutions

Part II: Propagation Through Dielectric Loaded Waveguides†

By

S. K. CHATTERJEE, M.Sc.‡

AND

(Mrs.) R. CHATTERJEE, Ph.D., M.S.E., M.Sc.‡

Summary: The paper presents an analytical survey of the propagation characteristics of microwaves through (i) dielectric loaded waveguides, such as parallel plane, rectangular, circularly cylindrical and coaxial guides filled inhomogeneously with one or two dielectrics; (ii) imperfect waveguides filled with imperfect dielectrics. The problem of the existence of backward waves in a circular cylindrical waveguide containing a concentric dielectric rod of smaller radius than the guide and the representation of equivalent circuit of a waveguide containing a dielectric post has also been discussed. A brief review of the theory of dielectrics has been included in the appendix.

7. Introduction

Waveguides suitably loaded with dielectrics having high dielectric constant and low loss, when compared to unloaded hollow waveguides offer certain advantages such as the reduction of phase velocity of an electromagnetic wave in a waveguide, etc. Theoretical analysis of wave propagation in dielectric loaded waveguides has been made by several authors[12-55,147] by using one of the mathematical methods outlined in Part I of this paper.† A survey of the theoretical results concerning the properties of dielectric loaded guides is presented below. In some cases, it has been considered worthwhile to present some significant mathematical steps leading to final results in order to enable a proper understanding of the application of the different mathematical methods discussed in Part I.

8. Parallel Plane Waveguide Partially Filled with Dielectric

The propagation characteristics of microwave in a dielectric loaded parallel plane waveguide have been studied by Cohn[39, 41, 118] by following the field theory approach. Due to the symmetry of the structure (Fig. 2), the solutions may be classified as even and odd modes, denoted by the subscripts "e" and "o" respectively. Treating this as a boundary value problem and using the field components,[34] the following characteristic equations have been obtained

$$\pi^2\left(\frac{2a}{\lambda_0}\right)^2(k_{e1}-k_{e2}) = \left(\frac{k_{1e}a}{\cos k_{1e}a}\right)^2$$

for the even-order modes .....(72)

and

$$\pi^2\left(\frac{2a}{\lambda_0}\right)^2(k_{e1}-k_{e2}) = \left(\frac{k_{1o}a}{\sin k_{1o}a}\right)^2$$

for the odd-order modes .....(73)

where

$$k_{1e}^2-\omega^2\mu_0\varepsilon_1 = -k_{2e}^2-\omega^2\mu_0\varepsilon_2$$
$$k_{1o}^2-\omega^2\mu_0\varepsilon_1 = -k_{2o}^2-\omega^2\mu_0\varepsilon_2 \quad .....(74)$$
$$k_{e1} = \varepsilon_1/\varepsilon_0 \qquad k_{e2} = \varepsilon_2/\varepsilon_0$$
$$\lambda_0 = \text{free space wavelength.}$$

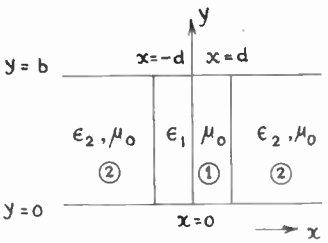

Fig. 2. Dielectric loaded parallel plane waveguide. (Ref. 41.)

The roots of the above eqns. (72) and (73), which can be obtained by graphical solution, yield the values of k_{1e} and k_{1o}. The propagating modes supported by this structure are designated as H_{m0}. The dominant mode H_{10} corresponds to $m = 1$. It is also found from the above equations that the condition for the H_{m0} mode to propagate in this structure is

$$\frac{2a}{\lambda_0} > \frac{m-1}{2\sqrt{\Delta k_e}} \quad .....(75)$$

where $\Delta k_e = k_{e1}-k_{e2}$. Figures 3 and 4 show the variation of the inner transverse distribution parameter $k_{1e}a$ and the outer transverse distribution parameter $k_{2e}a$ respectively as functions of the normalized slab width $2a/\lambda_0$ for different values of the

† Part I of this paper was published in the September issue of *The Radio and Electronic Engineer* (30, No. 3, pp. 145–60). References will be found at the end of Part III of the paper.

‡ Department of Electrical Communication Engineering, Indian Institute of Science, Bangalore, India.

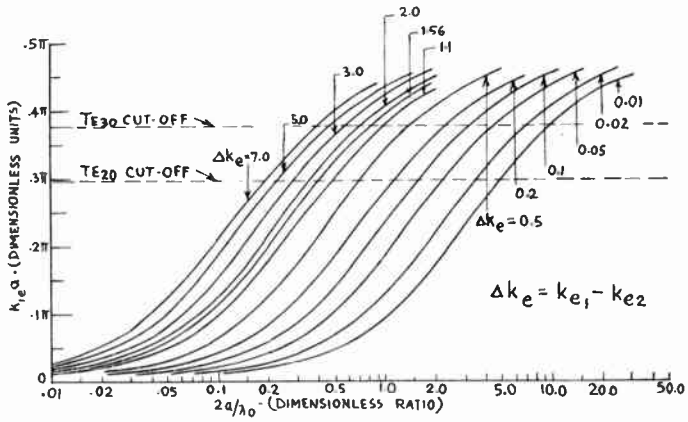

Fig. 3. Inner transverse distribution parameter ($k_{1e}a$) of the dominant mode as a function of the normalized dielectric slab width. (Ref. 41.)

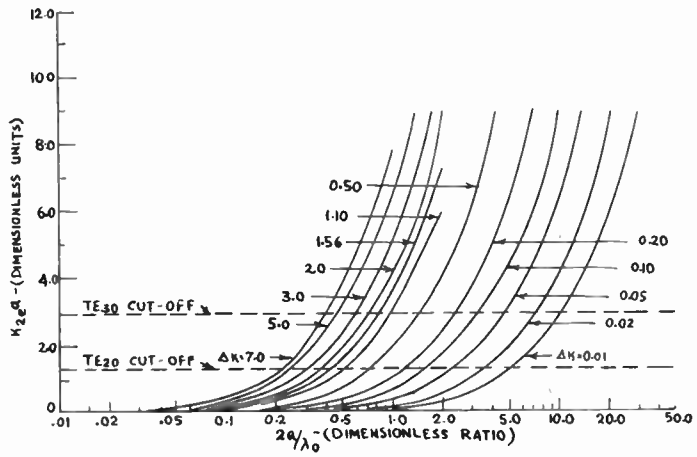

Fig. 4. Outer transverse distribution parameter ($k_{2e}a$) as a function of $2a/\lambda_0$ for different values of Δk_e. (Ref. 41.)

difference of dielectric constants Δk_e's for the dominant mode H_{10}. The cut-off loci for some of the higher-order modes are shown by dotted lines.

It has been found by Tischer[28] that TEM and TM modes cannot propagate in such a guide, although HE modes can be supported by such a structure. The field components for the H_{m0} modes are independent of the transverse coordinate y. So the guide wavelength λ_g and cut-off wavelength λ_c for the H_{m0} modes are independent of the distance b. Hence, by a proper adjustment of the distance between the two conducting plates of the guide, the HE modes can be suppressed without affecting the propagating modes H_{m0}. The cut-off condition for the HE mode is

$$\frac{b_c}{\lambda_0} = \frac{1}{2}\left[\frac{1+\tan^2 k_{1e}a}{1+k_{e1}\tan^2 k_{1e}a}\right]^{\frac{1}{2}} \qquad \text{.....(76)}$$

where the critical distance between the plates at cut-off is $b = b_c$. This shows that only H_{m0} modes will propagate in this structure if $b < b_c$. It has been shown by Tischer[35] that only the dominant mode H_{10} will propagate in this structure if the following inequality is satisfied

$$\frac{2a}{\lambda_0} < \frac{1}{2\sqrt{\Delta k_e}} \qquad \text{.....(77)}$$

in addition to the inequality $b < b_c$. The cut-off normalized height (b_c/λ_0) of the guide for the hybrid modes as a function of $2a/\lambda_0$ and k_{e1} is shown in Fig. 5. Using the relations[41]

$$\beta^2 = -k_1^2 + \omega_0\mu_0\varepsilon_1 \quad \text{and} \quad \lambda_g = 2\pi/\beta \qquad \text{.....(78)}$$

it has been shown by Cohn[41] that the normalized guide wavelengths for the even and odd H_{m0} modes are given respectively by the following relations[41]

$$\frac{\lambda_g}{\lambda_0} = \frac{\pi(2a/\lambda_0)}{[\pi^2(2a/\lambda_0)^2 k_{e1} - (k_{1e}a)^2]^{\frac{1}{2}}} \qquad \text{.....(79)}$$

$$\frac{\lambda_g}{\lambda_0} = \frac{\pi(2a/\lambda_0)}{[\pi^2(2a/\lambda_0)^2 k_{e1} - (k_{1o}a)^2]^{\frac{1}{2}}} \qquad \text{.....(80)}$$

For $k_{e2} = 1$, λ_g/λ_0 is plotted against $2a/\lambda_0$ in Fig. 6. The cut-off loci for the higher-order H modes are shown by the dashed curves.

By calculating the power flow for the even and odd modes with the help of the Poynting vector and proper field components and by assuming the maximum breakdown electric field E_{bd} at $x = 0$ as $E_{bd} = 15\,000$ volts per cm, the breakdown power level P_{bd} of the dominant mode is given by the following relation[41]

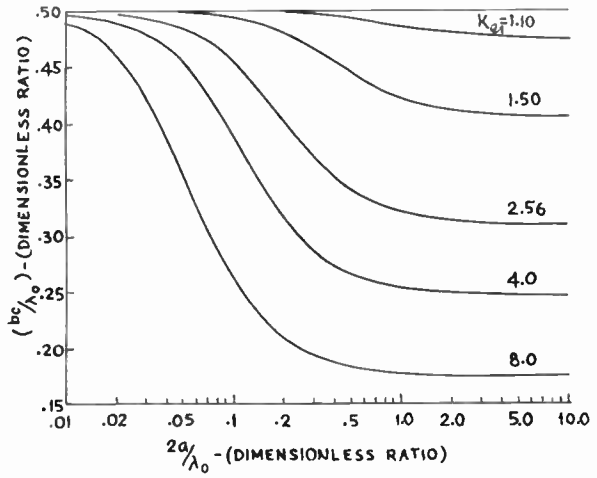

Fig. 5. Cut-off condition for the hybrid mode as a function of the normalized dielectric slab width. (Ref. 41.)

$$\frac{P_{bd}}{ab} = \frac{9{\cdot}51 \times 10^8}{2a/\lambda_0}\left[1 + \frac{\cot k_{1e}a}{k_{1e}a}\right] \times \times \left[\pi^2 k_{e1}\left(\frac{2a}{\lambda_0}\right)^2 - (k_{1e}a)^2\right]^{\frac{1}{2}} \quad \text{.....(81)}$$

The variation of P_{bd}/ab as a function of $2a/\lambda_0$ for different values of k_{e1} and for $k_{e2} = 1$ is shown in Fig. 7.

It is concluded that:

(i) As the dominant mode H_{10} has no cut-off wavelength, the structure can be used for broad-band operation.

(ii) TEM and TM modes cannot be supported by this structure.

(iii) The size of the structure needed in the x-direction for the power handling capacity given by eqn. (81), is larger than is required for a conventional rectangular unloaded guide. This makes the dielectric loaded parallel plane guide more convenient for millimetre wave work than a conventional hollow tube guide.

(iv) The losses are comparable to the losses suffered by the wave in propagating through a hollow rectangular waveguide (Sect. 14.2).

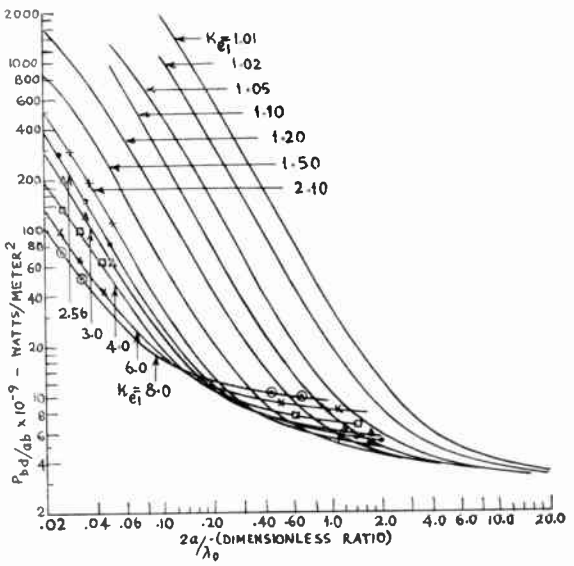

Fig. 7. Breakdown power level of the dominant mode H_{10} as a function of the normalized dielectric slab width. (Ref. 41.)

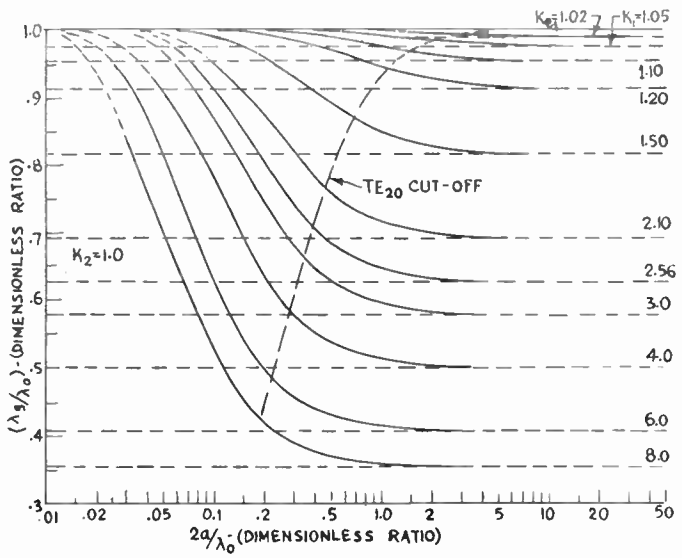

Fig. 6. Guide wavelength for the H mode as a function of the normalized slab width. (Ref. 41.)

9. Rectangular Guide Partially Filled with Dielectric

The theoretical treatment of problems of this nature involves the matching of fields which satisfy Maxwell's equations in the various media at the interfaces between them. In general, the modes are of complex nature and transcendental equations have to be solved in order to determine the propagation constants of the various modes. It is only when[13] the field does not vary along the interface between any two dielectrics that it is possible for the guide to transmit a pure H or E mode. Unless this condition of symmetry is satisfied, the mode transmitted will be a mixed one having longitudinal components of both electric and magnetic fields. Several typical cases which illustrate the application of the different methods of approach are discussed below.

9.1. *Dielectric Slab placed at the Centre of the Guide*

If the propagation is considered to be in the x-direction, an equivalent circuit for the guide (Fig. 8) may be considered to consist of two transmission lines shorted at one end and joined at the centre of the dielectric. If the guide is excited by the lowest H wave the electric field at the centre of the guide ($x = a/2$) is maximum. The admittance looking from the centre of the guide in the x-direction is obtained by following the conventional transmission line theory approach and is given by the following relation[98]

$$Y_{in} = Y_0^{(2)} \frac{jY_0^{(1)} \tan\left(x_1 \frac{d-a}{2}\right) + jY_0^{(2)} \tan\left(x_2 \frac{d}{2}\right)}{Y_0^{(2)} + jY_0^{(1)} \tan\left(x_1 \frac{d-a}{2}\right)} \qquad \text{.....(82)}$$

where, $Y_0^{(1)}$ and $Y_0^{(2)}$ represent the characteristic admittances of medium 1 (air) and medium 2 (dielectric slab) respectively and

$$x_1 = 2\pi\sqrt{\left(\frac{1}{\lambda_0}\right)^2 - \left(\frac{1}{\lambda_g}\right)^2}$$

$$x_2 = 2\pi\sqrt{k_e\left(\frac{1}{\lambda_0}\right)^2 - \left(\frac{1}{\lambda_g}\right)^2} \qquad \text{.....(83)}$$

$$\frac{Y_0^{(1)}}{Y_0^{(2)}} = \frac{x_1}{x_2}$$

The transverse resonance condition is obtained when $Y_{in} = 0$ which with the help of eqn. (83) yields the following characteristic equation

$$x_1 \tan\left(x_1 \frac{d-a}{2}\right) = -x_2 \tan\left(x_2 \frac{d}{2}\right) \qquad \text{.....(84)}$$

The variation of the guide wavelength with respect to the normalized slab width (d/a) can be studied with the help of eqn. (84).

The propagation characteristics of an electromagnetic wave in such a structure has also been studied by using the variational principle which has been discussed in Part I, section 6.3.2. The procedure is as follows. The cut-off frequency of the guide is calculated by regarding the guide as a two-dimensional resonator. The resonant frequency of the inhomogeneous guide is expressed as a variational integral. The field inside the guide is then expressed as a sum of the true (unperturbed) field **E** and an error field **e** as

$$\mathbf{E}_{trial} = \mathbf{E}_{true} + s\mathbf{e} \qquad \text{.....(85)}$$

where s is an arbitrary parameter. The permissible trial field is substituted in the variational integral. The resonant frequency is found by expressing ω as a function of s for a fixed value of **e** as

$$\omega^2(s) = \omega_r^2 + s\left.\frac{\partial \omega^2}{\partial s}\right|_{s=0} + \frac{s^2}{2!}\left.\frac{\partial^2 \omega^2}{\partial s^2}\right|_{s=0} + \ldots \qquad \text{.....(86)}$$

or in variational notation

$$\omega^2(s) = \omega_r^2 + \delta\omega^2 + \delta^2\omega^2 + \ldots \qquad \text{.....(87)}$$

where $\omega_r^2 = \omega^2(0)$ represents the true resonant frequency of the homogeneous cavity. The stationary character of the variational integral is proved by setting

$$\left.\frac{\partial \omega^2}{\partial s}\right|_{s=0} = 0 \qquad \text{.....(88)}$$

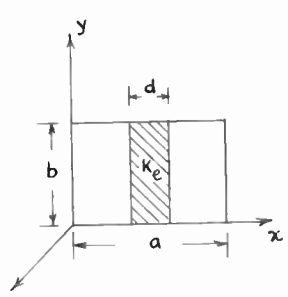

Fig. 8. Dielectric slab placed at the centre of a rectangular guide.

If

$$\mathscr{E} = \mathscr{E}(x, y) \exp(-j\gamma z)$$

and $\qquad \text{.....(89)}$

$$\mathscr{H} = \mathscr{H}(x, y) \exp(-j\gamma z)$$

represent three-dimensional field vectors depending on x and y only and satisfy the relations

$$\begin{aligned} \text{curl}\,\mathscr{E} + j\omega\mu\mathscr{H} &= j\gamma \mathbf{i}_z \times \mathscr{E} \\ \text{curl}\,\mathscr{H} - j\omega\varepsilon\mathscr{E} &= j\gamma \mathbf{i}_z \times \mathscr{H} \end{aligned} \qquad \text{.....(90)}$$

the expression for γ in variational form as derived from (90) for E-field formulation is given by the relation[119]

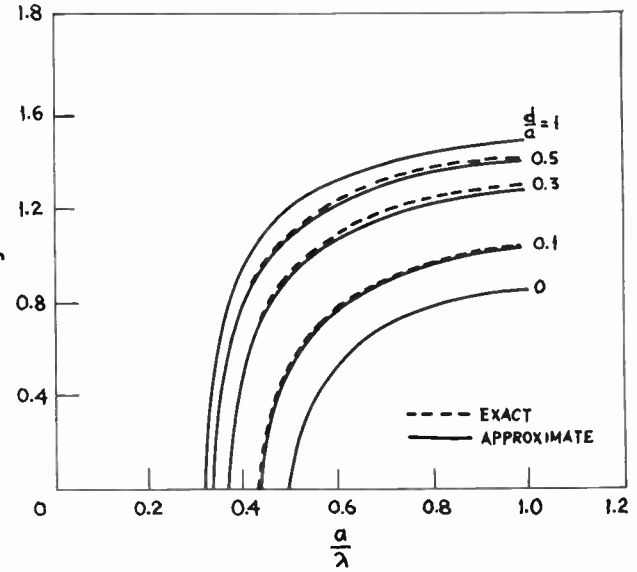

Fig. 9. Guide wavelength as a function of the dielectric slab width. Comparison with the results obtained by field theory. (Ref. 119.)

$$\gamma^2 \int (\mathbf{i}_z \times \mathscr{E}^*).\mu^{-1}.(\mathbf{i}_z \times \mathscr{E})ds - j\gamma \int [(\text{curl } \mathscr{E}^*).\mu^{-1}.(\mathbf{i}_z \times \mathscr{E}) - (\mathbf{i}_z \times \mathscr{E}^*).\mu^{-1}.(\text{curl } \mathscr{E})]ds + \int (\text{curl } \mathscr{E}^*).\mu^{-1}.(\text{curl } \mathscr{E})ds - \omega^2 \int \mathscr{E}^*. \times .e\mathscr{E}\, ds = 0 \quad \text{.....(91)}$$

γ is stationary provided $\mathscr{E}$ and $\mathscr{E}^*$ satisfy the relation

$$\gamma^2 \mathbf{i}_z \times (\mu^{-1}.\mathbf{i}_z \times \mathscr{E}) + j\gamma[\text{curl } (\mu^{-1}.\mathbf{i}_z \times \mathscr{E}) + \mathbf{i}_z \times (\mu^{-1}.\text{curl } \mathscr{E})] - \text{curl } (\mu^{-1}.\text{curl } \mathscr{E}) + \omega^2 \varepsilon.\mathscr{E} = 0 \quad \text{.....(92)}$$

and its conjugate. Using the variational expression (92) and the trial field

$$\mathbf{E}_{\text{trial}} = \mathbf{i}_y \sin\left(\frac{\pi x}{a}\right) \quad \text{.....(93)}$$

the expression for the guide wavelength λ_g is obtained and is given as follows[119]

$$\left(\frac{\lambda_0}{\lambda_g}\right)^2 = 1 + (k_e - 1)\left[\frac{d}{a} + \frac{1}{\pi}\sin\frac{\pi d}{a}\right] - 0{\cdot}25\left(\frac{a}{\lambda}\right)^{-2} \quad \text{.....(94)}$$

The variation of λ_0/λ_g vs a/λ_0 for dielectric slabs of various normalized widths d/a is shown in Fig. 9.

The problem has also been studied by the field theory approach. The characteristic equations are as follows[98]

$$\frac{k_{x1}}{\mu_1}\cot\left(k_{x1}\frac{a-d}{2}\right) = \frac{k_{x2}}{\mu_2}\tan\left(k_{x2}\frac{d}{2}\right) \quad \text{.....(95)}$$

for the H waves and

$$\frac{k_{x1}}{\varepsilon_1}\tan\left(k_{x1}\frac{a-d}{2}\right) = \frac{k_{x2}}{\varepsilon_2}\cot\left(k_{x2}\frac{d}{2}\right) \quad \text{.....(96)}$$

for the E waves, where,

$$k_{x1}^2 + \left(\frac{n\pi}{b}\right)^2 + k_z^2 = k_0^2 = \omega^2\mu_0\varepsilon_0$$

$$k_{x2}^2 + \left(\frac{n\pi}{b}\right)^2 + k_z^2 = k_2^2 = \omega^2\mu_2\varepsilon_2$$

$$\mu_1 = \mu_0, \quad \varepsilon_1 = \varepsilon_0, \quad k_{x1} = k_{x0}$$

The propagation constants and hence the guide wavelengths as a function of the normalized width d/a of the dielectric slab can be determined from the above characteristic equations. For the dominant mode $n = 0$, the results obtained by the variational and field theory methods are compared in Fig. 9.

The same problem has been treated by Collin and Vaillancourt[120] and also Chambers[31] by Rayleigh-Ritz method. The propagation constant is determined from the matrix eigenvalue equation

$$\sum_{n=1,\,3} a_{nj}(T_{nj} - \gamma^2\delta_{nj}) = 0; \quad j = 1, 3 \quad \text{.....(97)}$$

subject to the normalization condition

$$\sum_{1,\,3} a_{nj}^2 = 1; \quad = 1, 3 \quad \text{.....(98)}$$

The propagation constants γ_j^2 are the roots of the determinant of the coefficients a_{nj} in the above matrix equation, where the matrix elements are given by

$$T_{11} = \left(\frac{\pi}{a}\right)^2 - k_0^2 - (k_e - 1)k_0^2\left(\frac{d}{a} + \frac{1}{\pi}\sin\frac{\pi d}{a}\right)$$

$$T_{13} = (k_e - 1)k_0^2\left(\frac{1}{\pi}\sin\frac{\pi d}{a} + \frac{1}{2\pi}\sin\frac{2\pi d}{a}\right) \quad \text{.....(99)}$$

$$T_{33} = \left(\frac{3\pi}{a}\right)^2 - k_0^2 - (k_e - 1)k_0^2\left(\frac{d}{a} + \frac{1}{3\pi}\sin\frac{3\pi d}{a}\right)$$

9.2. *Dielectric Slab placed at One Side of the Guide*

If the inhomogeneous guide (Fig. 10) is excited by LSE mode, the eigenfunction ψ_h is given by the relation[121]

$$\psi_h = \begin{cases} A \sin kx \cos\dfrac{m\pi y}{b}, & 0 \leqq x < (a-d) \\ B \sin l(a-x) \cos\dfrac{m\pi y}{b}, & (a-d) < x < a \end{cases} \quad \text{.....(100)}$$

ψ_h satisfies the scalar Helmholtz equation

$$\nabla^2\psi + k^2\psi = 0$$

where

$$\gamma^2 = l^2 + \left(\frac{m\pi}{b}\right)^2 - k_e k_o^2 = k^2 + \left(\frac{m\pi}{b}\right)^2 - k_0^2 \quad \text{.....(101)}$$

If the propagation takes place along the z direction according to $\exp(-\gamma z)$ then the tangential components of the electric and magnetic fields given by

$$E_z = j\omega\mu_0 \frac{\partial\psi_h}{\partial y} \exp(-\gamma z)$$
$$H_y = \frac{\partial^2\psi_h}{\partial y\,\partial x} \exp(-\gamma z) \quad \text{.....(102)}$$

must be continuous along the interface of the two media at $x = a-d$. This requires that the following conditions must be satisfied

$$A \sin k(a-d) = B \sin ld$$
$$Ak \cos k(a-d) = -Bl \cos ld \quad \text{.....(103)}$$

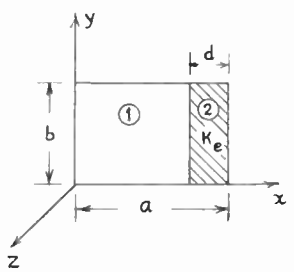

Fig. 10. Dielectric slab placed at one side of the rectangular guide.

The following eigenvalue equation is obtained from the above two relations

$$l \tan k(a-d) = -k \tan ld \quad \text{.....(104)}$$

The above equation with the following relation

$$l^2 = k^2 + (k_e - 1)\frac{4\pi^2}{\lambda_0^2} \quad \text{.....(105)}$$

yields an infinite number of solutions for l and k and hence for γ. To each pair of values of l and k corresponds a particular wave that can be labelled with the order of the corresponding root, namely LSE_{mn}.

If the guide is excited by LSM modes, proper solutions for ψ_e which will satisfy the scalar Helmholtz equation and boundary conditions are

$$\psi_e = \begin{cases} A \cos kx \sin \dfrac{m\pi y}{b}, & 0 \leqq x \leqq a-d \\ B \cos l(a-x) \sin \dfrac{m\pi y}{b} & (a-d) \leqq x \leqq a \end{cases} \quad \text{.....(106)}$$

From the continuity of the tangential components at $x = a - d$, the following characteristic equations are obtained

$$Ak \sin k(a-d) = -Bl \sin ld$$
$$A \cos k(a-d) = k_e B \cos ld \quad \text{.....(107)}$$

which yield the following eigenvalue equation

$$k_e k \tan k(a-d) = -l \tan ld \quad \text{.....(108)}$$

The permitted values of k and l and hence of γ can be determined from (108) and (105).

If the guide is excited by the lowest H mode, the eigenvalue equation obtained by the resonance method[98] is

$$Y_0^{(1)} \tan k_x^{(2)} d = -Y_0^{(2)} \tan k_x^{(1)}(d-a) \quad \text{.....(109)}$$

where $Y_0^{(1)}$ and $Y_0^{(2)}$ represent the characteristic admittances of the regions 1 and 2 respectively and

$$k_x^{(1)} = \left[\left(\frac{2\pi}{\lambda_1}\right)^2 - \left(\frac{2\pi}{\lambda_g}\right)^2\right]^{\frac{1}{2}}$$
$$k_x^{(2)} = \left[\frac{\varepsilon_2}{\varepsilon_1}\left(\frac{2\pi}{\lambda_1}\right)^2 - \left(\frac{2\pi}{\lambda_g}\right)^2\right]^{\frac{1}{2}} \quad \text{.....(110)}$$

λ_1 is the wavelength of a plane wave in medium 1. The variations of λ_1/λ_g with a/λ_1 for various values of d/a and particular values of k_e can be studied from eqn. (110).

Pincherle[13] has treated the case of a rectangular guide half-filled longitudinally with a dielectric slab and has discussed the characteristics of the LSE and LSM modes in such a guide. The field components in both the media are found to be sine functions of the propagation constant but with different amplitudes, so as to satisfy the boundary conditions. The ratio of the amplitudes of the field components in the two media is given in Table 3.

Table 3

Ratio of the amplitudes in the two media of higher to lower dielectric constants ($\varepsilon_2 > \varepsilon_1$)

	For E_y, E_z, H_x	For E_x, H_y, H_z
LSE waves	$\sin x/\sin y$	$-y \sin x/x \sin y$
LSH waves	$\sin x/\sin y$	$-x \sin x/y \sin y$

where

$$x = \tfrac{1}{2}k_2 a \qquad y = \tfrac{1}{2}k_1 a$$
$$k_2^2 = \gamma^2 + \omega^2\varepsilon_2\mu - \left(\frac{m\pi}{b}\right)^2 \qquad m = 0, 1, 2 \quad \text{.....(111)}$$
$$k_1^2 = \gamma^2 + \omega^2\varepsilon_1\mu - \left(\frac{m\pi}{b}\right)^2$$

The same type of guide has been studied by Berk[119] with the help of the variational principle. The variational expression for the resonant frequency of a resonator of volume v enclosing a medium of permittivity ε and permeability μ, provided ε and μ are

Hermitian, is[119]

$$\omega^2 = \frac{\int_v (\text{curl } \mathbf{E}^*).\mu^{-1}.(\text{curl } \mathbf{E})\,dv}{\int_v \mathbf{E}^*.\varepsilon.\mathbf{E}\,dv} \quad \text{.....(112)}$$

where $\mathbf{E}$ and $\mathbf{E}^*$ which render ω^2 stationary are solutions of

$$\text{curl}\,(\mu^{-1}.\text{curl } \mathbf{E}) - \omega^2 \varepsilon.\mathbf{E} = 0 \quad \text{.....(113)}$$

which has been obtained by eliminating the H-field between Maxwell's equations and its complex conjugate and having vanishing tangential components at the boundary of the guide. The trial fields used to find ω^2 must have $\mathbf{n}\times\mathbf{E} = 0$ at the boundary, be continuous together with their first derivatives and possess finite second derivatives everywhere in the cavity except at the surfaces where ε and μ are discontinuous. In such cases of discontinuity, $\mathbf{n}\times\mathbf{E}$ and $\mathbf{n}\times(\mu^{-1}\text{ curl }\mathbf{E})$ must be continuous.

Using the above variational expression (112) and the trial field

$$\mathbf{E} = \mathbf{i}_y \sin(\pi x/a)$$

the expression for the cut-off frequency ω_c and hence of λ_c ($\lambda_c^2 = 4\pi^2/\omega_c^2\mu_0\varepsilon_0$) is

$$\left(\frac{2\pi}{\lambda_c}\right)^2 = \left(\frac{\pi}{a}\right)^2 \left[1+(k_e-1)\left(\frac{d}{a}-\frac{1}{2\pi}\sin\frac{2\pi d}{a}\right)\right]^{-1} \quad \text{.....(114)}$$

The cut-off wavelengths computed from the above relation for different thickness of polystyrene slab ($k_e = 2{\cdot}45$) are compared with the values obtained by Frank[98] in Table 4.

Table 4

Cut-off wavelength of a rectangular waveguide with a dielectric slab

d/a	$\frac{a}{\lambda_c}$ (Frank[98])	$\frac{a}{\lambda_c}$ (Berk[119])
0·000	0·500	0·500
0·167	0·485	0·486
0·286	0·450	0·455
0·500	0·375	0·383
0·600	0·355	0·352
1·000	0·318	0·320

For a homogeneous guide, a knowledge of ω_c or λ_c gives the propagation constant $\gamma = \alpha + j\beta$ according to the following relation

$$\gamma = \begin{cases} j\beta = j\dfrac{2\pi}{\lambda_0}\sqrt{1-\left(\dfrac{\omega_c}{\omega}\right)^2} \\ \alpha = \dfrac{2\pi}{\lambda_c}\sqrt{1-\left(\dfrac{\omega}{\omega_c}\right)^2} \end{cases} \quad \text{.....(115)}$$

But for an inhomogeneous guide, no such simple relation exists. In such a case, the stationary formula for γ can be derived by using the reaction concept or by using the variational principle. The variational expression for γ in terms of both the $\mathbf{E}$ and $\mathbf{H}$ vectors, when both of them are arbitrary is[119]

$$\frac{[\omega\int_s \mathscr{E}^*.\varepsilon.\mathscr{E}\,ds + \omega\int_s \mathscr{H}^*.\mu.\mathscr{H}\,ds + j\int_s \mathscr{E}^*.\text{curl }\mathscr{H}\,ds - -j\int_s \mathscr{H}^*.\text{curl }\mathscr{E}\,ds - j\oint_{\text{Boundary of the Cross-Section } s} \mathbf{n}.(\mathscr{E}\times\mathscr{H}^*)\,dl]}{\int_s \mathscr{H}^*.\mathbf{i}_z\times\mathscr{E}\,ds - \int_s \mathscr{E}^*.\mathbf{i}_z\times\mathscr{H}\,ds} \quad \text{.....(116)}$$

9.3. *Dielectric Slab placed Longitudinally at the Bottom of the Guide*

By following the field theory approach, Bladel and Higgins[19] have derived the following characteristic equation which is valid for both real and imaginary values of an auxiliary variable u_i for the case of a two-dielectric layered rectangular waveguide (Fig. 11).

$$\left(\frac{k_m u_1 \tan u_1}{dk_1^2} + \frac{u_2 \tan u_2}{k_2^2(b-d)}\right)\times \times\left(\frac{k_e u_1}{k_1^2 d\tan u_1} + \frac{u_2}{k_2^2(b-d)\tan u_2}\right) + +\left(\frac{\gamma c_2 m\pi}{\omega a}\right)^2\left(\frac{1}{k_2^2}-\frac{1}{k_1^2}\right)^2 = 0 \quad \text{.....(117)}$$

where

$$u_i = \left[\left(\frac{\omega^2}{c_i^2}\right) - \gamma^2 - \left(\frac{m\pi}{a}\right)^2 l_i\right]^{\frac{1}{2}}$$
$$k_m = \mu_1/\mu_2 \qquad k_e = \varepsilon_1/\varepsilon_2 \qquad \text{.....(118)}$$
$$l_1 = d \qquad l_2 = b-d \qquad i = 1,2$$

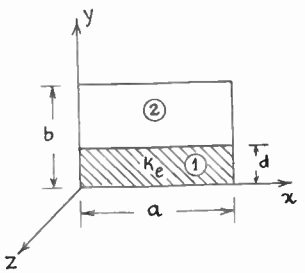

Fig. 11. Dielectric slab placed longitudinally at the bottom of the rectangular guide.

The modes represented by the above characteristic equation are classified as

(*a*) trigonometric when u_1 and u_2 are real

(*b*) single hyperbolic when u_2 is imaginary and u_1 is real

(*c*) double hyperbolic when both u_2 and u_1 are imaginary.

If $h = 0$ and $u_1 = j\omega_1$, $u_2 = j\omega_2$, where ω_1 and ω_2 are real, the characteristic eqn. (117) possesses no roots. So the double hyperbolic mode is never propagated. If

$$v_1 = \left\{\left(\frac{\omega^2}{c_1^2}\right)^2 - \gamma^2 - \left(\frac{m\pi}{a}\right)^2 d\right\}^{\frac{1}{2}}$$
$$v_2 = \left\{\left(\frac{m\pi}{a}\right)^2 + \gamma^2 - \frac{\omega^2(b-d)}{c_2^2}\right\}^{\frac{1}{2}} \quad \text{.....(119)}$$

the characteristic equations for the cut-off frequency ($\gamma = 0$) are, from eqn. (117),

$$v_2 \tanh v_2/k_2^2(b-d) - k_m v_1 \tan v_1/dk_1^2 = 0$$
and
$$v_2/k_2^2(b-d) \tanh v_2 + k_e v_1/k_1^2 d \tan v_1 = 0 \quad \text{.....(120)}$$

For $\gamma = 0$, $m = 0$, v_2 cannot be real, so no single hyperbolic mode characterized by $m = 0$ can be propagated. But for $m = 0$, trigonometric modes having $E_z = 0$ (H modes) can be propagated. The characteristic equation for the trigonometric modes with $m = 0$, $\gamma = 0$ is

$$u_1 \tan u_1 + k_e u_2 \tan u_2 = 0 \quad \text{.....(121)}$$

For $m \neq 0$, the lowest cut-off frequency (single hyperbolic) is obtained from the intersection in a (v_1, v_2) plane of the ellipse

$$[c_1 v_1/(d/b)]^2 + [c_2 v_2/(1-d/b)]^2 = \left(\frac{m\pi b}{a}\right)^2 (c_2^2 - c_1^2) \quad \text{.....(122)}$$

with the curve

$$v_1 \tan v_1 = k_e \frac{d}{b} v_2 \tanh v_2/(1-d/b) \quad \text{.....(123)}$$

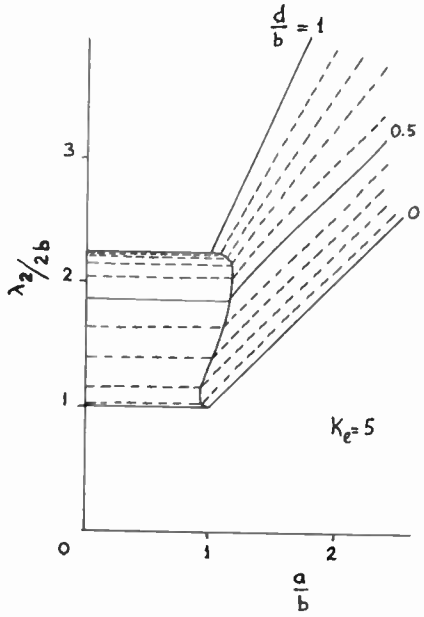

Fig. 12. Cut-off wavelength as a function of the shape factor a/b and d/b. (Ref. 19.)

Equation (122) is obtained from eqn. (119) by putting $\gamma = 0$ and eliminating ω between the two equations. It is evident that the cut-off frequency of the H mode is independent of a, but the cut-off frequency of the single hyperbolic mode ($m = 1$) which has both E_z and H_z components (EH mode) decreases with increasing values of a. So, the H mode will be the lowest mode for small values of a and the EH mode for higher values of a. The cross-over is shown in Fig. 12 for $k_m = 1$, $k_e = 5$, $d/b = 0, 0{\cdot}1, \ldots, 0{\cdot}9, 1$.

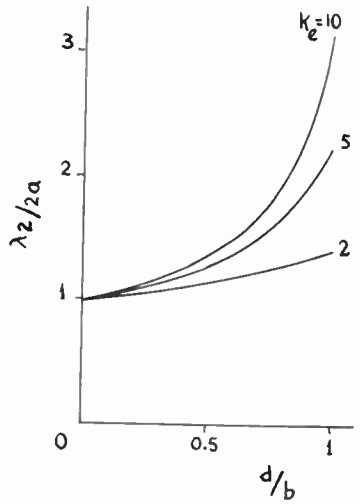

Fig. 13. Cut-off wavelength as a function of d/b when $a/b \to \infty$. (Ref. 19.)

The curves express the dependence of the general cut-off frequency measured by $\lambda_c/2b$ in terms of the shape factor a/b and d/b. The cross-over locus is a s-shaped curve, the tangents at the end-points of which are horizontal. For large values of a/b, $\lambda_c/2b$ becomes proportional to a/b, whence $\lambda_c/2b$ is independent of b. These independent values of $\lambda_c/2a$ are shown in Fig. 13.

The variational principle combined with the modal analysis and synthesis technique developed by Marcuvitz[121] has been used by Angulo[36] to study the modal spectrum for this type of structure and to derive a four-terminal network equivalent to the junction of the partially-filled guide and an empty guide. When an H_{10} mode is incident on such a structure, both LSE and LSM modes are excited and the modes are coupled. The coupling of the modes has not been taken into account in the treatment by Angulo[36] whose results are valid for $d \ll b$ or $d \simeq b$. The treatment by Collin and Vaillancourt,[120] Collin and Brown[122] takes into account the coupling of the modes and whose results are discussed below.

Considering that $k_e = k_e(y)$, the wave equation satisfied by Π is

$$\nabla^2 \Pi + k_e k_o^2 \Pi - k_e^{-1} \nabla k_e \nabla . \Pi = 0 \qquad \text{.....(124)}$$

and

$$\mathbf{E} = k_e^{-1} \nabla \times \nabla \times \Pi \qquad \text{.....(125)}$$

The solution of (124) is

$$\Pi = \mathbf{i}_y \sin \frac{\pi x}{a} \psi_e(y) \exp(\pm \gamma z)$$

assuming the x-dependence as $\sin \pi x/a$ and z-dependence as $\exp(\pm \gamma z)$. ψ_e is a solution of the Sturm-Liouville equation

$$\frac{d^2\psi_e}{dy^2} - k_e^{-1} \frac{dk}{dy} \frac{d\psi_e}{dy} + \left(k_e k_o^2 - \frac{\pi^2}{a^2} + \gamma^2\right)\psi_e = 0 \qquad \text{.....(126)}$$

which leads to the variational expression for γ^2 as

$$\gamma^2 \int_0^b k_e^{-1} \psi_e^2 \, dy - \int_0^b \left\{\left(\frac{d\psi_e}{dy}\right)^2 - \left(k_e k_o^2 - \frac{\pi^2}{a^2}\right)\psi_e^2\right\} k_e^{-1} \, dy = 0 \qquad \text{.....(127)}$$

for the LSM mode, and

$$\gamma^2 \int_0^b \psi_m^2 \, dy - \int_0^b \left\{\left(\frac{d\psi_m}{dy}\right)^2 - \left(k_e k_o^2 - \frac{\pi^2}{a^2}\right)\psi_m^2\right\} dy = 0 \qquad \text{.....(128)}$$

for the LSE mode. The kth approximate eigenvalue γ_k for the LSM mode is determined from the matrix eigenvalue equation:

$$\sum_{n=0}^{k} a_{nk}(T_{sn} - \gamma_k^2 P_{sn}) = 0, \qquad s = 0, 1, \ldots, N \qquad \text{.....(129)}$$

obtained from eqn. (127), where

$$P_{sn} = P_{ns} = \int_0^b k_e^{-1} \phi_{en} \phi_{es} \, dy \qquad \text{.....(130)}$$

and the matrix elements are

$$T_{ns} = T_{sn} = \int_0^b k_e^{-1} \left\{\frac{d\phi_{es}}{dy} \frac{d\phi_{en}}{dy} - \left(k_e k_o^2 - \frac{\pi^2}{a^2}\right)\phi_{es}^* \phi_{en}^*\right\} dy \qquad \text{.....(131)}$$

The approximate kth eigenfunction is

$$\psi_{ek} = \sum_{n=0}^{N} a_{nk} \phi_{en} \qquad \text{.....(132)}$$

For each root of γ_k^2, a solution for the coefficient a_{nk} can be obtained. This solution is unique when subjected to the normalization condition

$$\int_0^b k_e^{-1} \psi_{ek}^2 \, dy = \sum_{s=0}^{N} \sum_{n=0}^{N} a_{nk} a_{sk} P_{sn} = 1 \qquad \text{.....(133)}$$

Similarly for the LSE mode, the matrix eigenvalue equation obtained from (128) is

$$\sum_{n=1}^{k} b_{nk}(Q_{sn} - \beta_k^2 \delta_{sn}) = 0, \qquad s = 1, 2, \ldots, N \qquad \text{.....(134)}$$

where the matrix elements Q_{ns} are as follows:

$$Q_{sn} = Q_{ns} = \int_0^b \left\{\frac{d\phi_{ms}}{dy} \frac{d\phi_{mn}}{dy} - \left(k_e k_o^2 - \frac{\pi^2}{a^2}\right)\phi_{ms} \phi_{mn}\right\} dy \qquad \text{.....(135)}$$

where the Kronecker delta δ_{ns} is given by the orthonormal set

$$\delta_{ns} = \int_0^b \psi_{mn} \psi_{ms} \, dy, \qquad \delta_{ns} = \begin{cases} 1 & n = s \\ 0 & n \neq s \end{cases} \qquad \text{.....(136)}$$

and ψ_m is a solution of the equation

$$\frac{d^2\psi_m}{dy^2} + \left(k_e k_o^2 - \frac{\pi^2}{a^2} + \beta^2\right)\psi_m = 0 \quad \text{.....(137)}$$

The coefficients b_{nk} obey the normalization condition

$$\sum_{n=1}^{N} b_{nk}^2 = 1, \qquad k = 1, 2 \ldots N \quad \text{.....(138)}$$

and satisfy the orthogonality relation

$$\sum_{n=1}^{N} b_{nk} b_{nR} = 0 \qquad R \neq k \quad \text{.....(139)}$$

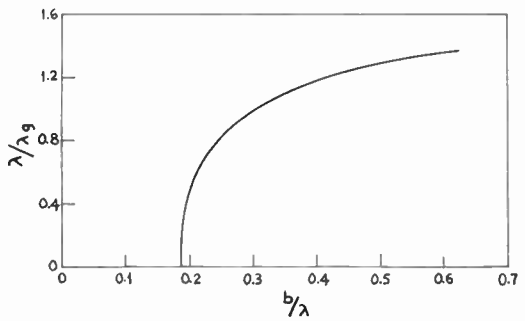

Fig. 14. Guide wavelength as a function of the normalized height of the guide. (Ref. 98.)

The case of a rectangular guide with dielectric slab placed at the bottom of the guide has also been treated by the network theory[98] and the results are shown in Figs. 14 and 15 for a guide half-full of dielectric. This case has also been treated by Pincherle.[13]

9.4. *Dielectric Slabs placed Longitudinally at the Top and the Bottom of the Guide*

By following the field theory approach, Bladel and Higgins[19] have derived the following characteristic equation for the lowest EH mode for the configuration shown in Fig. 16

$$v_1 \tanh v_2 \tan v_1/v_2 = \frac{d}{b} k_e/(1-d/b) \quad \text{.....(140)}$$

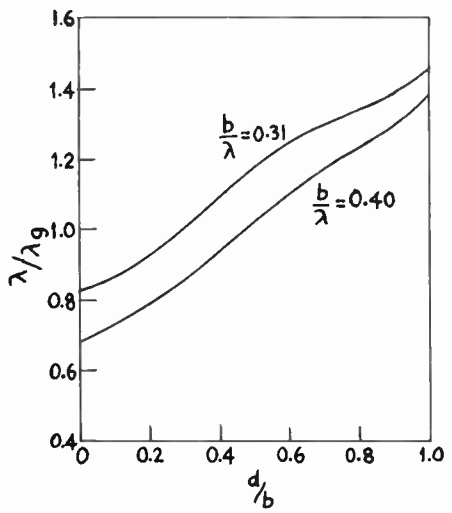

Fig. 15. Guide wavelength as a function of shape factor d/b. (Ref. 98.)

from which the variation of $\lambda_c/2b$ vs. a/b can be determined.

9.5. *Dielectric Slab placed at the Middle of the Guide*

The characteristic equation for this case (Fig. 17) is as follows[19]

$$v_1 \tanh v_2 \tan \frac{v_1}{v_2} = \frac{d}{b} k_m/(1-d/b) \quad \text{.....(141)}$$

A set of general cut-off frequency curves $\lambda_c/2b$ vs. a/b can be drawn with the help of this equation.

9.6. *Dielectric Slabs placed Longitudinally at the Two Sides of the Guide*

By matching the fields at the interface of the two media, Woodward[15] has derived a relation for the phase constant β when the guide (Fig. 18) is excited by H_{01} wave and the walls of the guide are assumed to be perfectly conducting and the dielectric to be lossless. β is found from the following relations graphically:

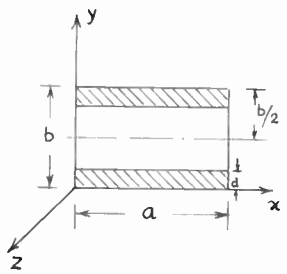

Fig. 16. Dielectric slab placed longitudinally at the top and bottom of the guide.

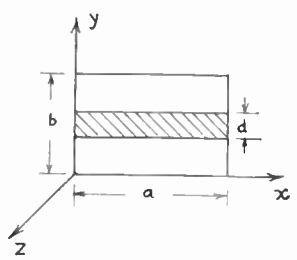

Fig. 17. Dielectric slab placed longitudinally at the middle of the guide.

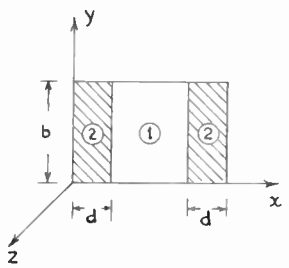

Fig. 18. Dielectric slab placed longitudinally at the two sides of the guide.

$$\frac{\sqrt{k_1^2-\beta^2}}{\mu_1}\tan\{(\tfrac{1}{2}a-d)\sqrt{k_1^2-\beta^2}\}=\frac{\sqrt{k_2^2-\beta^2}}{\mu_2}\cot\{d\sqrt{k_2^2-\beta^2}\}\quad\text{for}\quad\beta^2<k_1^2$$

and

$$-\frac{\sqrt{\beta^2-k_1^2}}{\mu_1}\tanh\{(\tfrac{1}{2}a-d)\sqrt{\beta^2-k_1^2}\}=\frac{\sqrt{k_2^2-\beta^2}}{\mu_2}\cot\{d\sqrt{k_2^2-\beta^2}\}\quad\text{for}\quad k_1^2<\beta^2<k_2^2 \qquad \ldots\ldots(142)$$

where

$$k_2^2=\omega^2\mu_2\varepsilon_2=\omega^2\mu_0\varepsilon_2$$
$$k_1^2=\omega^2\mu_1\varepsilon_1=\omega^2\mu_0\varepsilon_0 \qquad \ldots\ldots(143)$$

The first branches of the curve obtained by graphical solution of eqn. (142) give β for the H_{01} wave. Subsequent branches give higher-order waves.

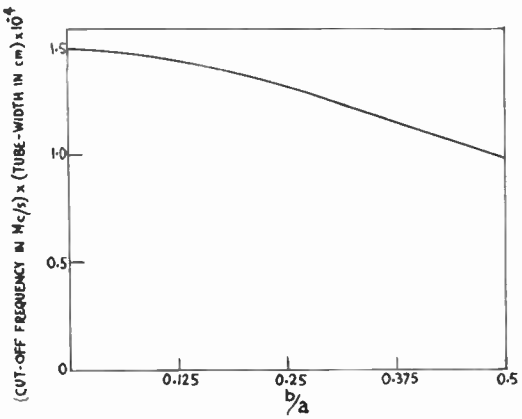

Fig. 19. Product of cut-off frequency and guide width as a function of b/a. (Ref. 15.)

The product of the cut-off frequency (f_c) and guide width a is obtained by putting $\beta = 0$ in eqn. (142). The variation of $f_c a$ vs. b/a is shown in Fig. 19. Figure 20 gives the variation of βa vs. $f_c a$ for $b/a = 0$, 1/8, 1/4, 3/8, 1/2; $\varepsilon_2 = 2{\cdot}3\times10^{-11}/36\pi$ F/cm $= 2{\cdot}3\varepsilon_1$; $\mu_0 = \mu_1 = \mu_2 = 4\pi\times10^{-9}$ H/cm for both Figs. 19 and 20. The curves in Fig. 20 tend to follow the curve

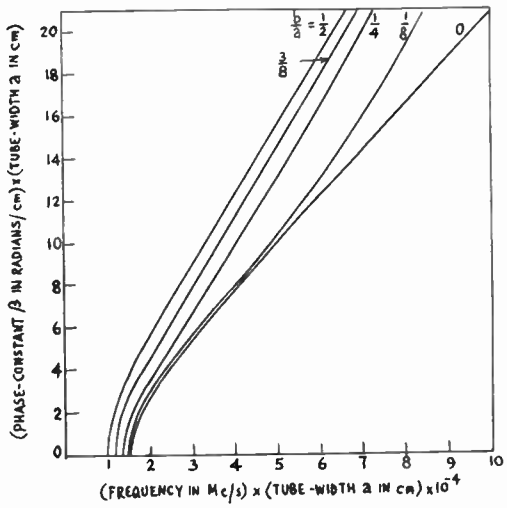

Fig. 20. Variation of the phase constant for H_{01} wave with respect to the product of the cut-off frequency and guide width. (Ref. 15.)

for an air-filled guide ($b/a = 0$) and then bend away from it. The bend occurs where

$$\beta_2^2=k_1^2=k_2^2-\left(\frac{\pi}{2d}\right)^2 \qquad \ldots\ldots(144)$$

which is the equation of a straight line through the origin.

(*Paper No. 1000/1.*)

[*To be continued*]

The remaining six sections of Part II of the paper will be published in the next issue of the *Journal*. Part III, which includes the References and Bibliography, will be published in December.

U.D.C.621.396.677

Limitations on Directional Patterns of Phase-compensated Circular Arrays

By

R. G. FENBY, B.Sc.†

Summary: This paper studies the principal design parameters of phase compensated circular arrays with a view to the synthesis of diametric-plane directional patterns having low side-lobes. After summarizing the general properties of such arrays it is shown that a maximum inter-element spacing exists, which if exceeded results in a rapid increase of side-lobe level. In most cases this spacing is 0·45λ. The effects of both amplitude tapers and directional elements are studied and it is shown that neither smooth amplitude tapers nor the use of directional elements can alone produce very low side-lobes. Several possible approaches to the design of low side-lobe aerials are discussed, involving tapers, directional elements, multiple rings, and semi-circular arrays. Experimental results are presented for the measured directional pattern of a 16-element circular array operating at 427 Mc/s under various conditions of excitation, and the results show sensible agreement with theoretical predictions. The studies are concerned with the possible application of these arrays to radar systems with 360 deg electronic scanning. Such systems place engineering constraints on the design of the arrays; consequently the effect of such constraints on pattern synthesis is also considered.

List of Symbols

C_n, S_n	function of number of elements (Appendix)
D	array diameter
$D(\theta)$	normalized horizontal directional pattern
$D_v(\alpha)$	normalized vertical directional pattern
$J_n(x)$	nth order Bessel function of argument x
$k=$	$2\pi/\lambda$
m, n, s	integers
N	number of elements (even) in complete array circle
R	array radius
$Z_{k'}$	k'th order directional pattern zero
α	elevation angle
β	azimuth bearing of main beam
γ_h	horizontal beamwidth
γ_v	vertical beamwidth
$\delta=$	$(\theta+\beta+\pi)/2$
θ	azimuth target bearing
λ	medium wavelength
$\sigma=$	$mn\delta$
ϕ	azimuth element position
ψ	radian-length phase difference in medium
ω	angular frequency in medium
ω_s	electronic-beam-rotation angular frequency

† Department of Electronic and Electrical Engineering, University of Birmingham.

1. Introduction

Although circular (or cylindrical) arrays have been the subject of spasmodic interest for many years,[1–4] their applications to low-inertia electronic beam-rotation radar systems have more recently received greater attention.[5–7] Such arrays are in many ways ideal for these systems because of their ability to produce a virtually distortionless beam in any azimuth direction, with 360 deg cover. Many primary and secondary radar requirements do not include beam-positioning in the elevation plane, and so several recent studies have investigated the problem of producing both transmission and reception systems capable of purely electronic beam position control[8–10] in the horizontal plane only. It has been found that the design of such systems is greatly dependent on the methods used to produce array directional patterns having low side-lobes. For this reason, a study of suitable procedures for realizing such patterns (consistent with relatively simple and economic system design) must be undertaken.

There are obviously many possible forms of aperture phase and amplitude distribution which could be used to produce a single-lobed horizontal-plane directional pattern. This paper considers a particular class of array operation characterized by having a cophasal main beam, along which direction all radiator outputs are made to add in phase. It can be shown (section 11.1) that a cosinusoidal aperture phase distribution is required to give this property. No similar prior restriction will be placed on the possible form of amplitude distribution, or 'taper', but

it will be noted that one unfortunate consequence of using circular arrays to cover 360 degrees of azimuth is that this taper must be rotated electronically around the aperture together with the cosine distribution of phase, in order to rotate the beam. It will be appreciated that this may be a great drawback on transmission, because the channel equipment feeding each element must contain an envelope modulator to effect this amplitude variation with time. Quite apart from the very considerable cost and increase in complexity which would result, it is evident that even if the amplitude taper were effected early in the transmitting system at low power levels, there would be an added necessity to provide phase-stable linear amplifiers throughout the remaining stages. This would be a very great disadvantage in a high-power radar. This problem may rule out the use of all but a coarse 'on/off' taper on transmission. It will be shown later that this restriction tends to limit the reduction in side-lobe level that could otherwise be obtained.

2. Directional Pattern Characteristics of a Continuous Aperture Array

A general analysis for a cophasal-beam (or 'phase-compensated') circular array is given in section 11.1; this develops an expression for the directional pattern from any phased arc in the plane containing the arc, for a constant element separation. The method used is an extension of that developed largely by Knudsen.[11] As is evident from eqn. (41), the generalized directional pattern is given by the normalized function:

$$D(\theta) = J_0\left(2kR\sin\frac{\theta-\beta}{2}\right(+ \\ + \frac{2}{s}\sum_{n=1}^{\infty} j^n J_n\left(2kR\sin\frac{\theta-\beta}{2}\right) . [C_n\cos n\delta + S_n\sin n\delta] \quad \ldots\ldots(1)$$

It is interesting to note that the basic J_0 term is always present, irrespective of the length of the phased arc or the number of elements. For the case of a complete circle of elements, eqn. (45) shows that

$$D(\theta) = J_0\left(2kR\sin\frac{\theta-\beta}{2}\right) + \\ + 2\sum_{m=1}^{\infty} j^{mN} J_{mN}\left(2kR\sin\frac{\theta-\beta}{2}\right) . \cos\frac{mN}{2}(\theta+\beta+\pi) \quad \ldots\ldots(2)$$

where N = number of elements (even).

If the number of elements is increased towards infinity, it is evident that (2) becomes simply

$$D(\theta) = J_0\left(2kR\sin\frac{\theta-\beta}{2}\right) \quad \ldots\ldots(3)$$

This idealized pattern is shown in Fig. 2. It is clear that the general side-lobe level is poorer than from an untapered linear array, the first side-lobe being about 8 dB below the main beam level.

2.1. *Horizontal Beamwidth from Continuous Aperture*

From eqn. (3), the horizontal beamwidth ($2\gamma_h$) from a continuous circular aperture is given by

$$J_0\left(2kR\sin\frac{\gamma_h}{2}\right) = 0{\cdot}707 \\ = J_0(1{\cdot}13) \quad \ldots\ldots(4)$$

For beamwidths of up to 40 deg, this may be written (with less than 2% error) as

$$\frac{\gamma_h}{2} \simeq \sin\frac{\gamma_h}{2} = \frac{1{\cdot}13}{2kR}$$

and so

$$2\gamma_h \simeq \frac{21}{R/\lambda}\text{degrees} \quad \ldots\ldots(5)$$

Thus, the beamwidth of a large continuous circular aperture is inversely proportional to the array diameter in wavelengths. This figure may be compared with the beamwidth from a continuous linear aperture of physical length $2R$:

$$\frac{\gamma_h(\text{linear})}{\gamma_h(\text{circular})} \simeq 1{\cdot}22 \quad \ldots\ldots(6)$$

It is not surprising to find that the narrower beam of the circular array is offset by the higher side-lobe levels compared with a linear array. Conversely, it might be expected that methods used to reduce the amplitudes of the side-lobes to acceptable limits would increase the beamwidth. There may therefore be little beamwidth improvement in practice over a linear array of the same length, when both are excited to give the same side-lobe level.

2.2. *Zero Spacings of the Horizontal Directional Pattern from a Continuous Aperture*

Equation (3) may be written as

$$D(\theta) = J_0(x)$$

A suitable expansion of $J_0(x)$ for large arguments (x) is given by Korn[12] as

$$J_m(x) \simeq \sqrt{\frac{2}{\pi x}} . \cos\left(x - \frac{m\pi}{2} - \frac{\pi}{4}\right) \quad \ldots\ldots(7)$$

where $|x| \gg |m|$

For $m = 0$, the directional pattern corresponding to large arguments therefore becomes

$$D(\theta) \simeq \sqrt{\frac{2}{\pi x}} . \cos\left(x - \frac{\pi}{4}\right) \quad \ldots\ldots(8)$$

It is clear that the zeros of $D(\theta)$ are zeros of $\cos(x - \pi/4)$, and so they occur at approximately equally spaced intervals, π apart, on the x scale—i.e. on a $\sin\theta/2$ scale. Naturally, the effect deviates from an even spacing as the argument drops in value,

but even for small arguments the maximum error is less than 1%. It is therefore concluded that the directional pattern of a continuous circular aperture has, for all practical purposes, uniformly spaced zeros on a sin $\theta/2$ scale.

This suggests that a suitable method of obtaining low side-lobes is to follow the analogous linear array synthesis procedure and construct the desired pattern by using angularly displaced beams in the sin θ domain. Unfortunately this technique is not directly applicable to circular arrays because the signal phasing needed to phase-compensate the array is carried out in the θ domain (unlike linear arrays, where the processing is done using sin θ as the variable). Thus displaced circular array patterns add on a θ scale, and low side-lobes can only be obtained over a small range of angles corresponding to $\theta \simeq \sin\theta$.

2.3. *Vertical Radiation Pattern from a Continuous Aperture*

It is interesting to note the form of the vertical radiation pattern, because this is a most important consideration from an operational point of view. If the beam is not being vertically positioned then a reasonably wide angle fan-beam is desirable in the

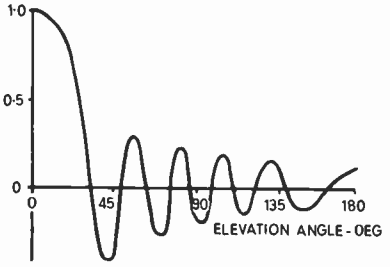

Fig. 1. Vertical response from 5λ diameter aperture, in main-beam plane.

vertical plane. This condition is (to some extent) fulfilled in practice, and section 11.2 derives the general form of the pattern:

$$D_v(\alpha) = J_0[kR(1-\cos\alpha)] \qquad \text{.....(9)}$$

where α = vertical elevation of target.

This has a half-beamwidth given by $\alpha = \gamma_v$:

$$J_0[kR(1-\cos\gamma_v)] = 0{\cdot}707 = J_0(1{\cdot}13)$$

and so

$$2\gamma_v \simeq 2\left[\frac{2{\cdot}26}{kR}\right]^{\frac{1}{2}} \qquad \text{.....(10)}$$

Equation (9) has been used to compute the vertical pattern of a 5λ diameter aperture array (Fig. 1); it is clear that a considerable vertical beamwidth exists. Furthermore, it is interesting to see from eqn. (10) that the vertical beamwidth decreases approximately as the square root of the array diameter in wavelengths. By manipulation of (5) and (10), it can be shown that

$$\frac{\gamma_v}{\gamma_h} \simeq [1{\cdot}8kR]^{\frac{1}{2}} \qquad \text{.....(11)}$$

This is an alternative way of demonstrating that, unlike planar arrays, circular arrays have horizontal and vertical patterns which are not independent.

Of course, these general remarks apply only to isotropic radiators; if elements are used which have marked vertical directivity but are horizontally omni-directional, then the overall directional pattern would be given by the product of the array and element vertical patterns. The use of either amplitude aperture tapers or horizontally directive elements will also cause the vertical beamwidth to alter.

2.4. *Summary of Section*

A continuous-aperture phase-compensated circular array has an array-plane directional pattern which has a narrower beamwidth than a linear aperture of the same width; such arrays have an inherently higher side-lobe level however. The zeros of a circular array pattern are nearly uniformly separated on a sin $\theta/2$ scale, but linear array sin x/x–type synthesis for low side-lobe patterns is not possible. The vertical radiation pattern has a considerably wider beamwidth than for the horizontal pattern; unlike linear arrays, the two patterns are not independent.

3. Circular Arrays with a Finite Number of Elements

It will be assumed throughout this work that the number of elements (N) will be even, to simplify analysis. As Knudsen has pointed out,[11] there may be some slight gain in using an odd number; however, for apertures of typical radar size this is probably an insignificant advantage. In this case, the directional pattern is given by eqn. (2). This is usefully separated into two terms: the continuous aperture term $J_0(2kR\sin\frac{1}{2}[\theta-\beta])$, and a distortion term made up of an infinite series of Bessel functions, each having the same argument as the continuous aperture factor:

$$D_d(\theta) = 2\sum_{m=1}^{\infty} j^{mN} J_{mN}\left(2kR\sin\frac{\theta-\beta}{2}\right).\cos\frac{mN}{2}(\theta+\beta+\pi) \qquad \text{.....(12)}$$

where $D_d(\theta)$ represents the distortion pattern. This expression is particularly convenient to apply in a number of circumstances.

3.1. *The Effect of the Number of Elements on the Horizontal Directional Pattern*

First, it is clear that $D_d(\theta)$ is zero as the number of elements (N) tends to infinity, because $J_{mN}(x)$ becomes zero for any finite value of argument. Conversely, as N falls from infinity there will come a point when $J_{mN}(x)$ becomes appreciable; by the nature of Bessel

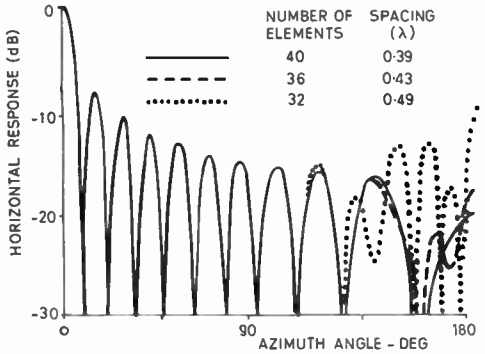

Fig. 2. Horizontal response from 5λ diameter array.

functions this will happen first (i) for large arguments and (ii) for small orders (mN). (The behaviour of (12) as far as numbers of elements are concerned lies mainly in the behaviour of the J_{mN} factors, for $\cos \frac{1}{2}mN(\theta+\beta+\pi)$ is merely a rapidly oscillating factor of peak value ± 1.)

Having first determined the array diameter by stipulating the desired beamwidth (Sect. 2.1), it is necessary to decide on the minimum possible number of elements that may be used without causing appreciable side-lobe increase due to the addition of the distortion pattern $D_d(\theta)$. Rewriting eqn. (12) gives

$$D_d(\theta) = 2j^N J_N(x) . \cos\sigma + 2j^{2N} J_{2N}(x) \cos 2\sigma + \quad \ldots\ldots(13)$$

where

$$\sigma = \frac{mN}{2}(\theta+\beta+\pi)$$

As N is reduced from infinity, there comes a point when the factors in (13) will become appreciable compared with the basic $J_0(x)$ pattern. However, $J_N(x) \gg J_{2N}(x) \gg J_{3N}(x)$ etc., for the case when $J_N(x)$ has not reached its first maximum, and so

$$D_d(\theta) \simeq 2j^N J_N\left(2kR \sin\frac{\theta-\beta}{2}\right) . \cos\frac{N}{2}(\theta+\beta+\pi) \quad \ldots(14)$$

As N is even, j^N is real, and so $D_d(\theta)$ is purely real. In the case of a non-zero-order Bessel function which has not reached its first maximum, the greatest value of $J_N(x)$ will occur at the maximum value of the argument x, that is, at $\theta = \pi$. Because of the very rapid rise from zero of high-order Bessel functions, it would be expected that the peak magnitude of $D_d(\theta)$ would rise quickly as θ approaches π. Thus the complete directional pattern is given by

$$D(\theta) \simeq J_0\left(2kR \sin\frac{\theta-\beta}{2}\right) + 2j^N J_N\left(2kR \sin\frac{\theta-\beta}{2}\right) . \cos\frac{N}{2}(\theta+\beta+\pi) \quad \ldots\ldots(15)$$

Figure 2 depicts the horizontal directional pattern resulting from 5λ diameter circular arrays having $N = 32$, 36, and 40, respectively. It can be seen that predictions made for (15) are in fact correct, and that the distortion is maximum at $\theta \simeq \pi$. The effect of the oscillating cosine term in (14) is also evident.

3.2. *Criterion for the Minimum Number of Elements*

Perhaps the most important practical point is the dramatic way in which the distortion term falls off, even at the back of the array, as N is slightly increased; this follows from eqn. (15) and is evident in Fig. 2. For any fixed argument x, the value $J_N(x)$ decreases rapidly as N increases slightly. This leads to a suitable criterion for determining the minimum number of elements (N_{min}) in any practical single-ring array (fed with a uniform aperture amplitude distribution). It is unfortunate that only this simple case appears to be analytically soluble. One criterion has been given by Horton,[13] but is applicable to small-diameter arrays only.

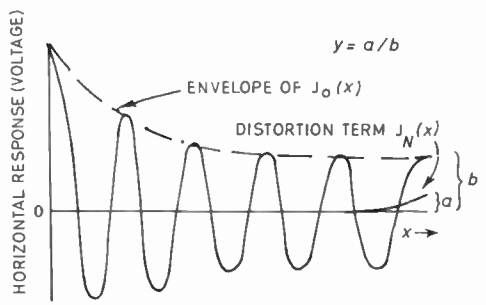

Fig. 3. Proposed criterion for minimum number of elements.

A more reasonable radar array criterion will now be given (Fig. 3). The value of N_{min} should be set by allowing the maximum value of the distortion term to be a certain fraction (say y) of the envelope of the continuous aperture $J_0(x)$ term, at $\theta = \pi$. Thus, N_{min} must be chosen so that

$$\pm 2J_{N_{min}}(2kR) = yJ_0(2kR) \quad \ldots\ldots(16)$$

The effect will then be that the side-lobes over the entire 360 deg cannot be more than $[20\log_{10}(y+1)]$ dB higher than for $N = \infty$.

First, however, it is necessary to find a suitable expression for the envelope of $J_0(x)$: such an expression is found in eqn. (7). For large arguments the envelope may be written

$$e = \sqrt{\frac{2}{\pi x}} \quad \ldots\ldots(17)$$

It can be shown that the error in using (17) is less than 0·5% for $x = 7$, and only 2·5% for $x = 2$. Maximum arguments below 2 would rarely be found in practice as they correspond to arrays of only $0{\cdot}7\lambda$ diameter.

A reasonable maximum side-lobe increase around the array due to using N_{min} elements instead of $N = \infty$

has been taken as 3 dB. As pointed out earlier, this value is only reached near $\theta = \pi$, and is likely to be much smaller than this even near $\theta = \pi$ due to the cosine multiplier term of eqn. (15). Using this criterion, a curve of N_{min} against array diameter in wavelengths has been computed (Fig. 4). As the distorting factor theory has assumed N to be even, the curve gives the nearest even number of elements equal to or greater than N_{min}. A further curve (Fig. 5) gives the resulting maximum element spacings as a function of array diameter. It will be noted that, even for large aperture arrays, a separation of $0{\cdot}45\lambda$ is the maximum permitted; for small arrays, elements may have to be spaced by as little as $0{\cdot}35\lambda - 0{\cdot}4\lambda$ to satisfy this criterion. It emphasized that small increases in separation over the figures given in Fig. 5 will tend to produce large back-lobes. For instance, $0{\cdot}5\lambda$ separation is too great (Fig. 2). In this respect circular arrays behave somewhat differently to their linear counterparts, and mutual coupling may therefore be a greater problem.

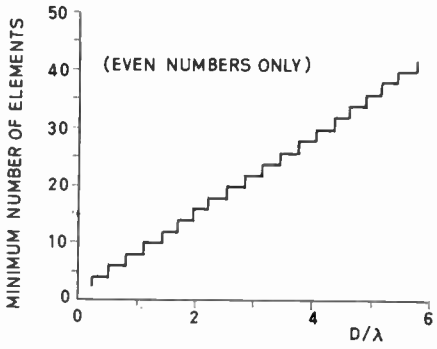

Fig. 4. Minimum number of elements for array of specified diameter.

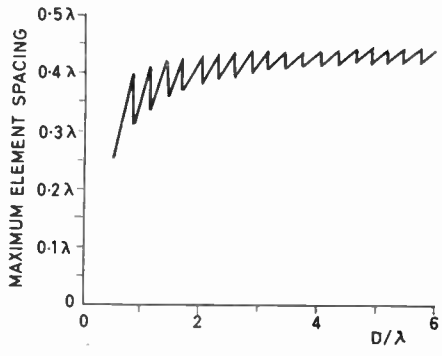

Fig. 5. Maximum element spacing.

3.3. *The Effect of Deflecting the Beam between Elements*

Clearly only partial rotational symmetry exists in a circular array using a finite number of elements, and

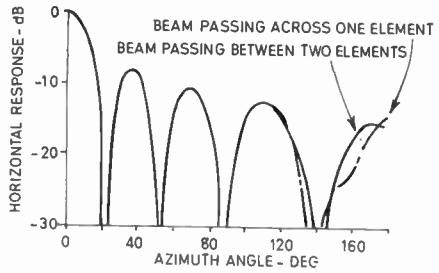

Fig. 6. Change in pattern shape due to variation of main beam deflection angle.

it would be expected that there would be a beam shape change when the beam was deflected to lie between the aperture sampling points. This is evident from eqn. (15). When the beam points across an element (say at $\beta = 0$) then

$$D(\theta) = J_0\left(2kR\sin\frac{\theta}{2}\right) + 2j^N J_N\left(2kR\sin\frac{\theta}{2}\right).\cos\frac{N}{2}(\theta+\pi) \quad \ldots(18)$$

and a comparison of eqns. (18) and (15) shows that the effect of deflecting the beam off normal by an angle β is

(i) to shift the basic $J_0(x)$ continuous aperture pattern along the θ axis by β, as expected,

(ii) to also shift the $J_N(x)$ distortion term along the θ axis by β, but to alter its magnitude by the ratio

$$\left[\frac{\cos\frac{N}{2}(\pi+\theta+\beta)}{\cos\frac{N}{2}(\pi+\theta)}\right]$$

It is the consequence of this amplitude change which causes pattern change; thus arrays with small distortion factors will have little overall pattern change with deflection angle. It will also be noted that the absolute maximum value of the distortion factor remains unchanged, and so if the criterion given in section 3.2 is used, the maximum value of the distortion due to the use of a finite number of elements is not affected by deflection angle. The array pattern for such a case has been computed and is shown in Fig. 6, where the beam from a 2λ-diameter array is shown deflected about half-way between elements. By comparison with the pattern for the case of the main beam lying across an element, it is evident that the change in shape is not deleterious.

3.4. *Summary of Section*

The effect of using a finite number of elements around the aperture is to add a distortion term to the $J_0(x)$ horizontal directional pattern of a continuous

ring. As the number of elements is reduced from infinity, severe lobes suddenly appear near 180 deg; $0{\cdot}45\lambda$ is the absolute maximum separation permitted if the side-lobes are not to rise more than 3 dB above the ideal $J_0(x)$ pattern. For small arrays, spacings of as little as $0{\cdot}35\lambda$–$0{\cdot}4\lambda$ may be sometimes needed; even small increases of separation above these figures will tend to produce large back-lobes. Although the pattern shape changes if the beam is deflected between elements, the peak amount of side-lobe deterioration does not increase above that due to the finite number of elements.

4. A Comparison Between the Effects of Amplitude Tapers on the Horizontal Directional Patterns of Linear and Circular Arrays

In linear array theory the performance of an array using directive elements may be predicted by the Product Rule, which states that the overall pattern is given by the product of the basic array and element patterns. There is no corresponding rule in circular array theory. Again, the use of smooth amplitude tapers is well understood for linear arrays, but it will be demonstrated that their effect on circular arrays is quite different. A mathematical approach to the combined use of certain tapers and directional elements has recently been made by James,[14] but this gives no idea of the reasons for the unusual pattern behaviour associated with cophasal-beam circular arrays.

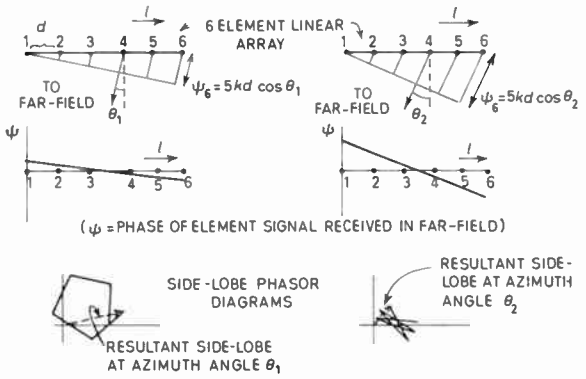

Fig. 7. Structure of linear array side-lobes.

This section puts forward a purely physical explanation of the differences in diametric-plane operation between linear and circular arrays. It shows, for instance, that amplitude tapering performs quite different operations in the two types of array. Basic differences such as these are due partly to the differing spatial element distributions, but equally to the phase compensations necessary to produce a cophasal beam from each type. To explain the real differences in operation, it is necessary to combine these two effects. This is accomplished by investigating the phases and amplitudes of the individual element contributions to the far-field radiation at any azimuth angle.

4.1. *Side-lobe Behaviour of Linear Arrays*

In this section, it will be assumed that the arrays are transmitting. Considering linear arrays first, the side-lobe phasor structure for two different azimuth angles is shown in Fig. 7; here the main beam is at $\theta = 0$. It is clear that the phase of the signals received from each element in the far-field is a linear function of the element position along the array, and that the slope of this line ($d\psi/dl$) increases with azimuth angle (up to $\theta = \pm 90°$). This will be referred to as the 'far-field element phase' curve. The phasor diagrams in Fig. 7 illustrate the reduction in peak side-lobe amplitude which occurs as the slope is increased. This is seen to be the reason why side-lobe levels from a linear array are reduced in strength as θ increases, because the far-field phase curve progressively tends to produce more tightly wound polygons.

4.2. *Side-lobe Behaviour of Circular Arrays*

It is now possible to consider the phasor diagram of circular array side-lobes. As is evident from section 11.1, the received far-field signal (at bearing θ) from an element located at ϕ_r on the array periphery is, for a main beam at $\beta = 0$:

$$\psi_F(\theta) = kR\,[\cos(\phi_r - \theta) - \cos\phi_r]$$
$$= 2kR \sin\frac{\theta}{2} \cdot \sin\left(\phi_r - \frac{\theta}{2}\right) \quad \text{.....(19}$$

Thus the received far-field phase distribution, for any θ, is sinusoidal if plotted as a function of element position around the array. This should be compared with the linear distribution which is obtained from a linear array. It is most important to note that, from (19), the sinusoidal phase variation from the circular array elements, as seen in the far-field, is a function of θ. This is shown graphically in Figs. 8 and 9, where the relative phases of the element contributions in the far-field from circular and linear arrays are shown as functions of azimuth angle.

It is clear that the circular array phase curve may be approximated to areas of low and high phase slope. It is the combinations of these different linear-array-like slopes, and the fact that the arcs responsible for each type are functions of far-field angle (θ), which characterize circular array patterns from those of linear arrays. Following the previous argument, it is evident that the areas of high phase slope must produce low side-lobes, while those of low phase slope are responsible for increased side-lobes (relative to linear arrays of the same width).

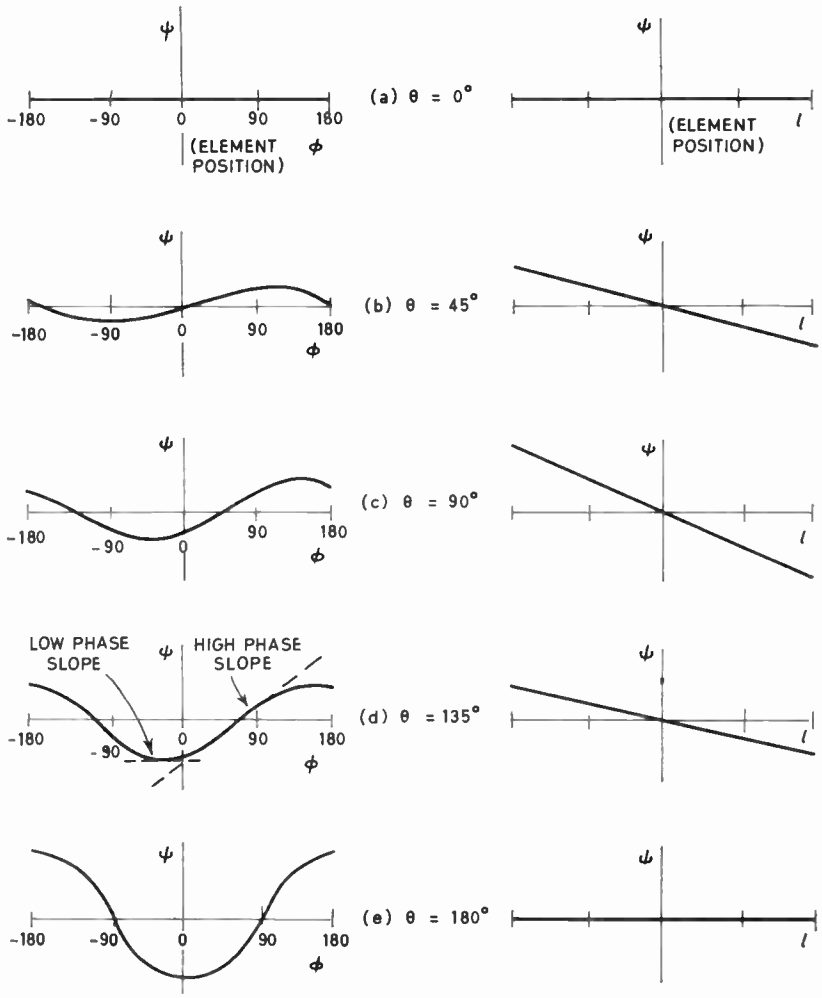

Fig. 8. Circular array.

Fig. 9. Linear array.

4.3. *The Effect of Amplitude Tapers on Circular Arrays*

It can now be appreciated that for any given far-field azimuth angle it is possible to apply an amplitude taper to a circular array to suppress contributions from those arcs which are responsible for low phase-slope far-field element contributions, and so reduce side-lobe levels. Unfortunately, this cannot be done for all azimuth angles because the low phase-slope contributions come from arcs whose position varies as θ varies (Fig. 8). It is therefore apparent that the use of a smooth amplitude taper alone cannot produce a circular array pattern having reduced side-lobes at all azimuth angles. For example, if elements near $\phi = \pm 90°$ are weighted down relative to those near 0 deg and 180 deg (e.g., by a $\cos^2 \phi$ taper) the side-lobes fall (Fig. 8(a), (b)) but the back-lobes rise (Fig. 8(d), (e)). This is evident in Fig. 10, which shows the computed directional pattern for a 5λ-diameter array with a $\cos^2 \phi$ taper, and a $\cos^{12} \phi$ taper Alternatively, if elements near $\phi = 0$ deg and 180 deg are weighted down (e.g., by a $\sin^2 \phi$ taper) the back-lobes are significantly reduced (Fig. 8(d), (e)) but the side-lobes rise (Fig. 8(a), (b)). Again, computed results agree with this general argument (Fig. 11).

It is now evident that this type of tapering performs quite different functions for circular and linear arrays. In the case of linear arrays, all side-lobe phasors are inclined at equal angles to their neighbours, and the tapering operation is merely one of symmetrically reducing the strength of side elements. The action is shown in Fig. 12 for the 45-deg side-lobe from a 5-element linear array of length 2λ. In the case of circular arrays, the process is more one of suppressing contributions from certain arcs, rather than applying symmetrical tapers over the entire circumference.

Since the form of the taper which is to be applied to a circular array to produce a low side-lobe level is itself a function of the side-lobe position, it is con-

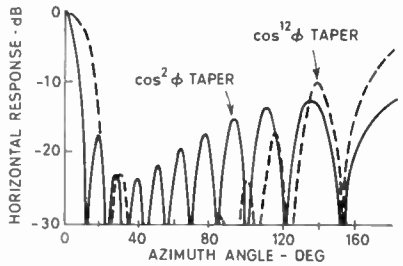

Fig. 10. Computed effect of amplitude tapers ($D = 5\lambda$).

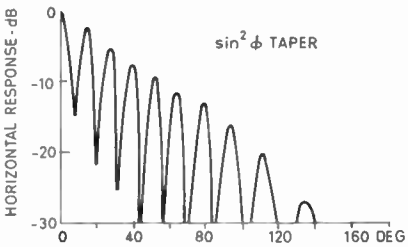

Fig. 11. Computed array pattern from tapered 5λ diameter ring.

cluded that smooth amplitude tapers are not capable of reducing the side-lobes at all angles. As is clear from Fig. 8 the same conclusions apply to smoothly-tapered semi-circular arrays, for the arcs producing high and low phase-slope side-lobe contributions are still functions of azimuth angle. It should be noted that the physical phase-slope arguments developed in this section are mainly useful for comparing tapered circular arrays with their linear counterparts. The theory does not yield useful results for tapered linear arrays.

4.4. *The Effect of Directional Elements on Circular Arrays*

James[14] has considered one particular case of the use of directional elements for circular arrays, and derives a purely mathematical treatment for the case of elements having a unidirectional, ideal-fan-shaped beam, showing that in large arrays their use always causes greatly reduced array side-lobes, but increased array back-lobes. However, this is only part of the picture. In an analogous way to that used in section 4.3, the phase-slope theory shows that element patterns may be selected to reduce near-in side-lobes at the expense of rising back-lobes (for example $\cos^2(\phi-\theta)$ directivity, Fig. 13). On the other hand, elements having zeros at $(\phi-\theta) = 0$ deg and 180 deg, and maxima at ± 90 deg (for example $\sin^2(\phi-\theta)$, give greatly reduced back-lobes but much increased side-lobes. Study of Fig. 8 shows that it is impossible to produce elements, having a relatively smooth response, which will reduce array side-lobes in all directions. This applies whether the elements are bi-directional or unidirectional.

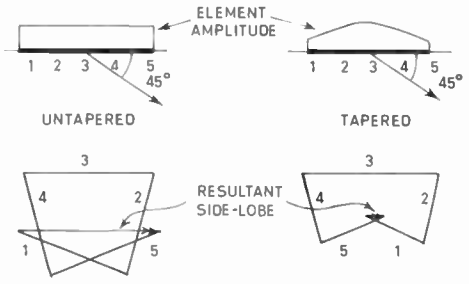

Fig. 12. Effect of tapering on linear arrays.

One intriguing result is that the directional pattern from an array having a $\cos^2\phi$ amplitude taper is exactly that from an array having $\cos^2(\phi-\theta)$ directional elements; this may be proved by showing that

$$\int_0^{2\pi} \cos^2\phi \,.\exp\left[-\mathrm{j}2kR\sin\left(\phi-\frac{\theta}{2}\right).\sin\frac{\theta}{2}\right]\mathrm{d}\phi$$

$$=\int_0^{2\pi} \cos^2(\phi-\theta).\exp\left[-\mathrm{j}2kR\sin\left(\phi-\frac{\theta}{2}\right).\sin\frac{\theta}{2}\right]\mathrm{d}\phi$$

Although this is a special case, it suggests that there exists some equivalence between symmetrical tapers (applied equally to the front and back of the array), and bidirectional elements.

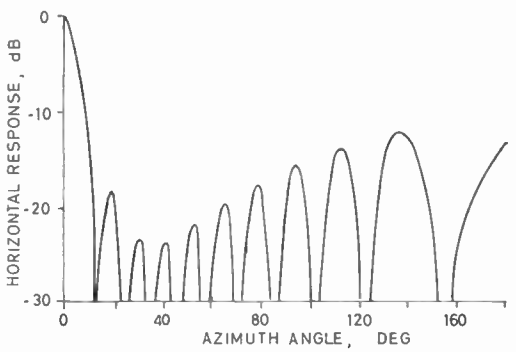

Fig. 13. Effect of using $\cos^2(\phi-\theta)$ directive elements.

One way of producing a bidirectional sub-array 'element' is to use two physically separated elements fed in phase; the phase centre of the sub-array then lies mid-way between them on a line joining their centres. However, as these sub-array 'elements' must lie about $0{\cdot}4\lambda$ apart to prevent pattern degradation, the separation of the adjacent physical elements will be very small indeed. To overcome the physical limitation, consider the proposal set out in Fig. 14. Here, N elements are split into N pairs; each pair is then fed in phase as a separate sub-array so that the N

required sub-arrays are obtained from only N elements. The output from each power adder is then the effective output from the appropriate sub-array, and is phase compensated in the normal way for a single-ring array. The method of operation has been described for a reception system for clarity; it is equally true for transmission, except that the roles of power adder and splitter are reversed.

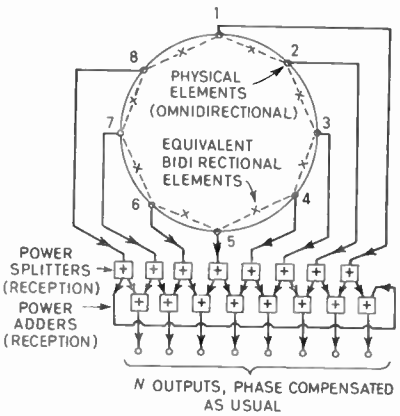

Fig. 14. Proposed system simulating a symmetrical amplitude taper, or bidirectional elements.

It will be noted from Fig. 14 that the phase centres of the equivalent sub-arrays lie on a circle of slightly smaller radius than the physical array. However, if the N output ports are compensated for the physical radius it can be shown that the sub-arrays are automatically correctly compensated. Consider the array transmitting, with compensation signals

$$A\cos(\omega t+\psi_r) \text{ and } A\cos(\omega t+\psi_{r+1})$$

being fed to the rth and $(r+1)$th input ports. The input signal to the rth element is clearly

$$v_r = \frac{A}{2}\cos(\omega t+\psi_r) + \frac{A}{2}\cos(\omega t+\psi_{r+1}) \quad ...(20)$$

Thus, since $\psi_r = -kR\cos(2\pi r/N-\omega_s t)$, eqn. (20) may be expanded to give:

$$v_r = A\cos\left[kR\sin\frac{\pi}{N}\,.\,\sin\left(\frac{2\pi}{N}(r+\tfrac{1}{2})-\omega_s t\right)\right]\times$$
$$\times\cos\left[\omega t-kR\cos\frac{\pi}{N}\,.\,\cos\left(\frac{2\pi}{N}(r+\tfrac{1}{2})-\omega_s t\right)\right] \quad .....(21)$$

This may be recognized as an amplitude-tapered cophasal distribution; the amplitude taper function is:

$$A(r) = A\cos\left[kR\sin\frac{\pi}{N}\,.\,\sin\left(\frac{2\pi}{N}(r+\tfrac{1}{2})-\omega_s t\right)\right] \quad ...(22)$$

which is symmetrical about $\phi = -\pi/N$ and π/N (as expected) and has a maximum value of A at these angles. The minimum value is a function of $kR\sin\pi/N$. This amplitude taper automatically rotates around the aperture at the phase distribution rotation frequency.

Thus an equivalence has been obtained between the effects of certain bidirectional elements and symmetrical amplitude tapers on the directional pattern from a single ring array. This principle can be extended however: a sub-array pattern different from that of a 2-element broadside array may be obtained by forming a sub-array of M elements (located on the arc of the physical circle of N elements), and then cophasally exciting the resulting phase centres of each of the sub-arrays. Although this process essentially forms 'curved' linear sub-arrays, its electronic nature provides a convenient method of simulating independent directive elements spaced equally around the circumference. Array patterns similar to the types shown in Figs. 10 and 13 could therefore be produced without having to make directive elements or rotate amplitude tapers. Although it has been shown that such methods are alone incapable of producing low side-lobes from a single-ring array, a dual-ring technique giving low side-lobes and high gain will be described, for which these processes are useful.

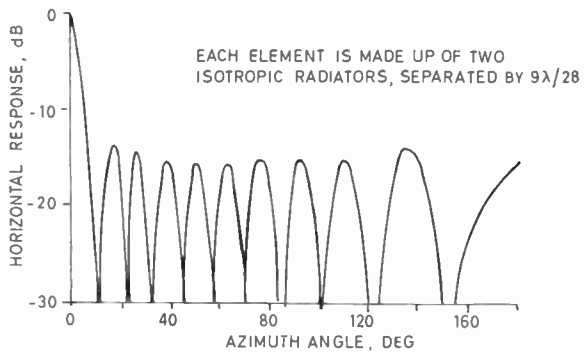

Fig. 15. Computed array pattern from 5λ diameter ring.

Another interesting point about single-ring arrays using directional elements is that a compromise is possible between the reduction of side-lobes and increase of back-lobes: it is theoretically possible to obtain an array pattern which has approximately equal-strength side-lobes. A suitable element pattern may be obtained most conveniently by feeding adjacent elements in phase to produce a broadside sub-array. By iterative digital computing methods, the separation of the elements may be adjusted to give a near-equal-strength side-lobe level. It has been found that an element separation of $0{\cdot}32\lambda$ is optimum in this respect for an array of diameter approximately 5λ: the resulting pattern is shown in Fig. 15. A suitable method of exciting the N elements to produce N equivalent sub-arrays has been described above.

4.5. *Summary of Section*

No smooth amplitude taper is alone capable of reducing side-lobes at all azimuth angles from a circular or a semicircular array. If applied, amplitude tapers on a circular array perform a quite different operation from similar linear array tapers. Similarly, directional elements are alone incapable of producing a very low side-lobe array pattern, and their effect is in many ways similar to that of amplitude tapers. A simple electronic system can simulate the effect of certain bidirectional elements or symmetrical tapers. Uniform side-lobe patterns can thereby be produced from a single ring of elements, but the resulting side-lobe level is not particularly low.

5. Semi-Circular Arrays

It has been shown above that neither smooth amplitude tapers nor the use of directional elements can alone produce a horizontal directional pattern having very low side-lobes. James[14] has suggested that a semi-circular array with unidirectional elements should be capable of producing low side-lobes at all angles. Such an array would be attractive for an electronic beam-positioning or continuous-scanning radar, because the only realistic taper for high-power phased-radar transmission is in the form of electronically-switched elements which are either on or off. By the use of techniques described elsewhere,[8] such a rotating 'square-wave' amplitude taper may be generated fairly easily for continuous-scanning or beam-positioned radar.

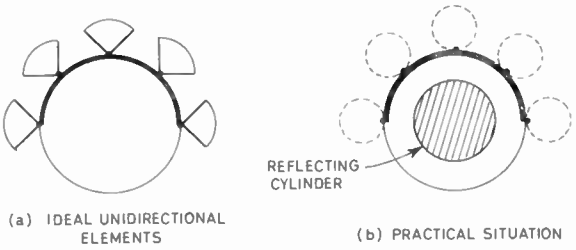

Fig. 16. (a) Ideal unidirectional elements.
(b) Practical situation.

Again we can make use of the 'far-field element phase' curve, for this array was conceived when it was realized that a semi-circular group of elements, backed with a reflecting semi-circular sheet, could provide a method of automatically suppressing the outputs of those elements producing a low phase slope ($d\psi/d\phi$) at all far-field azimuth angles, and so give a low side-lobe pattern. For example, referring to Fig. 8 (and remembering that elements between 90 to 180 deg, and -90 to -180 deg are switched off), elements near $\phi = 0$ deg should be removed to reduce the back-lobe level ($\theta \simeq 180$ deg); at $\theta \simeq 135$ deg elements near $\phi \simeq -23$ deg should be removed; at $\theta = 90$ deg, the output from the arc near $\phi = -45$ deg should be suppressed: and so on. It will be appreciated that these conditions can in fact be met using unidirectional elements, which provide a method of varying the side-lobe contributions from each portion of the circumference at different azimuth angles. A convenient experimental way of simulating such elements appears to be the use of a central reflecting cylinder in conjunction with a circle of dipoles or monopoles; the main beam direction is then selected by exciting and phase-compensating the appropriate semi-circular arc (Fig. 16). The computed array pattern for a typical case is shown in Fig. 17 for a 5λ-diameter array.

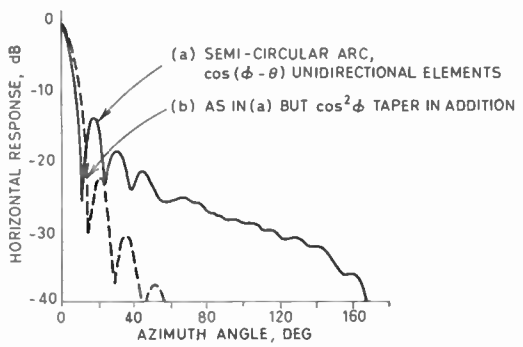

Fig. 17. Computed semi-circular array patterns ($D = 5\lambda$).

5.1. *The Effect of Non-ideal Element Patterns*

James[14] has considered the ideal case of directional elements which have a perfect fan-beam shape (Fig. 16(a)). Clearly, such elements cannot be exactly realized. It can be appreciated that practical elements, having a more gradual gain/angle fall-off, will tend to introduce an amplitude tapering effect at any given far-field angle (Fig. 16(b)). This would tend to give an asymmetrically-tapered linear array effect (Fig. 8), if it were not offset by the varying element density across the aperture. Thus the side-lobes are lower if practical (rather than ideal) elements are used. Moreover, this tendency may be optimized by applying an additional amplitude taper which reduces the effect of the side elements, and an immediate improvement is evident (Fig. 17(b)). From the viewpoint of phased-array system design, it is unfortunate that the relatively simple requirements of providing an on/off 'square-wave' taper seems to be complicated by a requirement for an additional 'fine-detail' taper to give low-side-lobe patterns. A simpler 'coarse' taper (using perhaps three levels: off, half-on, full-on) might be a better solution.

6. Dual-Ring Arrays

It has been shown in section 2.2 that the zeros from a continuous single ring aperture are very nearly equally spaced on a sin $\theta/2$ scale. On a $\theta/2$ scale the zero spacing tends to increase with θ up to 180 deg; use can be made of this principle to produce very low back-lobe radiation by using two concentric phased rings. The principle is shown in Fig. 18. The diameters are chosen so that, if k' represents the number of the zero (from the origin), the outer ring zero nearest $\theta = 180$ deg (say $Z_{k'}$) coincides with zero $Z_{k'-1}$ of the inner ring. In some cases it may be found advantageous to arrange that $(Z_{k'-1})_{\text{outer}}$ coincides with $(Z_{k'-2})_{\text{inner}}$; however, the general idea is the same: the side-lobes on either side of the coinciding zeros tend to cancel out, while the main beam and near-in side-lobes tend to add.

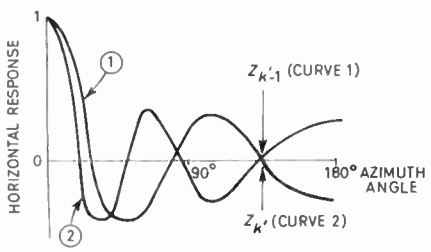

Fig. 18. Principle of dual-ring array.

From section 2.2, it follows that, for large arguments (such as are found for $\theta \simeq \pi$), $J_0(2kR \sin \theta/2)$ is zero when

$$2kR \sin \frac{\theta}{2} = \left((2m+1)\frac{\pi}{2} + \frac{\pi}{4}\right) \qquad \text{.....(23)}$$

(where m is any integer)

If R_1 and R_2 are the radii of the two rings, and it is desired that corresponding zeros $z_{k'}$ and $z_{k'-1}$ should coincide at the same azimuth angle (say θ_p), then

$$2k(R_1 - R_2) \sin \frac{\theta_p}{2} = \left[\{2(k'-1)+1\}\frac{\pi}{2} + \frac{\pi}{4}\right] - \left[\{2(k'-2)+1\}\frac{\pi}{2} + \frac{\pi}{4}\right]$$

$$= \pi$$

and so the difference in radii if θ_p is close to 180 deg is

$$R_1 - R_2 \simeq \frac{\lambda}{4} \qquad \text{.....(24)}$$

It will be noticed that there is no constraint on the absolute values of R_1 and R_2, other than this connection. The technique is illustrated in Fig. 19(a) for diameters of 5 and 4·5λ.

A separation of 0·25λ between the two rings is not encouraging as far as mutual coupling is concerned. However, by allowing the coincident zeros to lie some way from the 180 deg point (and preventing significant 180 deg radiation by arranging the absolute diameters so that zeros lie in the region just beyond sin $\theta/2 = 1$), the difference between R_1 and R_2 may be increased, perhaps to as much as 0·35λ.

It will be recognized that this whole procedure relies on equal-strength contributions from the two rings; if the numbers of elements differ in each ring then the amplitudes of the currents fed to each element must be adjusted accordingly.

6.1. *A Method of Reducing the Number of Elements in a Dual-ring Array to the Minimum Possible*

So far, no restriction has been placed on the number of elements in each ring, other than that implied in Section 3. It will now be shown that the use of dual rings permits a slightly greater element spacing to be used in each ring than is indicated in section 3.2.

It will be noted from eqn. (15) that, for N even, the distorting term in each ring is always real. However, for $N/2$ even, the factor j^N is $+1$; for $N/2$ odd it is -1; thus the sign of this distorting term for a given azimuth angle range depends on the value of N. By choosing the number of elements in the outer ring and inner ring so that they differ by 2, it therefore becomes

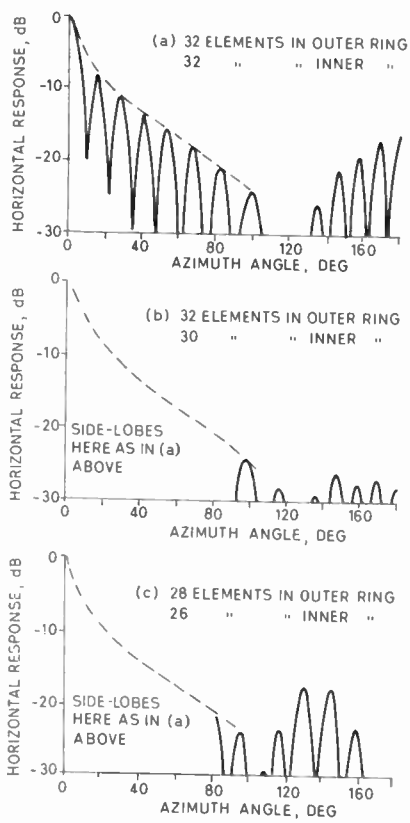

Fig. 19. Response from dual-ring array (5λ, 4·5λ diameters).

possible partly to cancel the distorting terms as well as the continuous aperture back-lobes. Examples of this are shown in Fig. 19. Curve (a) shows the pattern from dual rings (diameters 5 and 4·5λ) with 32 elements in each ring, while (b) shows the improvement obtained by *reducing* the number of elements in the inner ring to 30. Curve (c) shows the effect of reducing both outer and inner ring element numbers to 28 and 26 respectively, and it is evident that an improvement over 32 elements per ring is still present. In all cases the patterns were computed using equalized main beam amplitudes from each ring. This may be a useful method of reducing the mutual coupling between elements and of keeping the cost to a minimum.

6.2. *A Dual Ring Array using Directional Elements to give a Low Side-lobe Pattern*

Following the discovery that certain directional elements can produce a single-ring array pattern having low side-lobes but increased back-lobes, it seems reasonable to suppose that the use of dual concentric rings of directional elements will give an improved overall pattern. Such an array pattern is shown in Fig. 20 for rings of diameter 5λ and 4·5λ; each element has a $\cos^2(\phi-\theta)$ individual pattern. There may be no need to use physical directive elements; the purely electronic system described in section 4.4 could produce a similar effect.

The requirement that the two rings must be independently phase-compensated is a disadvantage, but a recent proposal by Chow[9] outlines a digital continuous beam-rotation system which is easily adapted to exciting double ring arrays with a relatively small increase in complexity.

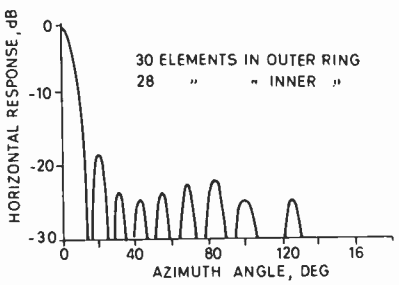

Fig. 20. Response from dual-ring array (5λ, 4·5λ diameters) having $\cos^2\phi$ amplitude taper or $\cos^2(\phi-\theta)$ bidirectional elements.

7. Experimental Circular Array Test Facilities

A small experimental test facility has been constructed in the Department of Electronic and Electrical Engineering at the University of Birmingham, and is designed for pattern measurements from a 2λ-diameter single-ring phase-compensated array operating at 427 Mc/s (70 cm). Facilities will ultimately be provided for individual phase and amplitude control of the signals fed to each of the 16 elements, but at present phase compensation is accomplished by using fixed lengths of coaxial cable: the residual phase and amplitude errors inherent in each channel are estimated to be less than ± 15 deg and $\pm 1{\cdot}5$ dB respectively. The elements are $\lambda/4$ monopoles mounted above an octagonal groundplane of about 6·4λ in extent. The outer part of the groundplane is made of mesh (weave $\simeq 0{\cdot}02\lambda$) to reduce weight and wind resistance. Such a fine weave effectively simulates a solid groundplane.

7.1. *The Measurement of Horizontal Plane Directional Patterns*

A number of pattern measurements have been taken using the array described above, with particular reference to the action of certain factors ignored in the preceding sections, such as mutual coupling, element shadowing, and groundplane effects. The array directional pattern for a complete circle of elements is shown in Fig. 21, together with the theoretical pattern computed from section 3. It will be noted that the two are in fairly good agreement, the first few side-lobes being of the appropriate magnitude and correctly positioned. The back radiation is slightly greater. Although the side-lobe level is not particularly low, the agreement is perhaps surprising in view of the phase and amplitude errors in the array excitation system, and the relatively close element spacing (0·39λ). By the use of Monte-Carlo techniques, curves have been computed for the patterns from a 2λ-diameter array in which the sixteen elements have independent Gaussian phase errors in their feeding systems (Fig. 22). These curves show the expected levels which will be bettered by 99%, and 90%, of all possible side-lobes. It is interesting to note that, for a 2λ-diameter array, the 99 percentile first side-lobe is only $-6{\cdot}4$ dB for 10 deg standard deviation phase errors, compared with about $-8{\cdot}0$ dB for no phase errors.

7.2. *Factors Affecting the Theoretical Pattern*

It is difficult to envisage the effect of mutual coupling on the shape of the computed pattern, except to point out that it produces phase and amplitude errors in the far-field contributions from each element. In order to assess the degree of coupling, measurements were taken of the induced voltage in elements close to a reference element; the latter was excited at frequencies above and below 427 Mc/s to obtain some idea of the variation with frequency. All other elements were terminated in their characteristic impedance.

The degree of coupling is shown in Table 1.

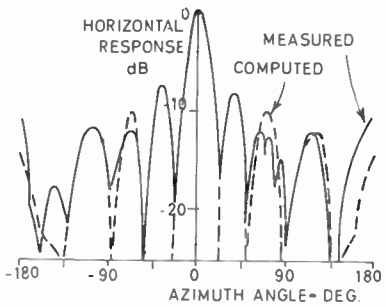

Fig. 21. Measured circular array response ($f = 427$ Mc/s) 2λ diameter.

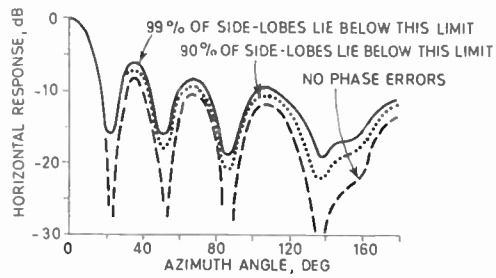

Fig. 22. Percentile pattern limits for 2λ diameter array ($N = 16$); Gaussian phase errors of standard deviation = 10 deg.

Table 1

Frequency (Mc/s)		363	384	427	470
Input to channel	1 (dB)	0·0	0·0	0·0	0·0
Output from channel	2 (dB)	− 12·7	− 11·4	− 13·3	− 16·0
	16 (dB)	− 13·1	− 11·4	− 14·1	− 15·8
	3 (dB)	− 18·0	− 18·0	− 19·7	− 23·3
	15 (dB)	− 17·6	− 19·4	− 19·3	− 23·9
Adjacent element separation (wavelengths)		0·33	0·35	0·39	0·43
Element length (wavelengths)		0·21	0·22	0·25	0·27

The coupling between adjacent elements is about 13 dB at 427 Mc/s, a figure which improves to 15 dB at 10% above this frequency. Conversely, the figure tends to be lower at lower frequencies. The exact figures at frequencies other than 427 Mc/s are not particularly significant except that they demonstrate the reduced coupling which occurs as the element separation (in wavelengths) increases. There is evidence that coupling tends to increase as the monopoles become resonant (defined as the frequency at which the reactive component of input impedance becomes zero—about 390 Mc/s in this case). The measured value of 13 dB coupling between adjacent elements does not seem unduly high considering that the separation is only $0{\cdot}39\lambda$. It is an unfortunate consequence of the 360 deg rotation capability of circular arrays that elements must be spaced as closely as $0{\cdot}4\lambda$, whereas in limited-deflection linear arrays separations of $0{\cdot}57\lambda$ are common with consequent reduction in coupling to nearer 20 dB.

The effect of the associated problem of element shadowing is also difficult to predict. Measurements have been taken to discover the extent of shadowing. A single element was excited by a 427-Mc/s source, and all other elements were terminated in their characteristic impedance. The horizontal far-field pattern from the single element was measured and the experiment was also repeated at 406 Mc/s, to see if the shadowing became more serious as the element neared resonance.

The results are shown in Fig. 23. It is immediately evident that considerable shadowing is present, the output from one element varying by as much as 9 dB with change in azimuth angle. Considering the 427 Mc/s pattern first, it is clear that there are really two types of variation occurring: a rapid, fairly shallow variation (between 0 to 90 deg, and 270 to 360 deg), and two deeper nulls located near 130 and 230 deg. These observations seem to have good physical backing, because it is these two latter positions which coincide with the maximum obstructing density of elements (Fig. 23). It therefore appears that the two nulls represent the main physical effect of shadowing, while the smaller variations at other angles are manifestations of mutual coupling in general. As expected, the effect becomes worse at 406 Mc/s; this seems to be partly because the elements are closer to electrical resonance at this frequency, and partly because they are spaced closer electrically.

One way of reducing shadowing is to make the monopoles non-resonant, that is, by cutting their physical length to less than $0{\cdot}25\lambda$ at the operating frequency. Stewart[15] reports considerably reduced deep-null shadowing by using monopoles of $0{\cdot}21\lambda$ physical length. However, the smaller variations of

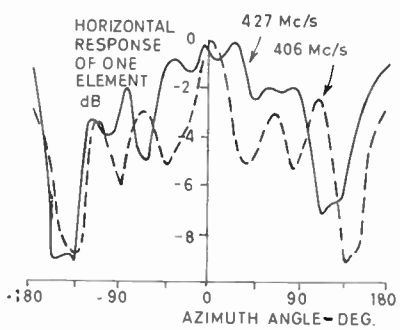

Fig. 23. Effect of shadowing on the polar response of one element.

the order of 4 dB at other angles are barely improved by this process, as they are an inevitable result of mutual coupling (as opposed to resonant element absorption). An additional disadvantage is the lowered element input impedance which results.

Since the elements are identical, it would be expected that they would all behave in this way; thus the effect of shadowing may perhaps be treated as a special case of element directivity, in which the elements radiate most effectively in the outward direction. It has been shown above that this results in increased array back-lobes, with reduced near-in side-lobes. Reference to Fig. 21 shows that there is a slight tendency to this behaviour.

An additional source of pattern error may be due to ground-plane effects. A disadvantage which follows from the use of a non-infinite groundplane is that its edges, being discontinuities in the surface current distribution, act as additional line sources. These tend to produce destructive far-field interference, the nature of which depends on the form of ground-plane boundary. For example, a ground-plane with a randomly-varying edge will tend to produce small random far-field perturbations in the pattern. On the other hand, any regular-shaped ground-plane may introduce periodic, more intense variations. It is thought that such variations may in fact be in evidence on several patterns; in particular, a typical example may be the 70 deg side-lobe of Fig. 21. Unfortunately the periodicity of these variations is about the same as that of the measuring positions in the far-field, and so the effect tends to be hidden.

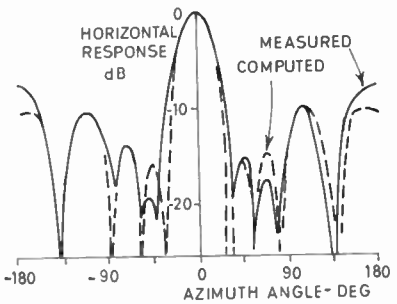

Fig. 24. Experimental amplitude-tapered array response, $D = 2\lambda$.

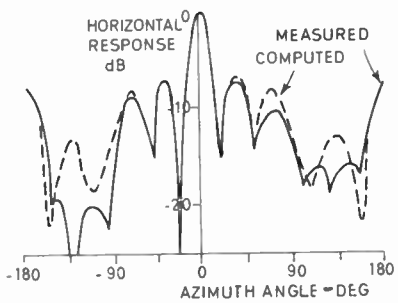

Fig. 25. Experimental semi-circular array response, $D = 2\lambda$.

7.3. *Further Pattern Measurements*

Following the basic array pattern measurement described above, several other configurations have been investigated. First, the effect of a $\cos^2 \phi$ amplitude taper was measured (Fig. 24). Although it was not possible to apply an exact $\cos^2 \phi$ taper, the measured pattern shows the predicted near-in side-lobe reduction and accompanying back-lobe rise which is typical of such tapers.

A number of semi-circular array patterns have also been measured. The first (Fig. 25) shows the complete response of an untapered semi-circular array with omni-directional elements. It has often been supposed that the back half of a circular array is redundant. Although this appears to be true for tapered arrays using particular directional elements,[14] it certainly does not apply to untapered arrays; both theoretical and measured patterns show a rise in side-lobe level compared with a complete circle of elements.

Following the ideas put forward in section 5, the elements in the semi-circle were made unidirectional by the introduction of a central reflecting cylinder of diameter $1{\cdot}5\lambda$. The exact theoretical pattern could not be evaluated due to difficulties arising from the use of a curved reflector, but if a 3-dB element beamwidth of about 70 deg is assumed, the resultant theoretical array pattern predicts reasonably accurately the measured beamwidth and side-lobe level (Fig. 26). As explained in section 5 the characteristics of practical directional elements limit the reduction in side-lobe level which is otherwise attainable with semi-circular arrays. However, the physical argument put forward in section 5 suggests that at least some improved side-lobe performance may be achieved by applying an additional amplitude taper (for example, $\cos^2 \phi$) to the array. The resultant measured pattern is shown in Fig. 26(b). The maximum side-lobe level of -20 dB compares very favourably with that of -8 dB from an untapered circle of isotropic elements, but the horizontal beamwidth has increased by about 60%. Mutual coupling undoubtedly accounts for some of the discrepancies between the theoretical and measured array patterns when such low side-lobes are present. In particular, the presence of the reflecting screen aggravates this problem because of increased near-field interaction.

8. Conclusions

This paper has considered the performance of cophasal-beam circular aerial arrays, with particular reference to their use for radars having electronically controlled beam-positioning capabilities. For such proposed radar systems[8] it is most inconvenient,

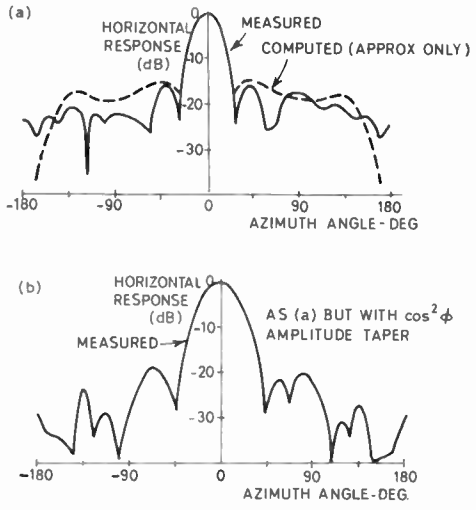

Fig. 26. Experimental semi-circular array, with directional elements.

particularly on transmission, to rotate an amplitude taper (in synchronism with the phase distribution) as the beam is electronically moved in azimuth. A conflicting requirement is that low two-way side-lobe levels are required. The only type of taper which would be permissible in the transmission system is an 'on/off' type which could be used to cut off elements at the back of the array, leaving the front semi-circle active.

The greatest virtue of the circular array—its symmetry, and ability to position a beam without appreciable distortion anywhere within 360 deg—is therefore one of its major drawbacks, in that fixed amplitude tapers cannot be used if the beam is to be moved. Another disadvantage is the fact that neither smooth amplitude tapers nor the use of directional elements can alone produce improved side-lobe reduction at all angles from a single ring. The only suitable combination for electronically-scanned radar systems appears to be a 'square-wave' on/off amplitude distribution which cuts off the back of the array, together with the use of unidirectional fan-beam elements.

It is interesting to note that this represents a tendency to revert back to the inefficient Wullenweber philosphy. It seems to be an unfortunate property of compensated circular arrays that low overall side-lobe levels cannot be realized if attempts are made to use more than half of the aperture. This appears to argue against the use of cosine phase-compensation. On the other hand, although low side-lobe levels can theoretically be produced if complex phase and amplitude distributions are permitted,[16] there is no evidence that such arrays necessarily have a higher aperture efficiency than do semi-circular cosine phase-compensated arrays. In addition, complex phase and amplitude tapers are difficult to rotate around the aperture of electronically-scanning arrays.

A more efficient array is obtained by using two concentric rings of specified diameters. In this case, relatively low-side-lobe patterns may be obtained by the use of an amplitude taper or directional elements alone. Although relatively large numbers of elements are required, the array might be useful for transmission in cases where it is more convenient to add large amounts of power in space rather than in hybrid junctions.

Practically, phase-compensated circular arrays exhibit a greater tendency to suffer from element shadowing and mutual coupling than do linear arrays. The worst aspect of shadowing can be overcome by using less efficient radiating elements. The mutual coupling problem primarily arises from the necessity to space elements by less than $0{\cdot}35\lambda$–$0{\cdot}45\lambda$, according to array diameter, and may be a considerable obstruction to the attainment of very low side-lobe patterns.

9. Acknowledgments

The author wishes to thank the staff of the Radio Group of the Department of Electronic and Electrical Engineering, University of Birmingham, for their valued assistance and discussions, Professor D. G. Tucker for his criticism of the manuscript, and particularly Dr. D. E. N. Davies for his guidance and encouragement throughout the course of this work. Special thanks are due also to the entire technical staff of the Department, and to Mr. E. McCabe and Mr. B. Fantini for making the pattern measurements. The author is also grateful for the provision of a Scholarship from Guest, Keen and Nettlefolds Limited.

10. References

1. W. R. LePage, C. S. Roys and S. Seely, "Radiation from circular current sheets", *Proc. Inst. Radio Engrs*, **38**, p. 1069, 1950.
2. U.S. Department of Commerce, "Compensated Circular Antenna Arrays". P.B. 8922, 1946. (D.S.I.R. Library No. 6413. 35B).
3. T. A. Mitchell, "The Design of Cylindrical Aerials by means of Equivalent Linear Arrays". Admiralty Surface Weapons Establishment, Portsmouth, Technical Note RX2–59–16, 1959 (unclassified).
4. C. E. Hickman, H. P. Neff and J. D. Tillman, "The theory of a single-ring circular array", *Trans. Amer. Inst. Elect. Engrs*, **80**, part 1, p. 110, 1961.
5. B. S. McCartney, "Proposals for an electronically scanned circular array", *Proc. Instn Elect. Engrs*, **110**, p. 120, 1963.
6. G. Chadwick and J. Glass, "Investigation of a Multiple Beam Scanning Circular Array". Radiation Systems Inc., Alexandria, Va., U.S.A. (Air Force Cambridge Research Labs. report).
7. H. P. Neff and J. D. Tillman, "An electronically scanned circular antenna array", *I.R.E. Nat. Conv. Rec.*, **8**, part 1, 1960.

8. D. E. N. Davies and B. S. McCartney, "Cylindrical arrays with electronic beam scanning", *Proc. Instn Elect. Engrs*, **112**, p. 497, March 1965.
9. P. Chow, Internal Interim Project Report, Department of Electronic and Electrical Engineering, University of Birmingham, 1964.
10. R. G. Fenby, "A Study of Phase-Compensated Circular Aerial Arrays for Electronic Beam-Scanning Radar Systems". M.Sc. Thesis, Department of Electronic and Electrical Engineering, University of Birmingham, 1965.
11. H. L. Knudsen, "Radiation from ring quasi-arrays", *Trans. Inst. Radio Engrs on Antennas and Propagation*, **AP-4**, p. 452, 1956.
12. G. A. Korn and T. M. Korn, "Mathematical Handbook for Scientists and Engineers", p. 734. (McGraw-Hill, New York,, 1961.)
13. J. W. Horton, "Fundamentals of Sonar", p. 257, U.S. Naval Institute, Md., U.S.A., 1957.
14. P. W. James, "Polar Patterns of Phase Corrected Circular Arrays". Royal Aircraft Establishment, Technical Note RAD 872, June 1964, (unclassified).
15. A. C. Stewart, "Experimental Performance of a Circularly Symmetrical Antenna Array". National Bureau of Standards unpublished report, 1962.
16. G. Ziehm, "Optimum directional pattern synthesis of circular arrays," *The Radio and Electronic Engineer*, **28**, p. 341, November 1964.

11. Appendix

11.1. *The Horizontal (diametric-plane) Directional Pattern from a Circular-arc Cophasal-beam Array*

It is assumed for convenience that the array is mounted with its diametric plane horizontal. The main beam lies at an angle β to the reference axis, and so the electrical phase compensation for an element at ϕ_r is $kR\cos(\phi_r-\beta)$. For a far-field azimuth angle of θ, the spatial relative delay for that element is clearly $d = R\cos(\phi_r-\theta)$—see Fig. 27. Thus the far-field output from the element is of the form

$$V_r(\theta, t) = \cos\left[\omega t + kR\left\{\cos(\phi_r-\theta)-\cos(\phi_r-\beta)\right\}\right] \quad \ldots\ldots(25)$$

When the element outputs are added, the array pattern becomes

$$V(\theta, t) = \sum_{r=0}^{s-1} V_r(\theta, t) \quad \ldots\ldots(26)$$

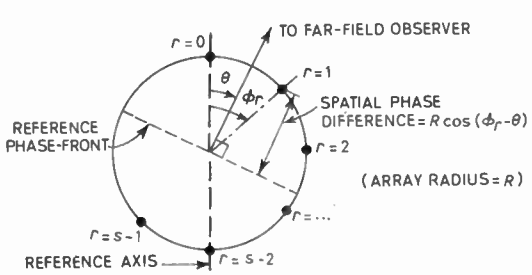

Fig. 27. Geometry of circular-arc array.

The jω-notation will be used to give the directional pattern. Let

$$\psi_r = kR\left\{\cos(\phi_r-\theta)-\cos(\phi_r-\beta)\right\} \quad \ldots\ldots(27)$$

Then

$$V(\psi, t) = \cos\omega t\left\{\sum_{r=0}^{s-1}\cos\psi_r\right\} + \sin\omega t\left\{\sum_{r=0}^{s-1}\sin\psi_r\right\} \quad \ldots\ldots(28)$$

Thus the magnitude of the final resultant phasor is

$$|V_R(\psi)| = \left[\left(\sum_r \cos\psi_r\right)^2 + \left(\sum_r \sin\psi_r\right)^2\right]^{\frac{1}{2}} \quad \ldots(29)$$

which is clearly equivalent to $\left|\sum_r \exp(j\psi_r)\right|$. Similarly, the phase angle is $\tan^{-1}\left[\sum_r \cos\psi_r \Big/ \sum_r \sin\psi_r\right]$. The directional pattern of the array may therefore be written in complex notation:

$$V_R(\theta) = \sum_{r=0}^{s-1}\exp\left\{jkR\left[\cos(\phi_r-\theta)-\cos(\phi_r-\beta)\right]\right\} \quad \ldots\ldots(30)$$

Expansion of the exponent yields

$$V_R(\theta) = \sum_{r=0}^{s-1}\exp\left\{j2kR\left[\sin\phi_r\left(\sin\frac{\theta-\beta}{2}\cos\frac{\theta+\beta}{2}\right) - \cos\phi_r\left(\sin\frac{\theta-\beta}{2}\sin\frac{\theta+\beta}{2}\right)\right]\right\} \quad \ldots(31)$$

and further rearrangement gives

$$V_R(\theta) = \sum_{r=0}^{s-1}\exp\left\{j2kR\sin\left(\frac{\theta-\beta}{2}\right)\times \times\cos\left[\phi_r - \left(\frac{\theta+\beta+\pi}{2}\right)\right]\right\} \quad \ldots(32)$$

It will be noted that when $\theta = \beta$ the summation of the element outputs along a line perpendicular to θ gives unity output from each, and so

$$V_R(\theta = \beta) = s \quad \ldots\ldots(33)$$

(where s = number of elements in phased arc). As this is the maximum value of V_R, it is convenient to normalize all $V_R(\theta)$ values so that $V_R(\theta = \beta) = 1$:

$$D(\theta) = \frac{1}{s}\sum_{r=0}^{s-1}\exp\left[j2kR.\sin\left(\frac{\theta-\beta}{2}\right)\times \times\cos\left(\phi_r - \frac{\theta+\beta+\pi}{2}\right)\right] \quad \ldots(34)$$

It is now convenient to use the substitution

$$\exp(jx\cos\alpha) = J_0(x) + 2\sum_{n=1}^{\infty} j^n J_n(x)\cos n\alpha \quad \ldots(35)$$

and so

$$D(\theta) = \frac{1}{s}\sum_{r=0}^{s-1}\left\{J_0\left(2kR\sin\frac{\theta-\beta}{2}\right) + + 2\sum_{n=1}^{\infty} j^n J_n\left(2kR\sin\frac{\theta-\beta}{2}\right)\cos n(\phi_r-\delta)\right\} \quad \ldots\ldots(36)$$

where $\delta = (\theta+\beta+\pi)/2$. This may be simplified to:

$$D(\theta) = J_0\left(2kR\sin\frac{\theta-\beta}{2}\right) + \frac{2}{s}\sum_{n=1}^{\infty}\left\{j^n J_n\left(2kR\sin\frac{\theta-\beta}{2}\right)\sum_{r=0}^{s-1}\cos n(\phi_r-\delta)\right\} \quad \ldots\ldots(37)$$

The final summation $\sum_{r=0}^{s-1}\cos n(\phi_r-\delta)$ is most conveniently represented as a complex geometric progression:

$$S = \mathrm{Re}\left\{\exp(-jn\delta)\sum_{r=0}^{s-1}\exp(jn2\pi r/N)\right\} \quad \ldots(38)$$

where $\phi_r = 2\pi r/N$, and $2\pi/N$ is the element separation in radians. The sum of this complex g.p. is given by

$$S = \mathrm{Re}\left\{\exp(-jn\delta)\,.\,\frac{1-\exp[jn2\pi(s-1+1)/N]}{1-\exp[jn2\pi/N]}\right\} \quad \ldots\ldots(39)$$

and after some algebraic manipulation, this becomes

$$S = \frac{\sin n\delta}{2(1-\cos n2\pi/N)}\{\sin(n2\pi/N) + \sin(n2\pi(s-1)/N) - \sin(n2\pi s/N)\} + \frac{\cos n\delta}{2(1-\cos n2\pi/N)}\{1-\cos(n2\pi s/N) - \cos(n2\pi/N) + \cos(n2\pi(s-1)/N)\} \quad \ldots\ldots(40)$$

Substituting in the $D(\theta)$ expression,

$$D(\theta) = J_0\left(2kR\sin\frac{\theta-\beta}{2}\right) + \frac{2}{s}\sum_{n=1}^{\infty} j^n J_n\left(2kR\sin\frac{\theta-\beta}{2}\right).[C_n\cos n\delta + S_n\sin n\delta] \quad \ldots\ldots(41)$$

where S_n and C_n are the coefficients of $\sin n\delta$ and $\cos n\delta$, respectively, in the previous expression.

In the case of a complete circle of elements, C_n and S_n may be found relatively easily by using l'Hospital's Rule for the evaluation of fractions whose numerator and denominator simultaneously become zero. Since $s = N$ in this case,

$$S_n = \frac{\sin(n2\pi/N) + \sin((N-1)n2\pi/N) - \sin n2\pi}{2(1-\cos(n2\pi/N))} \quad \ldots\ldots(42a)$$

$$C_n = \frac{1-\cos n2\pi - \cos(n2\pi/N) + \cos((N-1)n2\pi/N)}{2(1-\cos(n2\pi/N))} \quad \ldots\ldots(42b)$$

Examination of the numerators shows that they are zero under all conditions of n. Furthermore, the denominators are finite for most values of n, and so

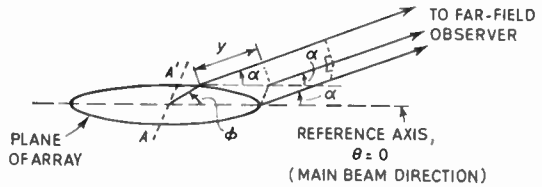

Fig. 28. Vertical plane geometry.

S_n and C_n are usually zero. However, for values given by

$$n = mN \quad \ldots\ldots(43)$$

(where m is any integer > 0) the numerators and denominators are both zero. The careful repeated use of l'Hospital's Rule [12] produces the results

$$C_{mN} = N,\quad S_{mN} = 0 \quad \text{(both factors are zero for } n \neq mN) \quad \ldots(44)$$

and so

$$D(\theta) = J_0\left(2kR\sin\frac{\theta-\beta}{2}\right) + 2\sum_{m=1}^{\infty} j^{mN} J_{mN}\left(2kR\sin\frac{\theta-\beta}{2}\right).\cos\frac{mN}{2}(\theta+\beta+\pi) \quad \ldots\ldots(45)$$

11.2. *The Vertical Radiation Pattern of a Phase-compensated Circular Array with an Infinite Number of Elements*

This appendix derives the vertical radiation pattern from a continuous circular aperture, in the plane of the main beam. Referring to Fig. 28 and taking AA' as the phase reference, the output from an element at ϕ is spatially advanced by

$$\psi_s = ky = (kR\cos\phi)\cos\alpha \quad \ldots\ldots(46)$$

Each individual element is electrically compensated by $-kR\cos\phi$ at any instant. The total far-field output is therefore

$$V(\alpha) = \int_0^{2\pi}\exp[jkR(\cos\phi.\cos\alpha - \cos\phi)]\,d\phi = 2\pi J_0[kR(1-\cos\alpha)] \quad \ldots\ldots(47)$$

This result follows from the standard integral

$$J_0(b) = \frac{1}{2\pi}\int_0^{2\pi}\exp(jb\cos\phi)\,d\phi$$

The maximum value of $V(\alpha)$ is clearly obtained when $\alpha = 0$ as expected, and then $V(0) = 2\pi$. Thus the normalized vertical directional pattern is

$$D_v(\alpha) = J_0[kR(1-\cos\alpha)] \quad \ldots\ldots(48)$$

Manuscript received by the Institution on 20th April 1965. (Paper No. 1003/RNA65).

U.D.C. 621.384.634

Characteristics of Oscillation of a Grounded-grid Synchrocyclotron Oscillator

By

D. N. BASU MALLIK, M.Sc.(Tech.)†

AND

B. R. NAG, M.Sc.(Tech.), M.S., D.Phil. (*Member*)‡

Summary: An analysis of a grounded-grid synchrocyclotron oscillator using a lumped equivalent circuit is presented. It is shown that for some circuit adjustments of the oscillator, oscillations may be excited at the dee resonant frequency, at the anode to dee coupling transmission line frequency, or simultaneously at both the frequencies. The excitation of simultaneous oscillations is explained by considering the tube non-linearities. Experimental results obtained from a model oscillator are also presented.

1. Introduction

In an earlier communication[1] the present authors made an analysis of a grounded-grid ordinary cyclotron oscillator using a lumped equivalent circuit and studied the characteristics of different modes of oscillations which may be excited in the oscillator. In the present paper the analysis is extended to the case of a synchrocyclotron oscillator which operates on the same principle as ordinary cyclotron oscillator but with different circuit arrangements.[4-11]

Sections 2 and 3 of the paper are devoted to the derivation of the equivalent circuit and the describing differential equations of a synchrocyclotron oscillator. The different frequencies of oscillation and the conditions of their maintenance are obtained in Section 4. It is found that in this case there are three possible frequencies of oscillations and for some conditions oscillations at the tube to dee coupling line frequencies may be excited.

In Section 5 the non-linearity in the tube characteristics is considered in order to determine the conditions under which the above-mentioned oscillations may be excited simultaneously with the dee-system frequency oscillations.

Experimental results obtained from a model oscillator are presented in Section 6.

2. The Schematic Circuit of a Practical Synchrocyclotron Oscillator and its Equivalent Circuit

The schematic circuit of the synchrocyclotron oscillator is shown in Fig. 1. The resonant system of the actual oscillator consists of a single dee, the dee stem and the variable capacitance at the other end of the dee stem. The anode and cathode of the oscillator are coupled by two short transmission lines to the resonant system through mutual inductances. The grid is grounded for radio frequencies.

The circuit which is equivalent to this oscillator system is shown in Fig. 2. The dee capacitance and the variable capacitance are denoted by C_d and C_v respectively. The dee stem is represented by the lumped inductance L. This replacement is not fully justified since the dee stem is of the order of $0{\cdot}3\lambda$. The analysis made here would thus give results which would be applicable only to the fundamental modes. The coupling transmission lines at the plate and the cathode side of the oscillator, together with loop inductances, are denoted by lumped inductances L_1 and L_2 respectively; C_{ag} and C_{gk} are the anode to grid and the grid to cathode capacitances of the tube; M_1 and M_2 are the mutual inductances of the anode and cathode loops respectively. The losses in the dee system is represented by the resistance R in parallel

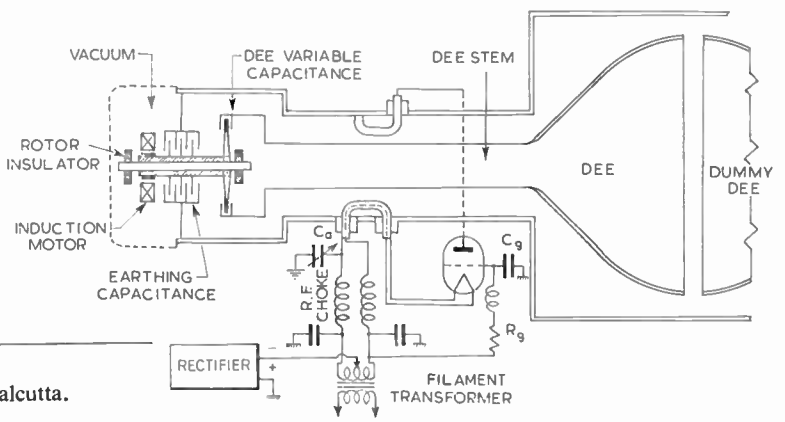

Fig. 1.
Schematic diagram of the synchrocyclotron oscillator.

† Saha Institute of Nuclear Physics, Calcutta.
‡ Institute of Radio Physics and Electronics, Calcutta.

to the dee capacitance C_d. C_a is the capacitance placed in series with the filament circuit for correcting the phases of the voltages appearing between the anode and cathode.

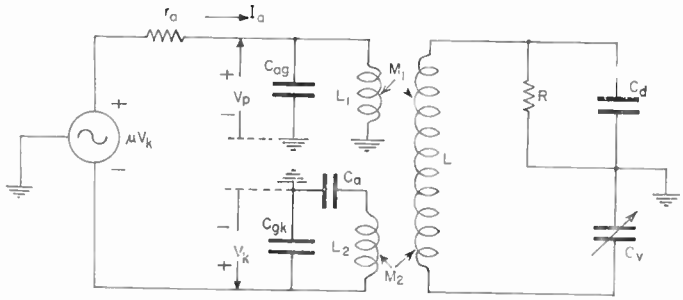

Fig. 2. Equivalent circuit of the oscillator.

3. Describing Differential Equations of the Oscillator

Let V_a and V_k be the voltages appearing at the anode and cathode side of the oscillator as shown in Fig. 2. The anode current, I_a and the grid current, I_g, are functions of the voltages V_a and V_k and let these be denoted by

$$I_a = \mathrm{f}_a(V_a, V_k) \qquad \ldots\ldots(1)$$

$$I_g = \mathrm{f}_g(V_a, V_k) \qquad \ldots\ldots(2)$$

By methods similar to those used in reference 1, it can be shown that the describing differential equations of the oscillator, expressed in terms of V_a and V_k, are given by

$$\left[\left(\frac{T}{\omega_1^2}-\frac{1}{\omega_3^2}\right)\frac{\mathrm{d}^5}{\mathrm{d}t^5}+a\left(\frac{T}{\omega_1^2}-\frac{1}{\omega_3^2}\right)\frac{\mathrm{d}^4}{\mathrm{d}t^4}+T\left(1+\frac{\omega_0^2}{\omega_1^2}\right)\frac{\mathrm{d}^3}{\mathrm{d}t^3}+T\left(a+a_1\frac{\omega_0^2}{\omega_1^2}\right)\frac{\mathrm{d}^2}{\mathrm{d}t^2}+(\omega_0^2T)\frac{\mathrm{d}}{\mathrm{d}t}+a_1\omega_0^2T\right]V_a+$$

$$+\left[\frac{1}{\omega_4^2}\cdot\frac{\mathrm{d}^5}{\mathrm{d}t^5}+\frac{a}{\omega_4^2}\cdot\frac{\mathrm{d}^4}{\mathrm{d}t^4}\right]V_k=\left[(TL_1-M_1)\frac{\mathrm{d}^4}{\mathrm{d}t^4}+a(TL_1-M_1)\frac{\mathrm{d}^3}{\mathrm{d}t^3}+(TL_1\omega_0^2)\frac{\mathrm{d}^2}{\mathrm{d}t^2}+(TL_1a_1\omega_0^2)\frac{\mathrm{d}}{\mathrm{d}t}\right]\times$$

$$\times\{\mathrm{f}_a(V_a,V_k)\}-\left[M_2\left(\frac{\mathrm{d}^4}{\mathrm{d}t^4}+a\frac{\mathrm{d}^3}{\mathrm{d}t^3}\right)\right]\{\mathrm{f}_a(V_a,V_k)+\mathrm{f}_g(V_a,V_k)\} \qquad \ldots\ldots(3)$$

$$\left[K\left(\frac{1}{\omega_1^2}\cdot\frac{\mathrm{d}^3}{\mathrm{d}t^3}+\frac{\mathrm{d}}{\mathrm{d}t}\right)\right]V_a+\left[\frac{1}{\omega_2^2}\cdot\frac{\mathrm{d}^3}{\mathrm{d}t^3}+K_1\frac{\mathrm{d}}{\mathrm{d}t}\right]V_k$$

$$=\left[\left(KL_1\frac{\mathrm{d}^2}{\mathrm{d}t^2}\right)\{\mathrm{f}_a(V_a,V_k)\}-\left(L_2\cdot\frac{\mathrm{d}^2}{\mathrm{d}t^2}+\frac{1}{C_a}\right)\{\mathrm{f}_a(V_a,V_k)+\mathrm{f}_g(V_a,V_k)\}\right] \qquad \ldots\ldots(4)$$

where

$$\omega_1^2=\frac{1}{L_1C_{ag}},\quad \omega_2^2=\frac{1}{L_2C_{gk}},\quad \omega_3^2=\frac{1}{M_1C_{ag}},\quad \omega_4^2=\frac{1}{M_2C_{gk}},$$

$$\omega_0^2=\frac{1}{L}\left(\frac{1}{C_d}+\frac{1}{C_v}\right),\quad a=\frac{1}{RC_d},\quad a_1=\frac{1}{R(C_d+C_v)},\quad T=\frac{L}{M_1},$$

$$K=\frac{M_2}{M_1},\quad a_1\omega_0^2=\frac{1}{LRC_vC_d},\quad K_1=\frac{C_a+C_{gk}}{C_a} \qquad \ldots\ldots(5)$$

It may be noted that eqns. (3) and (4), when combined give an equation of order seven. The oscillator system has therefore three possible frequencies of oscillation, which would be close to ω_1, ω_2 and ω_0. Among these ω_0, the dee system frequency, is the desired frequency while ω_1 and ω_2, the anode and cathode line frequencies, are the undesired ones. The conditions under which each of these three frequencies are excited may be obtained by analysing eqns. (3) and (4). In this analysis the tube characteristics are assumed to be linear. One may hence write

$$\mathrm{f}_a(V_a,V_k)=\left(g_m+\frac{1}{r_a}\right)V_k-\frac{V_a}{r_a} \qquad \ldots\ldots(6)$$

and

$$\{\mathrm{f}_a(V_a,V_k)+\mathrm{f}_g(V_a,V_k)\}=\left(g_m+\frac{1}{r_a}+\frac{1}{r_g}\right)V_k-\frac{V_a}{r_a} \qquad \ldots\ldots(7)$$

In the above equation g_m, r_a and r_g represent respectively the average values of mutual conductance, anode resistance and grid resistance corresponding to the equilibrium amplitudes of oscillation.

Substituting these values in eqns. (3) and (4) one obtains,

$$\left[\left(\frac{T}{\omega_1^2}-\frac{1}{\omega_3^2}\right)\frac{d^5}{dt^5}+\left(\frac{aT}{\omega_1^2}-\frac{a}{\omega_3^2}-h_2+b_2T-c_2\right)\frac{d^4}{dt^4}+\left(T+\frac{\omega_0^2T}{\omega_1^2}-ah_2-ac_2+ab_2T\right)\frac{d^3}{dt^3}+\right.$$
$$+\left(aT+\frac{a_1\omega_0^2T}{\omega_1^2}+b_2\omega_0^2T\right)\frac{d^2}{dt^2}+\omega_0^2T(1+a_1b_2)\frac{d}{dt}+a_1\omega_0^2T\Big]V_a+$$
$$+\left[\frac{1}{\omega_4^2}\cdot\frac{d^5}{dt^5}+\left(\frac{a}{\omega_4^2}+h_1+c_1-b_1T\right)\frac{d^4}{dt^4}+(ah_1+ac_1-ab_1T)\frac{d^3}{dt^3}-(\omega_0^2b_1T)\frac{d^2}{dt^2}-\right.$$
$$\left.-(a_1b_1\omega_0^2T)\frac{d}{dt}\right]V_k=0 \quad \text{.....(8)}$$

and

$$\left[\frac{K}{\omega_1^2}\cdot\frac{d^3}{dt^3}+(Kb_2-b_4)\frac{d^2}{dt^2}+K\cdot\frac{d}{dt}-c_4\right]V_a+\left[\frac{1}{\omega_2^2}\cdot\frac{d^3}{dt^3}+(b_3-Kb_1)\frac{d^2}{dt^2}+K_1\frac{d}{dt}+c_3\right]V_k=0 \quad \text{.....(9)}$$

where

$$\left.\begin{aligned} b_1&=L_1\left(g_m+\frac{1}{r_a}\right), & b_2&=\frac{L_1}{r_a}, & h_1&=M_1\left(g_m+\frac{1}{r_a}\right), & h_2&=\frac{M_1}{r_a}\\ c_1&=M_2\left(g_m+\frac{1}{r_a}+\frac{1}{r_g}\right), & c_2&=\frac{M_2}{r_a}, & b_3&=L_2\left(g_m+\frac{1}{r_a}+\frac{1}{r_g}\right)\\ b_4&=\frac{L_2}{r_a}, & c_3&=\frac{1}{C_a}\left(g_m+\frac{1}{r_a}+\frac{1}{r_g}\right), & c_4&=\frac{1}{r_aC_a}\end{aligned}\right\} \quad \text{.....(10)}$$

Eliminating one of the variables from eqns. (8) and (9), replacing d/dt by $j\omega$, and equating the real and imaginary parts of the resultant equation separately to zero one gets

$$\left[\left(\frac{K}{\omega_1^2\omega_4^2}+\frac{1}{\omega_2^2\omega_3^2}-\frac{T}{\omega_1^2\omega_2^2}\right)\omega^6-\left\{K_1\left(\frac{1}{\omega_3^2}-\frac{T}{\omega_1^2}\right)+\left(\frac{K}{\omega_4^2}-\frac{T}{\omega_2^2}\right)-\frac{\omega_0^2T}{\omega_1^2\omega_2^2}\right\}\omega^4-\right.$$
$$\left.-\left\{K_1T\left(1+\frac{\omega_0^2}{\omega_1^2}\right)+\frac{\omega_0^2T}{\omega_2^2}\right\}\omega^2+\omega_0^2K_1T\right]=0 \quad \text{.....(11}$$

and

$$\left[a\left\{\frac{K\omega^4}{\omega_4^2}\cdot\frac{(\omega^2-\omega_1^2)}{\omega_1^2}+\frac{\omega^4(\omega^2-K_1\omega_2^2)}{\omega_2^2\omega_3^2}-\frac{(\omega^2-\omega_1^2)(\omega^2-K_1\omega_2^2)}{\omega_1^2\omega_2^2}\cdot\omega^2T\right\}+\right.$$
$$+a_1\omega_0^2T\left\{\frac{(\omega^2-\omega_1^2)(\omega^2-K_1\omega_2^2)}{\omega_1^2\omega_2^2}\right\}-Kb_1\frac{\omega^6}{\omega_3^2}+b_2\left\{\frac{K\omega^6}{\omega_4^2}-\frac{\omega^2T(\omega^2-\omega_0^2)(\omega^2-K_1\omega_2^2)}{\omega_2^2}\right\}+$$
$$+b_3\left\{\frac{\omega^6}{\omega_3^2}-\frac{T\omega^2(\omega^2-\omega_0^2)(\omega^2-\omega_1^2)}{\omega_1^2}\right\}-b_4\frac{\omega^6}{\omega_4^2}+K(h_1+c_1)\frac{\omega^4(\omega^2-\omega_1^2)}{\omega_1^2}+$$
$$\left.+(h_2+c_2)\frac{(\omega^2-K_1\omega_2^2)\omega^4}{\omega_2^2}-c_3\left\{\frac{\omega^4}{\omega_3^2}-\frac{T(\omega^2-\omega_0^2)(\omega^2-\omega_1^2)}{\omega_1^2}\right\}+c_4\frac{\omega^4}{\omega_4^2}\right.=0 \quad \text{.....(12)}$$

Values of ω satisfying eqn. (11) are the frequencies at which steady oscillations are possible. The relations between the tube parameters, dee system loss and the coupling with the dee system which ensure oscillations at these frequencies are obtained from eqn. (12) by replacing ω by the roots of eqn. (11).

4. Frequencies of Oscillation and the Equilibrium Conditions

The roots of eqn. (11) give the frequencies of oscillations. Equation (11) is a cubic equation and the roots may be expressed in analytical form in terms of the coefficients of ω. However, it should be noted that $1/\omega_3^2$ and $1/\omega_4^2$ are, in general, much too small compared to the other terms. When these terms are completely neglected, eqn. (11) reduces to

$$(\omega^2-\omega_0^2)(\omega^2-\omega_1^2)(\omega^2-K_1\omega_2^2)=0 \quad \text{.....(13)}$$

Under this condition the roots are identical to ω_0, ω_1 and $\sqrt{K_1}\,\omega_2$, as expected. The terms containing $1/\omega_3^2$ and $1/\omega_4^2$ cannot be completely neglected in practice, but one may assume that the actual roots of eqn. (11) deviate from those of eqn. (13) by small amounts. Under this condition it may be shown that to the first order of approximation frequencies of oscillation are given by

$$\omega_{10}^2 = \omega_0^2 + \Delta\omega_{10} = \omega_0^2 + \frac{\omega_0^4}{T}\left\{\frac{\omega_1^2.\Delta\omega_3}{(\omega_0^2-\omega_1^2)} + \frac{K\omega_2^2.\Delta\omega_4}{(\omega_0^2-K_1\omega_2^2)}\right\} \qquad \text{.....(14)}$$

$$\omega_{11}^2 = \omega_1^2 + \Delta\omega_{11} = \omega_1^2 + \frac{\omega_1^4}{T}\cdot\frac{\omega_1^2.\Delta\omega_3}{(\omega_1^2-\omega_0^2)} \qquad \text{.....(15)}$$

$$\omega_{12}^2 = K_1\omega_2^2 + \Delta\omega_{12} = K_1\omega_2^2 + \frac{K_1^2\omega_2^4}{T}\cdot\frac{K\omega_2^2\Delta\omega_4}{(K_1\omega_2^2-\omega_0^2)} \qquad \text{.....(16)}$$

where $\Delta\omega_3$ and $\Delta\omega_4$ are equal to $1/\omega_3^2$ and $1/\omega_4^2$ respectively.

Equations (14) to (16) together with eqn. (13) thus give the three possible frequencies of oscillation.

In order that oscillations be maintained at these frequencies, it is necessary that each of these roots should also satisfy eqn. (12).

On substituting the above roots in eqn. (12) one obtains

$$(a_1-a)\alpha_1\alpha_2 = \omega_0^2\cdot\frac{M_1M_2}{L}\left(g_m+\frac{2}{r_a}\right) + \frac{M_1^2}{Lr_a}\cdot\frac{\alpha_2}{\alpha_1}\cdot\omega_0^2 + \omega_0^2\cdot\frac{M_2^2}{L}\cdot\frac{\alpha_1}{\alpha_2}\left(g_m+\frac{1}{r_a}+\frac{1}{r_g}\right) \qquad \text{.....(17)}$$

$$(a_1-a)\frac{\omega_0^2}{\omega_1^2}\cdot\frac{1}{\beta_1^2} = \omega_1^2\cdot\frac{M_2}{M_1}\cdot\frac{L_1}{\beta_1\beta_2}\left(g_m+\frac{2}{r_a}\right) + \frac{\omega_1^2L_1}{r_a}\left[\frac{LL_1}{M_1^2}+\frac{1}{\beta_1^2}+\frac{\omega_1^2}{\omega_2^2\beta_1\beta_2}\left(1-\frac{L_1M_2^2}{L_2M_1^2}\right)\right] \qquad \text{.....(18)}$$

$$(a_1-a)\frac{\omega_0^2}{\omega_2^2}\cdot\frac{1}{\gamma_2^2} = K_1\omega_2^2\cdot\frac{M_1}{M_2}\cdot\frac{L_2}{\gamma_1\gamma_2}\left(g_m+\frac{2}{r_a}\right) + \omega_2^2L_2\left(g_m+\frac{1}{r_a}+\frac{1}{r_g}\right)\left[\frac{LL_2}{M_2^2}+\frac{1}{\gamma_2^2}+\frac{K_1\omega_2^2}{\omega_1^2\gamma_1\gamma_2}\left(1-\frac{L_2M_1^2}{L_1M_2^2}\right)\right] \qquad \text{...(19)}$$

where

$$\alpha_1 = \frac{(\omega_0^2-\omega_1^2)}{\omega_1^2}, \qquad \alpha_2 = \frac{(\omega_0^2-K_1\omega_2^2)}{\omega_2^2}$$

$$\beta_1 = \frac{(\omega_1^2-\omega_0^2)}{\omega_1^2}, \qquad \beta_2 = \frac{(\omega_1^2-K_1\omega_2^2)}{\omega_2^2}$$

$$\gamma_1 = \frac{(K_1\omega_2^2-\omega_1^2)}{\omega_1^2}, \qquad \gamma_2 = \frac{(K_1\omega_2^2-\omega_0^2)}{K_1\omega_2^2}$$

Equations (17), (18) and (19) give respectively the conditions for stable oscillations at the frequencies corresponding to dee system, anode line and cathode line respectively. The physical significance of these equations are discussed separately for each case below.

4.1. *Conditions for Oscillation at* ω_{10}

The terms a and a_1 in the left-hand side of the above equations represent the actual losses in the resonant circuit of the oscillator. The terms on the right-hand side containing M_1 and M_2 represent the compensation due to feedback. For maintenance of stable oscillations at any one of the above three modes, the right-hand side term of the corresponding equation, representing the regenerative feedback should be equal to or larger than that of the left-hand side term.

Remembering the above-mentioned point the condition for stable oscillation at ω_{10} may be obtained from eqn. (17) in the following manner. One notes that ω_1 and $\sqrt{K_1}\,\omega_2$ are both greater than ω_0, hence α_1 and α_2 are negative. The left-hand side of the equation is always negative since $a > a_1$ and the product term $\alpha_1\alpha_2$ is positive. Hence, oscillations at ω_{10} may be maintained if the first term on the right-hand side of eqn. (17) is negative and greater than the sum of the other two terms, which are small and positive terms. This requires that the product M_1M_2 should be negative and $M_1 > M_2$. In synchrocyclotron oscillators, therefore, oscillation at the dee system frequency ω_{10} will be possible if the anode and cathode loops are connected in opposite senses with mutual coupling in the anode side greater than that at the cathode side.

4.2. *Conditions for Oscillations at* ω_{11} *and* ω_{12}

The term β_1 on the left-hand side of eqn. (18) is always positive and $a > a_1$; hence the left-hand side term of the equation is negative. On examining the right-hand side of the equation, one may conclude that the first term is to be negative for equilibrium conditions to exist at ω_{11}. Now, since M_1 and M_2

have opposite signs, the first term on the right-hand side will be negative if $\beta_1\beta_2$ is positive; but β_1 is positive hence β_2 must also be positive. Hence, for maintenance of oscillations at ω_{11} the anode transmission line frequency ω_1 is required to be higher than that of the cathode line frequency $\sqrt{K_1}\,\omega_2$. It may also be noted that if the losses due to the dee system are less predominant than the other terms the value of M_1 required for maintenance of oscillations at ω_{11} would decrease with increase in the value of M_2.

On examining eqn. (19) one can similarly argue and show that steady oscillation at ω_{12} will be possible if γ_1 is positive, i.e. the cathode line frequency is higher than the anode line frequency. It may also be noted that the second term of eqn. (19) is larger than the corresponding term in eqn. (18). Hence, out of the two transmission line modes, ω_{11} and ω_{12}, oscillations are more easily excitable at ω_{11} than at ω_{12}.

5. Consideration of Non-linearity

The possible frequencies of oscillations have been determined in the preceding section considering the linearized parameters of the tube. It has been found that for some oscillator adjustments there are two possible frequencies of oscillation. In order to determine whether under these conditions oscillations will be excited simultaneously at both the frequencies, the non-linear characteristics of the tube has to be taken into consideration. In this section the effect of this non-linearity is discussed.

In order to simplify the analysis it is assumed that the contribution of non-linearity is small and a first-order approximate analysis is applicable. Equations (6) and (7) under this assumption may be replaced by

$$f_a(V_a, V_k) = \left(g_m + \frac{1}{r_a}\right) V_k - \frac{V_a}{r_a} + f_1(V_a, V_k) \qquad \text{.....(20)}$$

$$f_g(V_a, V_k) = \frac{V_k}{r_g} + f_2(V_a, V_k) \qquad \text{.....(21)}$$

where $f_1(V_a, V_k)$ and $f_2(V_a, V_k)$ are non-linear functions determined by the tube characteristics.

Replacing $f_a(V_a, V_k)$ and $f_g(V_a, V_k)$ in (3) and (4) by the above expressions, combining the equations and collecting the first-order terms on one side, one obtains

$$\left(\alpha_7\frac{d^7V_k}{dt^7} + \alpha_5\frac{d^5V_k}{dt^5} + \alpha_3\frac{d^3V_k}{dt^3} + \alpha_1\frac{dV_k}{dt}\right) = \left(\beta_6\frac{d^6V_k}{dt^6} + \beta_4\frac{d^4V_k}{dt^4} + \beta_2\frac{d^2V_k}{dt^2} + \beta_0V_k\right) +$$
$$+ \left(\gamma_6\frac{d^6}{dt^6} + \gamma_4\frac{d^4}{dt^4} + \gamma_2\frac{d^2}{dt^2}\right)\{f_1(V_a, V_k)\} + \left(\delta_6\frac{d^6}{dt^6} + \delta_4\frac{d^4}{dt^4} + \delta_2\frac{d^2}{dt^2}\right)\{f_2(V_a, V_k)\} \qquad \text{.....(22)}$$

where

$$\alpha_7 = \left(\frac{K}{\omega_1^2\omega_4^2} + \frac{1}{\omega_2^2\omega_3^2} - \frac{T}{\omega_1^2\omega_2^2}\right) \qquad \alpha_5 = \left\{\left(\frac{1}{\omega_3^2} - \frac{T}{\omega_1^2} + \frac{K}{\omega_4^2} - \frac{T}{\omega_2^2}\right) - \frac{\omega_0^2T}{\omega_1^2\omega_2^2}\right\}$$

$$\alpha_3 = -\left\{T\left(1 + \frac{\omega_0^2}{\omega_1^2}\right) + \frac{\omega_0^2T}{\omega_2^2}\right\} \qquad \alpha_1 = -\omega_0^2T$$

$$\beta_6 = -\left\{a\left(\frac{K}{\omega_1^2\omega_4^2} + \frac{1}{\omega_2^2\omega_3^2} - \frac{T}{\omega_1^2\omega_2^2}\right) - \frac{Kb_1}{\omega_3^2} + b_3\left(\frac{1}{\omega_3^2} - \frac{T}{\omega_1^2}\right) + \frac{K}{\omega_1^2}(h_1 + c_1)\right\}$$

$$\beta_4 = -\left\{a\left(\frac{K}{\omega_4^2} - \frac{T}{\omega_1^2} + \frac{1}{\omega_3^2} - \frac{T}{\omega_2^2}\right) - \frac{a_1\omega_0^2T}{\omega_1^2\omega_2^2} - b_2T\left(1 + \frac{\omega_0^2}{\omega_2^2}\right) - b_3T\left(1 + \frac{\omega_0^2}{\omega_1^2}\right) + K(h_1 + c_1)\right\}$$

$$\beta_2 = \left\{aT + \omega_0^2T(b_2 + b_3) + a_1\omega_0^2T\left(\frac{1}{\omega_1^2} + \frac{1}{\omega_2^2}\right)\right\} \qquad \beta_0 = a_1\omega_0^2T,$$

$$\gamma_6 = \left\{\frac{1}{\omega_3^2}(KL_1 - L_2) + \frac{1}{\omega_1^2}(TL_2 - KM_1 - KM_2)\right\} \qquad \gamma_4 = \left\{L_2T\left(1 + \frac{\omega_0^2}{\omega_1^2}\right) - K(M_1 + M_2)\right\}$$

$$\gamma_2 = \omega_0^2L_2T \qquad \delta_6 = \left\{\frac{1}{\omega_1^2}(TL_2 - KM_2) - \frac{L_2}{\omega_3^2}\right\}$$

$$\delta_4 = \left\{L_2T\left(1 + \frac{\omega_0^2}{\omega_1^2}\right) - KM_2\right\} \qquad \delta_2 = \omega_0^2L_2T$$

It has been shown that when the right-hand side terms are zero, the equation admits oscillations at three frequencies ω_{10}, ω_{11}, and ω_{12}. For any particular adjustment of the oscillator of these three, oscillations at only two frequencies are possible. Let these frequencies be ω_{10} and ω_{11}. The effect of the non-linearity may be studied by assuming the following as the generating solution,[2]

$$V_k = A\sin(\omega_{10}t+\phi) + B\sin(\omega_{11}t+\theta) \qquad \text{.....(23)}$$

In eqn. (23) A, ϕ, B and θ are assumed to be time dependent. On substituting (23) in (22) and collecting only the first-order terms one obtains

$$\left(\frac{dA}{dt}\right) = p_1A + q_1(A,B) \qquad \text{.....(24)}$$

$$A\left(\frac{d\phi}{dt}\right) = r_1(A,B) \qquad \text{.....(25)}$$

$$\left(\frac{dB}{dt}\right) = p_2B + q_2(A,B) \qquad \text{.....(26)}$$

$$B\left(\frac{d\theta}{dt}\right) = r_2(A,B) \qquad \text{.....(27)}$$

where

$$p_1 = \frac{(\beta_6\omega_{10}^6 - \beta_4\omega_{10}^4 + \beta_2\omega_{10}^2 - \beta_0)}{(6\alpha_7\omega_{10}^6 - 4\alpha_5\omega_{10}^4 + 2\alpha_3\omega_{10}^2)}; \qquad p_2 = \frac{(\beta_6\omega_{11}^6 - \beta_4\omega_{11}^4 + \beta_2\omega_{11}^2 - \beta_0)}{(6\alpha_7\omega_{11}^6 - 4\alpha_5\omega_{11}^4 + 2\alpha_3\omega_{11}^2)}$$

$$q_1(A,B) = \frac{(\gamma_6\omega_{10}^4 - \gamma_4\omega_{10}^2 + \gamma_2)}{(6\alpha_7\omega_{10}^4 - 4\alpha_5\omega_{10}^2 + 2\alpha_3)}\left[\frac{1}{\pi}\int_0^{2\pi} f_1(V_a, V_k)\sin(\omega_{10}t+\phi)\,dt\right] + \\ + \frac{(\delta_6\omega_{10}^4 - \delta_4\omega_{10}^2 + \delta_2)}{(6\alpha_7\omega_{10}^4 - 4\alpha_5\omega_{10}^2 + 2\alpha_3)}\left[\frac{1}{\pi}\int_0^{2\pi} f_2(V_a, V_k)\sin(\omega_{10}t+\phi)\,dt\right]$$

$$r_1(A,B) = \frac{(\gamma_6\omega_{10}^4 - \gamma_4\omega_{10}^2 + \gamma_2)}{(6\alpha_7\omega_{10}^4 - 4\alpha_5\omega_{10}^2 + 2\alpha_3)}\left[\frac{1}{\pi}\int_0^{2\pi} f_1(V_a, V_k)\cos(\omega_{10}t+\phi)\,dt\right] + \\ + \frac{(\delta_6\omega_{10}^4 - \delta_4\omega_{10}^2 + \delta_2)}{(6\alpha_7\omega_{10}^4 - 4\alpha_5\omega_{10}^2 + 2\alpha_3)}\left[\frac{1}{\pi}\int_0^{2\pi} f_2(V_a, V_k)\cos(\omega_{10}t+\phi)\,dt\right]$$

$$q_2(A,B) = \frac{(\gamma_6\omega_{11}^4 - \gamma_4\omega_{11}^2 + \gamma_2)}{(6\alpha_7\omega_{11}^4 - 4\alpha_5\omega_{11}^2 + 2\alpha_3)}\left[\frac{1}{\pi}\int_0^{2\pi} f_1(V_a, V_k)\sin(\omega_{11}t+\theta)\,dt\right] + \\ + \frac{(\delta_6\omega_{11}^4 - \delta_4\omega_{11}^2 + \delta_2)}{(6\alpha_7\omega_{11}^4 - 4\alpha_5\omega_{11}^2 + 2\alpha_3)}\left[\frac{1}{\pi}\int_0^{2\pi} f_2(V_a, V_k)\sin(\omega_{11}t+\theta)\,dt\right]$$

$$r_2(A,B) = \frac{(\gamma_6\omega_{11}^4 - \gamma_4\omega_{11}^2 + \gamma_2)}{(6\alpha_7\omega_{11}^4 - 4\alpha_5\omega_{11}^2 + 2\alpha_3)}\left[\frac{1}{\pi}\int_0^{2\pi} f_1(V_a, V_k)\cos(\omega_{11}t+\theta)\,dt\right] + \\ + \frac{(\delta_6\omega_{11}^4 - \delta_4\omega_{11}^2 + \delta_2)}{(6\alpha_7\omega_{11}^4 - 4\alpha_5\omega_{11}^2 + 2\alpha_3)}\left[\frac{1}{\pi}\int_0^{2\pi} f_2(V_a, V_k)\cos(\omega_{11}t+\theta)\,dt\right]$$

In the actual adjustment of the oscillator, possibility of simultaneous oscillations arise when p_1 and p_2 are both positive. The equilibrium amplitudes of oscillations A and B are obtained from the following equations

$$p_1A + q_1(A,B) = 0 \qquad \text{.....(28)}$$

$$p_2B + q_2(A,B) = 0 \qquad \text{.....(29)}$$

The frequencies of oscillation are obtained from eqns. (25) and (27) by substituting the values of q_1, q_2, r_1 and r_2 for the equilibrium values of A and B.

In order that simultaneous oscillations be possible it is required that for the equilibrium conditions the following two equations are satisfied

$$p_1 + \frac{\partial}{\partial A}\cdot\{q_1(A,B)\} + p_2 + \frac{\partial}{\partial B}\{q_2(A,B)\} < 0 \qquad \text{...(30)}$$

$$\left[p_1 + \frac{\partial}{\partial A}\{q_1(A,B)\}\right]\left[p_2 + \frac{\partial}{\partial B}\{q_2(A,B)\}\right] \\ - \left[\frac{\partial}{\partial B}\{q_1(A,B)\}\cdot\frac{\partial}{\partial A}\{q_2(A,B)\}\right] > 0 \qquad \text{.....(31)}$$

All the differential coefficients are to be evaluated for the equilibrium values of A and B.

Further discussion about the stability of simultaneous oscillation may be made when the non-linear terms q_1 and q_2 are completely known. It may be easily shown that, when the non-linearity is of the cubic type, simultaneous oscillations become unstable and hence the oscillator will not execute simultaneous oscillations but at either ω_{10} or ω_{11}, the actual frequency being determined by initial conditions.

Since in the actual oscillator the bias is introduced by grid-leak arrangement it is difficult to express the functions f_1 and f_2 analytically. The nature of the functions may, however, be determined experimentally by introducing some simplifications. It may be assumed that the effect of V_a and also that of the grid current is small. The main limiting is introduced by the non-linear character of the mutual characteristics. This may be obtained experimentally by using audio frequency signals.

The grid leak biasing capacitance is replaced by a higher value capacitance so that the time-constant of the grid leak arrangement bears the same ratio to the audio frequencies as that of the original grid-leak arrangement with the radio frequencies. Two signals at audio frequencies having the same frequency

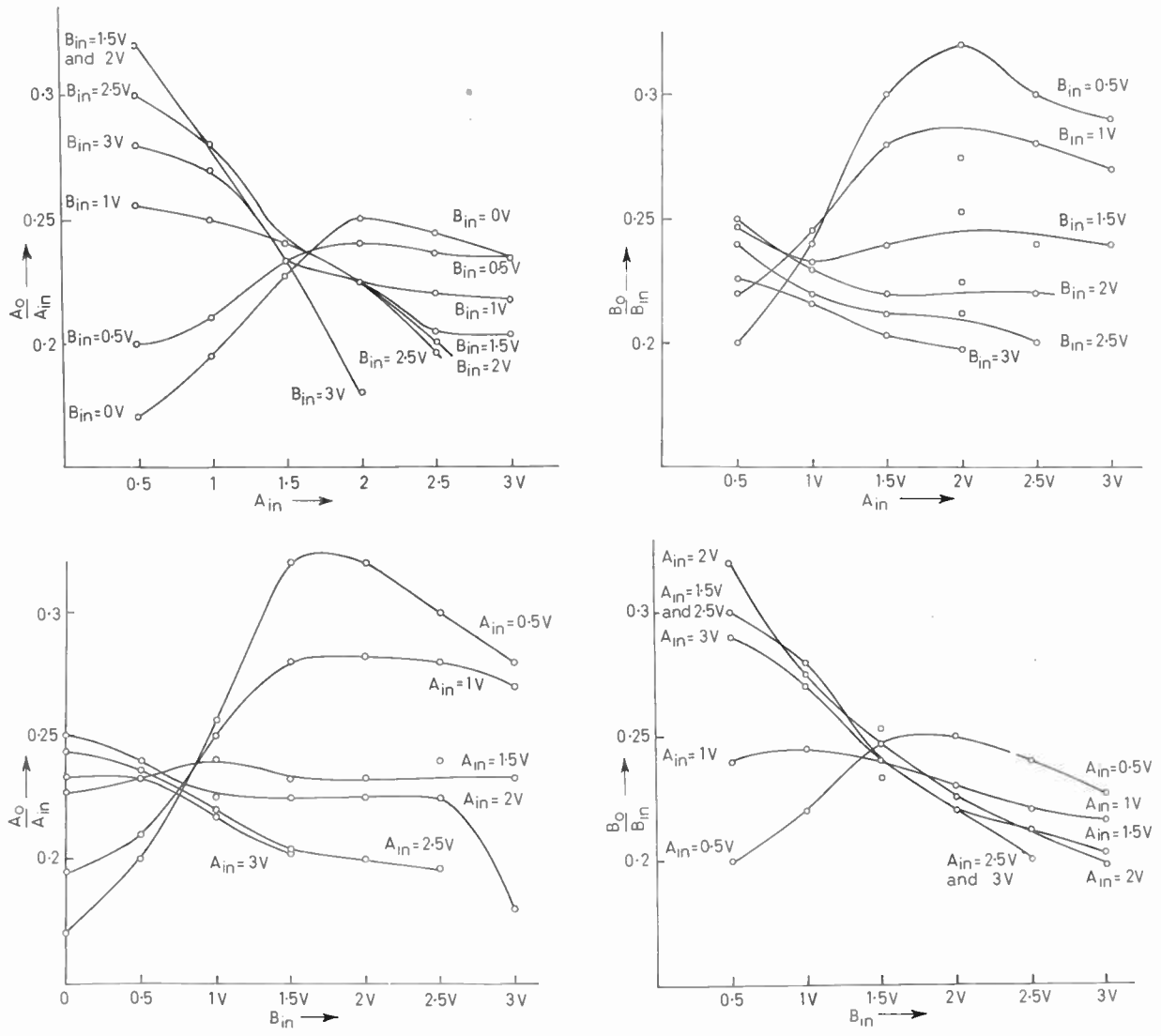

Fig. 3. Plots of the tube non-linearity.

A_{in} = input voltage of the low frequency signal.
A_o = output voltage of the low frequency signal.
B_{in} = input voltage of the high frequency signal.
B_o = output voltage of the high frequency signal.

ratio as the radio frequencies are applied in series with the grid leak resistance. The amplitude of one signal is kept constant and for different amplitudes of the other signal the outputs across a small resistance in the anode are determined for the two frequencies by a wave analyser. Plots obtained experimentally following the above procedure are shown in Fig. 3.

On examining the characteristics shown in Fig. 3 it is observed that these are of the same nature as would be obtained if the tube had a fifth-order polynomial type non-linearity with a positive cubic and a negative fifth-order term. The stability of simultaneous oscillations in the latter case have been discussed by Skinner.[3] It has been shown that for this non-linearity stable simultaneous oscillations may be obtained for some adjustments of the oscillator. Bearing this result in mind, one may conclude that in the present case also stable simultaneous oscillations would be possible.

One may thus conclude that in the cyclotron oscillator with grid leak bias arrangement under some adjustments simultaneous oscillations will be possible. The oscillation at the undesired frequency may, however, be eliminated by so adjusting the circuit elements that either p_2 is negative or it leads to a value of B which falls outside the stability range.

In order to test the conclusions drawn in the previous section an experimental oscillator was constructed and the results obtained from the study of this oscillator are given in the next Section.

6. Experimental Results

The circuit of the oscillator from which the experimental results were obtained is shown in Fig. 4. All the circuit elements are lumped elements but chosen to have values approximating to those of an actual synchrocyclotron oscillator. The circuit parameter values of an actual oscillator[4] and of the experimental oscillator are given in Table 1.

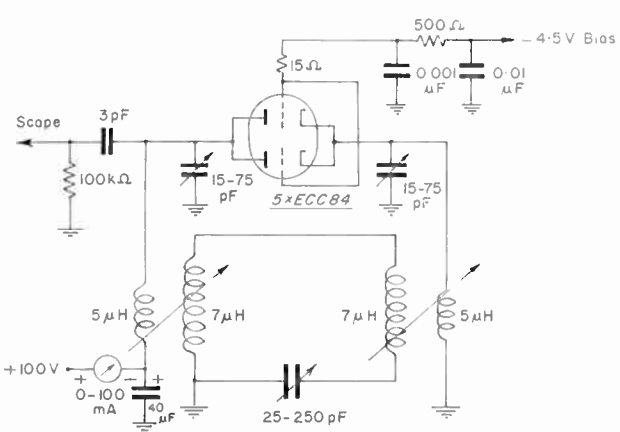

Fig. 4. Circuit arrangement of the experimental oscillator.

Table 1

Circuit parameter values of an actual and the experimental oscillator

Actual Oscillator	Experimental Oscillator
Tube: 9C21	Tubes: 10 × ECC84 (5 twin-triodes)
Mutual conductance: 50–60 mA/V	Mutual conductance: (10 × 6) mA/V
Amplification factor: 36	Amplification factor: 24
Anode-cathode capacitance: 2 pF	Anode-cathode capacitance: (10 × 0·45) pF
Anode-grid capacitance: 46 pF	Anode-grid capacitance: (10 × 1·2) pF
Grid-cathode capacitance: 100 pF	Grid-cathode capacitance: (10 × 2·1) pF
Dee resonant frequency: 13·5–9·5 Mc/s	Resonant frequency: 3·6 Mc/s
Inductance of the dee stem: 0·56 to 0·6 μH	Inductance simulating the dee stem: 14 μH
Q of the dee system: 1000–1200	Q of the resonant circuit: 200
Impedance of the dee system: 58 to 41 kΩ	Impedance of the resonant system: 60 kΩ

It may be noted from Table 1 that the tube parameters are approximately the same, and also the main resonant system impedances at the working frequency are nearly equal. The anode and cathode line frequencies which were kept variable in the experimental oscillator bore approximately the same ratio to the main resonant frequency as in an actual oscillator. The performance of the experimental oscillator may, therefore, be assumed to simulate an actual sychrocyclotron oscillator. However, there are two essential differences which should be mentioned. These are: (*a*) the screening between anode and cathode by the grid in an actual oscillator would be more effective because of constructional differences; (*b*) the lumped nature of the circuit elements in the experimental oscillator prevents excitation of harmonic modes which may be excited in an actual oscillator due to distributed parameter character of the circuit elements. However, in spite of these differences, the excitation of the essential modes which are being studied in this paper should be evident from the experimental oscillator.

The characteristics showing the excitation of the different modes as obtained from the experimental oscillator are shown in Fig. 5. These were obtained by setting a value of cathode mutual inductance M_2 and reducing the value of M_1 till a particular mode was extinguished and a new mode excited. This was repeated for different settings of M_2. M_1 was always varied in one direction to avoid hysteresis effect which was often found to be present. In Fig. 5 are displayed the different regions in the M_1–M_2 plane in which the

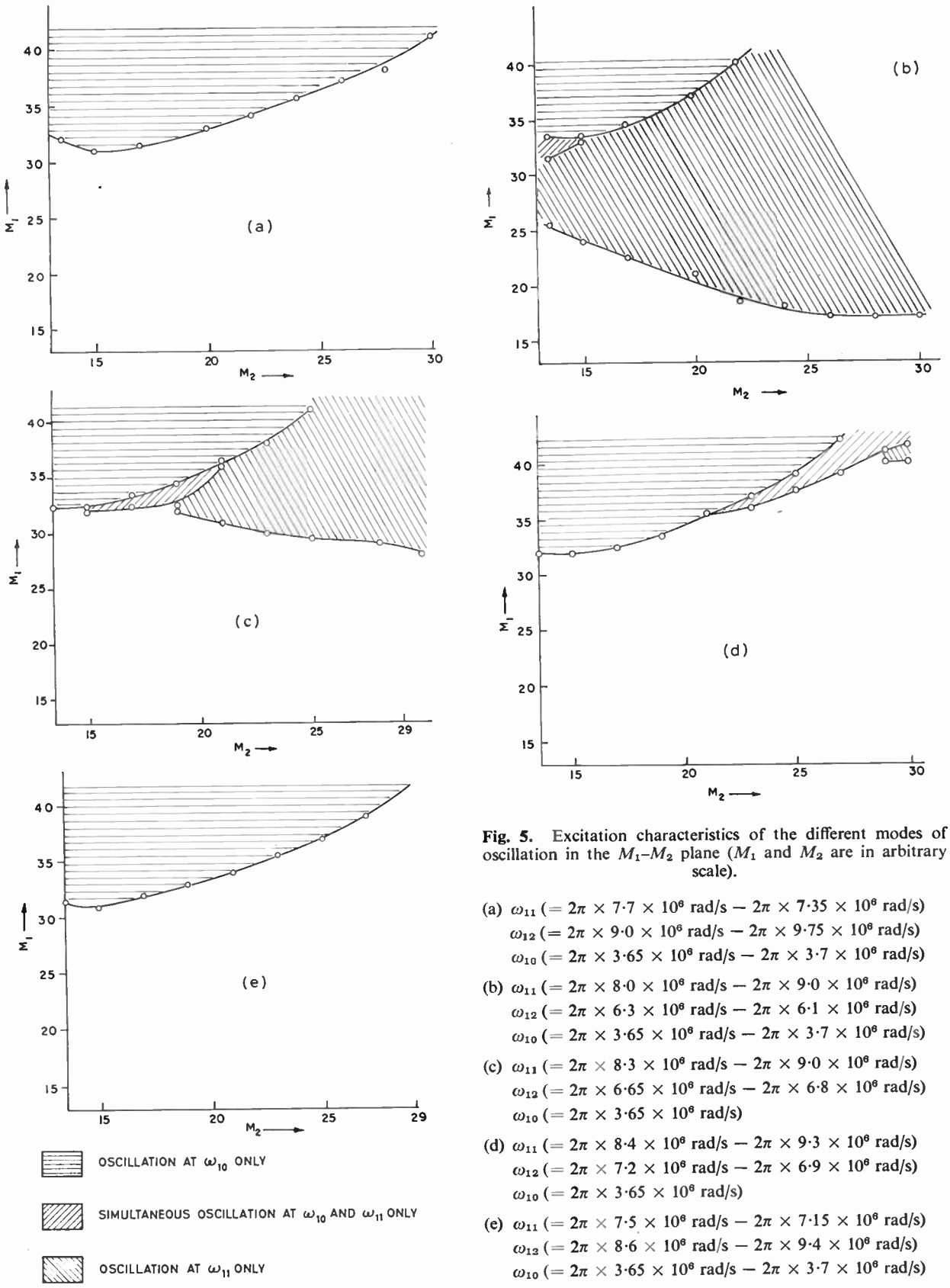

Fig. 5. Excitation characteristics of the different modes of oscillation in the M_1–M_2 plane (M_1 and M_2 are in arbitrary scale).

(a) ω_{11} ($= 2\pi \times 7{\cdot}7 \times 10^6$ rad/s $- 2\pi \times 7{\cdot}35 \times 10^6$ rad/s)
ω_{12} ($= 2\pi \times 9{\cdot}0 \times 10^6$ rad/s $- 2\pi \times 9{\cdot}75 \times 10^6$ rad/s)
ω_{10} ($= 2\pi \times 3{\cdot}65 \times 10^6$ rad/s $- 2\pi \times 3{\cdot}7 \times 10^6$ rad/s)

(b) ω_{11} ($= 2\pi \times 8{\cdot}0 \times 10^6$ rad/s $- 2\pi \times 9{\cdot}0 \times 10^6$ rad/s)
ω_{12} ($= 2\pi \times 6{\cdot}3 \times 10^6$ rad/s $- 2\pi \times 6{\cdot}1 \times 10^6$ rad/s)
ω_{10} ($= 2\pi \times 3{\cdot}65 \times 10^6$ rad/s $- 2\pi \times 3{\cdot}7 \times 10^6$ rad/s)

(c) ω_{11} ($= 2\pi \times 8{\cdot}3 \times 10^6$ rad/s $- 2\pi \times 9{\cdot}0 \times 10^6$ rad/s)
ω_{12} ($= 2\pi \times 6{\cdot}65 \times 10^6$ rad/s $- 2\pi \times 6{\cdot}8 \times 10^6$ rad/s)
ω_{10} ($= 2\pi \times 3{\cdot}65 \times 10^6$ rad/s)

(d) ω_{11} ($= 2\pi \times 8{\cdot}4 \times 10^6$ rad/s $- 2\pi \times 9{\cdot}3 \times 10^6$ rad/s)
ω_{12} ($= 2\pi \times 7{\cdot}2 \times 10^6$ rad/s $- 2\pi \times 6{\cdot}9 \times 10^6$ rad/s)
ω_{10} ($= 2\pi \times 3{\cdot}65 \times 10^6$ rad/s)

(e) ω_{11} ($= 2\pi \times 7{\cdot}5 \times 10^6$ rad/s $- 2\pi \times 7{\cdot}15 \times 10^6$ rad/s)
ω_{12} ($= 2\pi \times 8{\cdot}6 \times 10^6$ rad/s $- 2\pi \times 9{\cdot}4 \times 10^6$ rad/s)
ω_{10} ($= 2\pi \times 3{\cdot}65 \times 10^6$ rad/s $- 2\pi \times 3{\cdot}7 \times 10^6$ rad/s)

different modes were observed. From a study of these characteristics the following features may be noted.

Case A:

Characteristics as shown in Fig. 5(a).

(*a*) Oscillations are possible only at ω_{10}.

(*b*) The value of M_1 required for maintenance of oscillations increases with increase in the value of M_2.

Case B:

Characteristics as shown in Fig. 5(b).

(*a*) Oscillations are possible at ω_{10}, at ω_{11} or simultaneously at both.

(*b*) Oscillations at ω_{10} are excited when M_1 is much larger than M_2. As M_1 is decreased for a fixed value of M_2, gradually oscillations at ω_{11} develop simultaneously with oscillations at ω_{10}. For further decrease in M_1 only oscillations of ω_{11} become possible.

(*c*) The value of M_1 required for maintenance of oscillations at ω_{10}, as in the previous case, increase with increase in the value of M_2. However, for oscillations at ω_{11} the required value of M_1 decreases with increase in the value of M_2.

Case C:

Characteristics as shown in Fig. 5(c), 5(d), 5(e).

In an actual oscillator the anode and cathode line frequencies are usually adjusted so as to be equal. An attempt was made to study this case. However, due to the coupling through anode to cathode capacitance it was hard to tune experimentally the two resonant systems to identical frequencies. The following procedure was hence adopted. The anode line frequency was first fixed approximately at 8·0 Mc/s. The cathode line frequency was gradually increased by steps and the M_1–M_2 plane curves shown in Fig. 5 were obtained for each setting. Figures 5(c), 5(d) and 5(e) show a set of such curves as cathode line frequency is increased to approach the anode line frequency.

It may be noted that the general features are identical to those listed under Case B for all the adjustments. However, as ω_{11} approaches ω_{12} simultaneous oscillations are more easily excited. The required value of M_1 to maintain oscillations at ω_{10} are somewhat smaller than in Case B for the same value of M_2.

It should be noted that the features listed above which were obtained experimentally all agree with those discussed in connection with theory.

7. Conclusion

It has been shown from an analysis of a lumped equivalent circuit of a synchrocyclotron oscillator that oscillations may be excited at the dee frequency and under certain conditions also at the anode coupling line frequency. The anode line frequency oscillations may occur for grid leak bias arrangement simultaneously with the dee resonant frequency oscillations or may occur alone by suppressing the latter.

It has also been shown that oscillations of this undesired frequency may be completely suppressed by making the anode line frequency lower than the cathode line frequency. However, for obtaining the greatest efficiency for the oscillator it is desirable to make the two resonant frequencies equal. In such circumstances, oscillations at the anode line frequency may be suppressed by introducing cubic type non-linearity instead of the grid leak bias type non-linearity.

Experimental studies made with a model oscillator gives results in agreement with the theory.

8. Acknowledgment

The authors are indebted to Professors J. N. Bhar, B. D. Nag Chaudhury and D. N. Kundu for their kind interest in the work.

9. References

1. D. N. Basu Mallik and B. R. Nag, "Modes of oscillation of a grounded grid cyclotron oscillator", *The Radio and Electronic Engineer*, **27**, pp. 27–36, 1964.
2. N. Kryloff and N. Bogoliuboff, "Introduction to Non-linear Mechanics". (Princeton University Press, 1947.)
3. L. V. Skinner, "Criteria of Stability in Circuits Containing Nonlinear Resistance", Doctoral Dissertation, University of Illinois, 1948.
4. K. R. MacKenzie *et al.* "Design of the radio frequency system for the 184-inch cyclotron", *Rev. Sci. Instrum.*, **20**, pp. 126–133, 1949.
5. K. R. MacKenzie, "The proton deuteron r-f system for the Berkeley synchrocyclotron", *Rev. Sci. Instrum.*, **22**, pp. 302–309, 1951.
6. F. A. Heyn, "The synchrocyclotron at Amsterdam", *Philips Tech. Rev.*, **12**, pp. 241–256, 1951.
7. F. H. Schmidt, "Mechanical frequency modulation system as applied to the cyclotron", *Rev. Sci. Instrum.*, **17**, pp. 301–306, 1946.
8. T. G. Pickavance, J. B. Adams and M. Snowden, "The Harwell cyclotron", *Nature*, **165**, pp. 90–91, 1950.
9. L. Kornblith, "An r.f. generator for nuclear energy studies", *Electronics*, **27**, pp. 142–145, May 1954.
10. S. Kikuchi *et al.*, "A 160-cm synchro and variable energy ordinary cyclotron", *J. Phys. Soc., Japan*, **15**, pp. 41–59, 1960.
11. J. J. Livingood, "Principles of Cyclic Particle Accelerators". (D. Van Nostrand, Princeton, N.J., 1961.)

Manuscript first received by the Institution on 16th November 1964. (Paper No. 1004).

U.D.C. 621.375.9.029.63

A Parametric Amplifier for the Frequency Range 400–800 Mc/s

By

J. D. PEARSON, M.Sc.†

A paper to be presented at the Conference on U.H.F. Television in London on 22nd–23rd November 1965.

Summary: The paper considers the performance required from a parametric amplifier. Choice of varactor diode and pump frequency and the necessity to keep circuit losses to a minimum are discussed. A practical amplifier is described in detail including frequency tuning, variation of gain with temperature and power saturation. The expected noise figure was 1 dB and this was confirmed in practice. A method of increasing bandwidth by cascading two amplifiers is given.

1. Introduction

The paper describes the design and performance of a relatively simple parametric amplifier for the frequency range 400–800 Mc/s. At the start of the design study it was thought that a u.h.f. parametric amplifier would have applications in radio astronomy, radar and master receivers for wired television. Such an amplifier must therefore satisfy the following requirements.

(1) Have a noise figure sufficiently low that it could be regarded as approaching the ideal receiver. The maximum noise figure of the parametric amplifier was to be 1 dB, 0·25 dB of this total would arise in the circulator, so that the amplifier itself must contribute only 0·75 dB, i.e. it has to approach the noise figure obtainable with the more complicated maser amplifier.

(2) Have a stable gain of at least 20 dB in order that a simple second stage might be used and its noise contribution would not dominate the overall noise figure.

(3) Have a bandwidth of at least 1%.

(4) The amplifier should be simple and hence relatively cheap.

(5) Since the parametric amplifier is a relatively new device, and its first applications might be to improve the performance of existing system it was decided it must be fail safe, i.e. in the event of fault on the parametric amplifier the user would be left with his original noise figure. It was decided therefore that the amplifier would be of the negative resistance type and use a circulator. The previous generation of u.h.f. parametric amplifiers had been of the up-converter type since at the start of their development u.h.f. circulators were not available. About three years ago such circulators were becoming commercially obtainable and it was decided therefore to go ahead and build conventional amplifiers for the u.h.f. region.

† Ferranti Ltd., Wythenshawe, Manchester 22.

2. Amplifier Design

In building a parametric amplifier, it is necessary to provide circuits incorporating the varactor diode, at the signal, idler and pump frequencies. The type of varactor diode and the pump frequency to be used must first be chosen. The higher the cut-off frequency of the diode selected, the lower will be the noise figure possible from its use in an amplifier and for a given diode there exists an optimum pump frequency to obtain the mimimum noise figure. It is possible to calculate the expected noise figure which may be obtained with an amplifier by the use of diodes of various cut-off frequencies and with various pump frequencies. Diodes of 100 Gc/s cut-off (−6 V) are readily obtainable and when used with an X-band klystron as the pump source, noise figures of less than 1 dB are predicted. This is sufficiently low for all our applications and the use of a higher cut-off frequency varactor together with a higher pump frequency is not justified, since they would not appreciably add to the performance but would increase the amplifier cost and possibly reduce the reliability.

The approximate expression for the noise figure of a parametric amplifier at high gains is

$$F = \left[1 + \frac{r}{R_g}\right]\left[1 + \frac{f_1}{f_2}\right] \qquad \text{.....(1)}$$

where f_1 is the signal frequency, f_2 is the idler frequency, r is the resistance of the unloaded signal circuit, which in a carefully designed circuit can be taken as the series resistance of the varactor, and R_g is the resistance of the source when transformed to the signal circuit. This expression is given in terms of a series equivalent circuit, most authors use a shunt

equivalent circuit (see for example Greene and Sard,[1] eqn. 10), but since the losses in the varactor arise in the base resistance which is in series with the junction capacitance, a series circuit appears more logical. The ratio r/R_g is the standing wave ratio (<1) between the circulator and the input of the unpumped amplifier and it may be shown

$$\frac{Q_0}{Q_L} = 1 + \frac{R_g}{r} \qquad \text{.....(2)}$$

where Q_0 = unloaded Q of the signal circuit

and Q_L = loaded Q of the signal circuit

Figure 1 is a graph of the theoretical noise figure against R_g/r for a 400 Mc/s amplifier pumped at 8800 Mc/s. The higher the value of R_g/r, the lower is the noise figure of the amplifier, however, R_g/r cannot be made indefinitely high otherwise the obtainable gain is restricted. A varactor diode has a certain resistance associated with it. When used in an amplifier it is capable of producing a negative resistance which, in general, is greatly in excess of its positive resistance. Thus the amplifier may be loaded by the source resistance by an amount such that the total positive resistance is equal to the available negative resistance. Under this condition gains up to infinity (oscillation) may be obtained and r/R_g is at its limiting value in the expression for noise figure. The limiting value of the loading is a function of the cut-off frequency of the diode and the type of junction (abrupt or diffused). The maximum loading is given by Kurokawa and Uenohara[2]

$$1 + \frac{R_g}{r} = \left[\frac{\gamma}{2}\right]^2 Q_{d_1} Q_{d_2} \qquad \text{.....(3)}$$

where Q_{d_1}, Q_{d_2} are the diode Q's at the signal and idler frequencies

$$Q_{d_1} = \frac{1}{\omega_1 C_j r} \qquad \text{.....(4)}$$

ω_1 is the signal angular frequency (radians/second) C_j is the junction capacitance at the operating voltage. For silicon graded junctions operating at zero volts $\gamma = 0{\cdot}5$ and eqn. (3) may be rewritten;

$$1 + \frac{R_g}{r} = \frac{1}{16} \frac{f_c}{f_1} \cdot \frac{f_c}{f_2} \qquad \text{.....(5)}$$

where f_1, f_2 are the signal and idler frequencies respectively, and f_c is the varactor cut-off frequency at the working voltage. This is thought to be a conservative estimate giving loadings less than the theoretical figures of Penfield and Rafuse.[3] Using a diode of cut-off frequency 100 Gc/s at a bias of -6 V, eqn. (5) gives a maximum loading given by $R_g/r = 36$ for a 400-Mc/s amplifier operating at zero volts.

It has been assumed in eqn. (1) and in Fig. 1 that the only source of noise is Johnson noise arising in the series resistance of the varactor; however, if any direct current flows some shot noise will exist.[4]

The effect on the overall noise figure of shot noise is usually very small but since in this particular

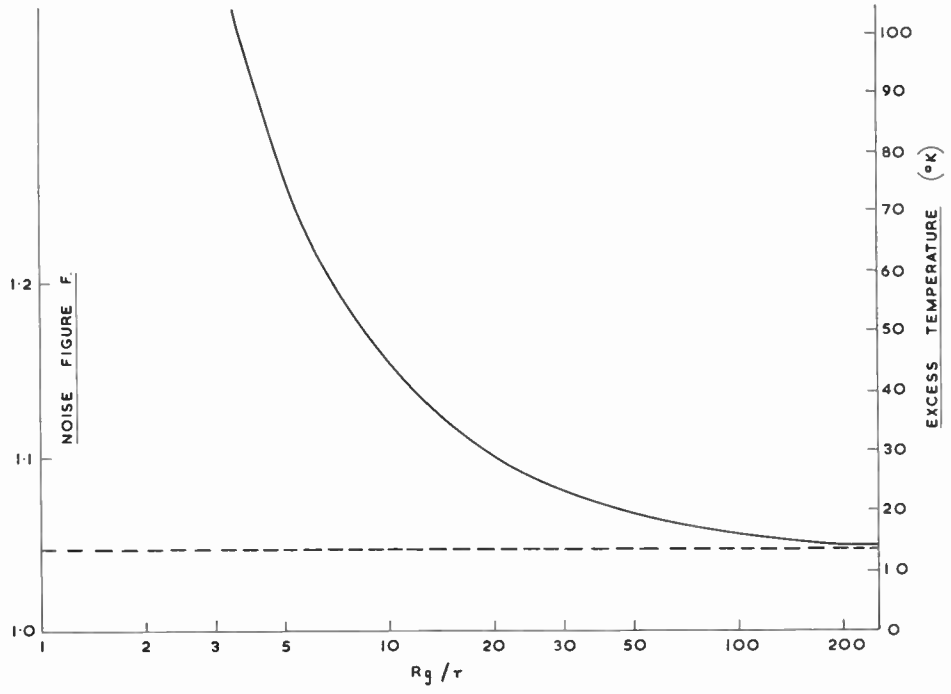

Fig. 1. Theoretical noise figure vs. R_g/r for 400 Mc/s amplifier pumped at 8800 Mc/s.

design the Johnson noise is also expected to be very small, an additional safety factor was introduced. To minimize direct current flow the varactor was pumped to approximately half its theoretical limit and amplifiers were designed to have

$$R_g/r = 20$$

This increased the theoretical noise figure of expression (1) by only 0·10 dB over the figure for $R_g/r = 36$, and should reduce the required pump power and have less detuning of the circuits when the amplifier is pumped. This last point will be discussed later.

3. Circuit Design

Figure 2 is a diagram of a parametric amplifier. A problem for the designer is the effective separation of the three frequencies involved in the amplifier, the signal, the idler and the pump. Since the signal frequency is well below cut-off of the pump waveguide no leakage of signal occurs along this path. To prevent pump and idler power passing to the main coaxial signal cavity a radial bandstop filter is placed near the diode.

The signal circuit consists of a coaxial line with the varactor diode acting as a capacitor at its end. The equation to determine the resonant frequency is

$$\cot(2\pi/\lambda)l = \omega C_0 Z_0 \qquad \text{.....(6)}$$

where $\omega = (2\pi/\lambda)/c$ = angular frequency (rad/s)

$c = 3 \times 10^{10}$ cm per second

l = cavity length

C_0 = total capacitance of the diode

Z_0 = characteristic impedance of the coaxial line forming the cavity.

The dimensions of the signal cavity are chosen such that:

(i) The losses in the cavity are mainly due to the series resistance of the diode, that is the radial dimensions are chosen sufficiently large that the losses in the cavity wall can be neglected.

(ii) The stored energy in the coaxial cavity is mainly magnetic. In order to get the maximum bandwidth, the electrical stored energy associated with the diode capacitance must be balanced by magnetic energy in an inductance, and no additional electrical energy should be added. The method of obtaining resonance which has been chosen, using a coaxial line to supply the inductance, must also add electrical stored energy, this may be kept small by using a line of high characteristic impedance and thus, from eqn. (6), a relatively short length of line.

The expression for the Q of coaxial cavity loaded by a diode of capacitance C_j and series resistance r is given by

$$\frac{1}{Q} = \frac{1}{Q_0} + \frac{\alpha}{Q_d} \qquad \text{.....(7)}$$

where Q is the Q of the system,

Q_d is the diode Q $(1/\omega C_j r)$,

Q_0 is the Q of a resonant half-wave-length cavity made of coaxial line of the same radial dimensions as that used.

Losses in the cavity end wall have been neglected.

It can be shown that

$$\alpha = \frac{2\sin 2kl}{\sin 2kl + 2kl} \qquad \text{.....(8)}$$

$$\frac{1}{Q_0} = \frac{1}{4\pi^2}\frac{R_s\lambda}{Z_0}\left[\frac{1}{b} + \frac{1}{a}\right] \qquad \text{.....(9)}$$

R_s = surface resistance (ohms per square)

λ = signal wavelength

a = radius of the inner conductor of the cavity

b = radius of the outer conductor of the cavity

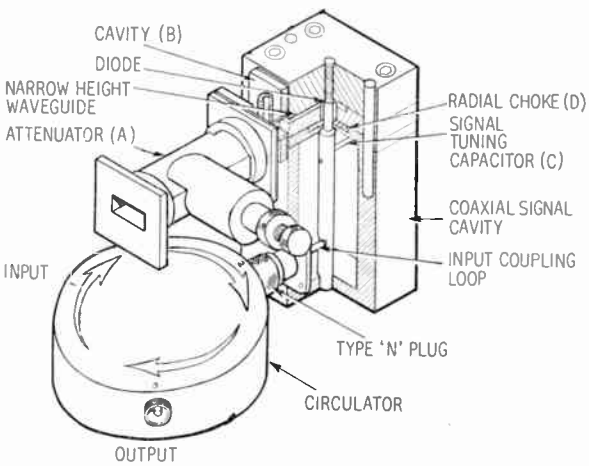

Fig. 2. Construction of the parametric amplifier.

The terms on the right-hand side of eqn. (7) are proportional respectively to the losses in the cavity walls and the losses in the varactor. Thus in order to satisfy condition (i) above.

$$\frac{1}{Q_0} \ll \frac{\alpha}{Q_d}$$

and to satisfy condition (ii)

$$\alpha \gg 0 \qquad [\alpha_{max} = 1]$$

These inequalities imply that

Z_0 should be high

a, b should be large

R_s should be low

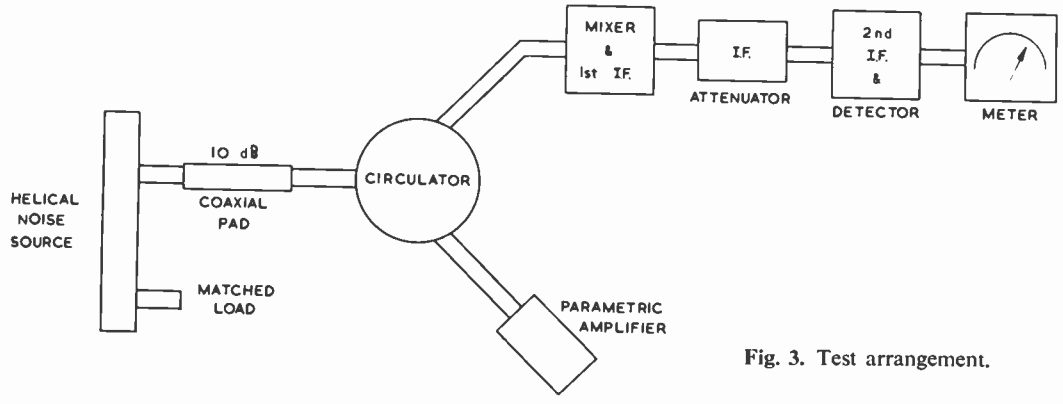

Fig. 3. Test arrangement.

In the amplifier Z_0 is made 100 ohms, the internal diameter of the coaxial cavity is 1·5 in (b = 0·75 in), the outer wall of the cavity is made of aluminium and the inner conductor of silver plated brass. The total capacity of the varactor at zero volts is 1·4 pF.

The input to the signal cavity is through an N-plug, and a rigid connection is made to the centre conductor of the cavity, a magnetic coupling loop being formed consisting of the extension of the N-plug centre conductor, the inner conductor of the cavity and the cavity bottom. The position of the N-plug is such that a coupling of approximately 20 : 1 is obtained.

In order to compensate for variations in varactor impedance a variable capacitor (C) is included in the signal circuit. This can also be used to obtain a mechanically tunable parametric amplifier.

The radial choke (D) prevents the idler and pump power getting into the signal cavity. If a satisfactory choke is not used any variation in the signal circuit, e.g., changes in the tuner C, changes in aerial mismatch etc., will have an effect on the pump and idler circuits, in particular the pump power to the varactor may be changed and variations in gain will occur.

The radial choke is chosen to be resonant at a frequency mid-way between the idler and pump frequencies and presents a high impedance at its open end. The position of the choke is approximately a quarter wavelength from the waveguide wall and thus at the idler and pump frequencies there is an effective short from the diode to the waveguide wall.

The pump power to the varactor is controlled by the waveguide attenuator A, the cavity B is tuned to the pump frequency and thus presents a short circuit to the idler frequency approximately at its front face. The waveguide beyond the diode is terminated in a short circuit. The distance of the cavity B and the short circuit from the varactor are chosen to give resonances at the idler and pump frequencies. In practice it is found that the position of the short circuit determines the pump resonance and the cavity position the idler resonance, and nearly independent tuning of idler and pump frequencies can be obtained by variation of these dimensions.

When a varactor is pumped the change in capacitance in the forward voltage direction is greater than the decrease in the reverse direction; thus the mean value of capacitance increases from the unpumped condition. The resonant frequencies of the signal and idler decrease on pumping and in designing the amplifier this must be taken into account. A detuning of approximately 20 Mc/s occurs in the signal circuit on pumping.

4. Performance

4.1. *Noise Figures*

The noise figure of a system having a parametric amplifier as the first stage will have contributions from

(a) the loss in the circulator,

(b) the parametric amplifier itself,

(c) the second stage and subsequent stages.

It may be shown that the overall noise figure is given by

$$F = \frac{1}{L_1}\left[F_1 + \frac{F_2 - 1}{G_1 L_2}\right] \qquad \text{.....(10)}$$

where F_1 = parametric amplifier noise figure

L_1 = loss in the circulator ports 1 to 2

L_2 = loss in the circulator ports 2 to 3

G_1 = gain of the parametric amplifier

F_2 = noise figure of the system without the circulator and parametric amplifier.

The circulator loss is approximately 0·25 dB, i.e. $L_1 = L_2 = 0{\cdot}944$.

From eqn. (1) with a loading of 20 : 1 and an idler-to-signal-frequency ratio of 20 the theoretical amplifier noise figure is

$$F_1 = 1{\cdot}1$$

Taking $F_2 = 10$ and $G_1 = 100$ (a noise figure of 10 dB and a parametric amplifier gain of 20 dB) and substituting in expression (1):

$$F = 1{\cdot}059\,[1{\cdot}1 + 0{\cdot}095]$$
$$= 1{\cdot}165 + 0{\cdot}101$$
$$= 1{\cdot}266\ (1{\cdot}02\ \text{dB})$$

or expressed in terms of excess noise temperatures, the parametric amplifier contributes 48 deg K and the second stage 29 deg K giving a total system excess of 77 deg K. The values for F_2 and G_1 are chosen to be the same as those used in evaluating the amplifiers in the laboratory.

The test set-up for measuring noise figures is shown in Fig. 3; the noise source is a helical mount using an argon noise tube and the coaxial attenuator is 10 dB $\pm 0{\cdot}1$ dB. The use of a coaxial pad between the noise source and the parametric amplifier is to prevent any possible change in gain of amplifier on firing the tube. The impedance looking into the noise source may be slightly different for the tube fired and unfired which can cause changes in parametric amplifier gains and thus invalidate the noise figure measurements. The use of the 10 dB pad makes this effect negligible. Care is taken to ensure correct readings of the i.f. attenuator by having good matches looking into the first and second i.f. strips from the attenuator and having a minimum insertion of 20 dB in the attenuator.

The so-called Y method is used to measure the noise figure. With the parametric amplifier at 20 dB gain and the noise tube off, the i.f. gain is adjusted to give a reading on the meter, the noise tube is then switched on and by increasing the attenuation in the i.f. strip the meter is brought back to the original reading. The change in i.f. attenuation (power ratio) is noted (Y). The expression for the excess noise temperature of the system is

$$T = \frac{\alpha T_e - T_0[Y + \alpha - 1]}{Y - 1} \qquad \text{.....(11)}$$

where α = attenuation in front of noise tube = 0·1 (power ratio)

T_e = noise temperature of the gas tube

T_0 = room temperature assumed as 290°K.

For the tube used the excess noise is 15·55 dB at X-band when $T_e = 10{,}408$°K. (No figures are quoted for lower frequencies.)

Some correction is necessary for the imperfect coupling of the discharge to the helix below 500 Mc/s. At 400 Mc/s for example the attenuation through the mount with the tube on is 12 dB which reduces the noise from the mount to 0·936 of its value for perfect coupling. Assuming a noise temperature of 10,408°K for the tube at 400 Mc/s, in the mount the effective temperature will be 9,742°K. The average measure value of Y for a 400 Mc/s amplifier is 5·5 dB ($Y = 3{\cdot}548$) giving an excess temperature of 81 deg K. This is very good agreement with the predicted figure (77 deg K). Agreement between theoretical and experimental values of noise figure have been obtained with u.h.f. amplifiers in the range 400–700 Mc/s.

4.2. *Gain-Bandwidth Characteristics*

The (gain)$^{\frac{1}{2}}$-bandwidth product of an amplifier is a constant which is determined by the unpumped bandwidths of the signal and idler circuits:[1]

$$G^{\frac{1}{2}}B \propto \left[\frac{1}{B_1} + \frac{1}{B_2}\right]^{-1} \qquad \text{.....(12)}$$

where G = power gain

B = amplifier bandwidth

B_1 and B_2 are the bandwidths of the signal and idler circuits unpumped.

At 20 dB gain 5 Mc/s bandwidth is obtained at 400 Mc/s, 8 Mc/s at 600 Mc/s. The use of very high quality diodes reduces the bandwidth since the idler circuit Q is increased and B_2 becomes the dominant term in expression (12). A typical response curve is given in Fig. 4 and is in good agreement with the theoretical shape.

$$\text{Gain at } f_0.(1 \pm \delta) = G_0 \frac{1}{1 + \left[\frac{\delta}{\delta_0}\right]^2} \qquad \text{.....(13)}$$

where G_0 is the gain at mid-band

δ_0 is the 3-dB bandwidth

4.3. *Tuning*

The amplifier may be tuned over 30 Mc/s by adjustment of the capacitor C leaving the pump frequency fixed. Slight adjustments only are needed in the attenuator setting to keep the gain constant over this range. By changing the pump frequency tuning over 50 Mc/s is possible but re-adjustments of the pump attenuator A and pump cavity B are necessary in this case.

4.4. *Temperature*

The effect of ambient temperature has been investigated only over the restricted range 17°C–45°C. The junction capacitance of the varactor is temperature dependent and thus the impedance presented to the pump and the pump voltage across the junction changes with temperature causing changes in gain. The isolation of some circulators has been found to be temperature dependent, and the power output of the pump klystron may also change with temperature. The variation in gain for the complete amplifier at 20 dB gain over the range 17–45°C is between 1·5 dB and 5 dB, and is less than 2 dB for an amplifier at 15 dB gain.

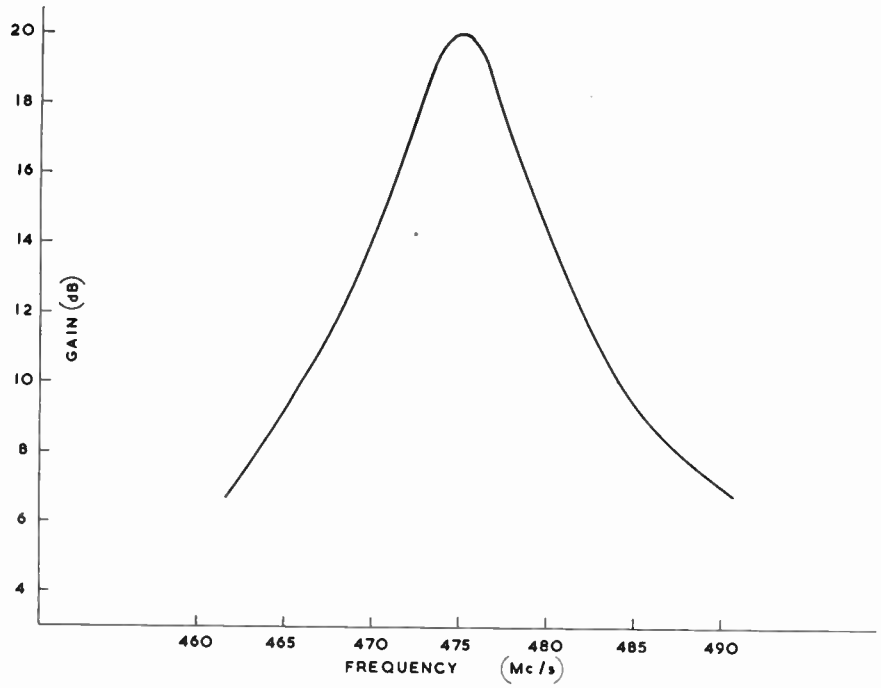

Fig. 4. Frequency response of the amplifier.

4.5. *Saturation*

Figure 5 shows the input/output characteristic for an amplifier at 20 dB low signal gain operating with no bias. By operating the varactor at −1 V bias the input levels can be increased by approximately 10 dB over the no-bias condition before the same gain compression occurs.

5. Cascaded Amplifiers

For some applications a 1% bandwidth is not sufficient, in which case the amplifier can be run at lower gains with a corresponding increase in second stage noise contribution or two amplifiers can be cascaded.

It was shown above that the gain-frequency response

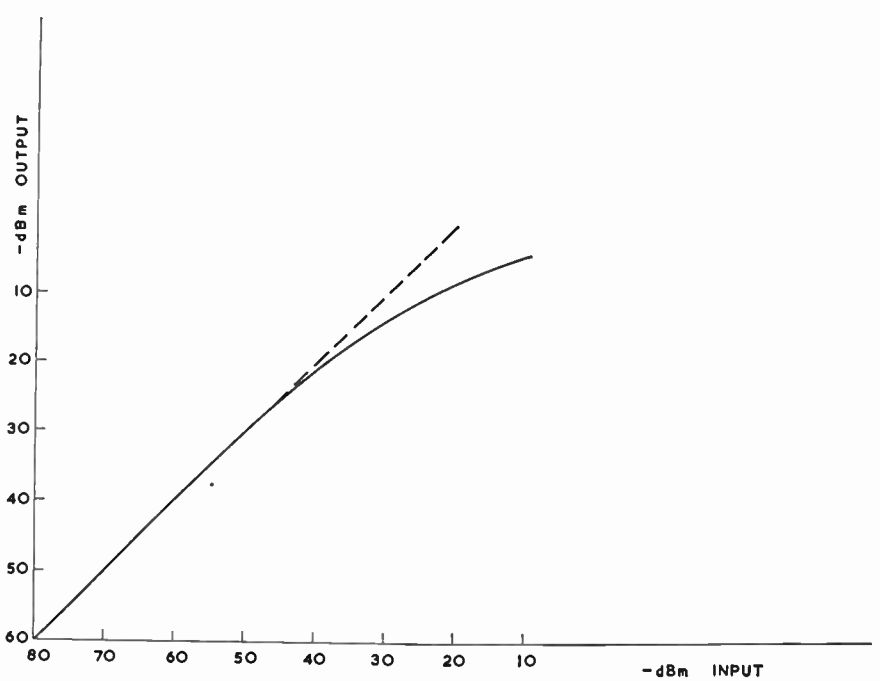

Fig. 5. Input/output characteristics for the amplifier.

of the v.h.f. parametric amplifier is in good agreement with the theoretical shape (eqn. 13)). This is of the same form as that of a single stage of an i.f. amplifier.[5] Hence all the methods of stagger tuning which are well known for i.f. amplifiers apply directly to stagger tuning parametric amplifiers. These may be summarized as follows.

1. To obtain a maximally flat response two amplifiers must be staggered by an amount equal to the bandwidth of a single amplifier.
2. To obtain a response with a 3-dB ripple the amplifiers must be staggered by an amount equal to 2·4 times the bandwidth of a single amplifier.

In the second case to obtain 20 dB overall gain each amplifier should have a gain of 16·8 dB and the overall bandwidth of the system will be five times that of a single amplifier at 20 dB. The use of two amplifiers in cascade increases the noise figure of the system in particular at the band edge where the gain of the first amplifier is low. Consider a four-port circulator with parametric amplifiers of noise figures F_1 and gains G_1 and G_2 at the frequency to be considered. The loss between port 1 and 2 is denoted by L_1 and between 2 and 3 by L_2. In general

$$L_2 \simeq 2L_1$$

The noise figure of this system is given by

$$F = \frac{1}{L_1}\left[F_1 + \frac{F_1 - 1}{L_2 G_1} + \frac{1 - L_2}{L_2 G_1}\right]$$

The second and third terms represent the deterioration in noise figure using the two-amplifier system over a single amplifier. At the band edge $G_1 = 1{\cdot}8$ and for a typical circulator $L_1 = 0{\cdot}944$ (0·25 dB) $L_2 = 0{\cdot}891$ (0·5 dB).

Taking $F_1 = 1{\cdot}1$, the ratio of the parametric amplifier plus circulator noise figure in the cascaded system at one edge of the band to that of a single stage is 1·117, an increase of 0·5 dB in overall noise figure.

6. References

1. J. C. Greene and E. W. Sard, "Optimum noise and gain-bandwidth performance for a practical one-port parametric amplifier", *Proc. Inst. Radio Engrs*, **48**, pp. 1583–90, September 1960.
2. K. Kurokawa and M. Uenohara, "Minimum noise figure of the variable-capacitance amplifier", *Bell Syst. Tech. J.*, **40**, pp. 695–722, May 1961.
3. P. Penfield and R. P. Rafuse, "Varactor Applications". (The M.I.T. Press, Cambridge, Mass., 1962).
4. H. Heffner and G. Wade, "Gain, bandwidth and noise characteristics of the variable parametric amplifier", *J. Appl. Phys.* **29**, pp. 1323–31, September 1958.
5. G. E. Valley and H. Wallman, "Vacuum Tube Amplifiers". (McGraw-Hill, New York, 1948).

Manuscript first received by the Institution on 23rd March 1965 and in final form on 9th August 1965. (Paper No. 1005).

STANDARD FREQUENCY TRANSMISSIONS

(Communication from the National Physical Laboratory)

Deviations, in parts in 10^{10}, from nominal frequency for **September 1965**

September 1965	GBR 16 kc/s 24-hour mean centred on 0300 U.T.	MSF 60 kc/s 1430–1530 U.T.	Droitwich 200 kc/s 1000–1100 U.T.	September 1965	GBR 16 kc/s 24-hour mean centred on 0300 U.T.	MSF 60 kc/s 1430–1530 U.T.	Droitwich 200 kc/s 1000–1100 U.T.
1	— 150·2	— 151·1	+ 1	16	— 151·0	— 151·1	+ 1
2	— 151·1	— 151·1	+ 1	17	— 150·4	— 150·4	+ 1
3	— 149·9	— 149·3	+ 2	18	— 150·4	— 150·1	+ 1
4	— 148·2	— 148·2	+ 2	19	— 150·2	— 150·3	+ 1
5	— 149 9	— 150·5	+ 2	20	— 149 8	— 150·3	+ 1
6	— 150·3	—	+ 1	21	— 150·3	— 150·7	+ 1
7	— 149·9	— 150·8	+ 2	22	— 150·5	— 150·7	+ 1
8	—	— 147·0	0	23	— 150·4	— 151·3	0
9	— 149·9	— 152·0	+ 1	24	— 150·5	— 150·7	— 1
10	— 150·7	— 150·1	0	25	— 150·5	— 150 6	— 1
11	— 149·5	— 150·7	+ 2	26	— 150·8	—	— 2
12	—	—	—	27	— 150·5	— 151·2	— 3
13	—	— 149·2	+ 2	28	— 150·9	— 150 5	— 3
14	— 149·2	— 150·9	+ 1	29	— 150·7	— 150·6	— 2
15	— 150·6	— 152·5	+ 1	30	— 150·6	— 150·9	— 6

Nominal frequency corresponds to a value of 9 192 631 770 c/s for the caesium F,m (4,0)–F,m (3,0) transition at zero field.
Note: The phase of the GBR and MSF time signals was retarded by 100 milliseconds at 0000 U.T. on 1st September 1965.

I.E.C. information

Conference on Electrical Equipment of Machine Tools

Thirty-five delegates from eleven countries (Belgium, Czechoslovakia, France, Germany, Holland, Italy, Japan, Switzerland, U.K., U.S.A., U.S.S.R.) attended a recent meeting in Coventry of I.E.C./TC 44 —the technical committee on the electrical equipment of machine tools of the International Electrotechnical Commission.

The meeting approved for publication the final draft of an international Recommendation covering standardized requirements for the use of electrical equipment of machine tools. A supplementary draft, for electrical equipment of machines used in large series production (transfer machines), is at present in circulation to the 39 member countries for approval.

After considerable discussion, a further supplementary draft for electronic equipment on machine tools was amended, and it was agreed to circulate this to all member countries for approval. The purpose of these recommendations on electronic equipment is to ensure safety to personnel, uninterrupted production, long life for the equipment, and economy in maintenance costs. The recommendations cover the following main points:

provision for use in various working conditions, including use in temperate or tropical climates and in the special conditions of machine shops;

their use on various electrical supply systems, with precautions specially necessary for electronic equipment;

marking and operating instructions and diagrams to facilitate installation, maintenance and repairs;

the use of internationally standardized components wherever practicable;

special precautions to be taken on electronic equipment against electric shock, faulty operation or damage to machines or work pieces during operation and maintenance;

methods of assembly and wiring to secure accessibility, mechanical strength and correct electrical and electronic functioning;

testing requirements, both initially and for locating faults in service.

It was agreed that a Guide to the specification of operating requirements for electronic equipment on machine tools, proposed by the British Committee, should be circulated to all National Committees for comment. The Guide states the kinds of information required—and why they are required—by manufacturers of electronic equipment in order that they may provide reliable and economic equipment for machine tools.

Also discussed at the I.E.C. meeting was the standardization of colours for pushbuttons and pilot lamps according to their function; agreed lists of such standards are to be circulated to National Committees for approval.

The Committee reviewed the co-ordination of their own work with that of other international standardizing committees, particularly on the subject of fully automated machine tools using numerical (tape) control for positioning and sequencing.

To continue work on the standardization of diagrams and cable connections for machine tool use, small working groups have been set up, and these will take into account the contributions made to the Coventry discussions by delegates from different countries. Close contact will be maintained with National Committees on the work of these groups, in preparation for the next full international meeting to be called by the Swiss secretariat when sufficient documentation has accumulated.

Judging by the comments of delegates to the Coventry meeting, the conference should help the prospects for the export of British machine tools, a large number of which were seen in manufacture and use by delegates during technical visits to works in Coventry.

Annual Report for 1964

The Central Office Report of the International Electrotechnical Commision recently published, describes fully the various activities of the I.E.C. and reports in detail on the progress of its work during 1964.

In addition to an introductory section, the report covers the following main aspects: work of the Council and Committee of Action; meetings held in 1964; work of the Technical Committees (and sub-committees); co-operation with I.S.O. (International Organization for Standardization); I.E.C. publications issued during 1964 and those being printed at the end of the year; and draft publications submitted for approval.

The report is of great importance for everyone interested in I.E.C. work, whether at the level of the national standards bodies or in those industrial sectors dealing with electrical and electronic engineering. Copies may be obtained from the B.S.I. Sales Branch, 2 Park Street, London, W.1. The price is 30s. (postage will be charged extra to non-subscribers).

U.D.C. 621.391.812.62.029.63

Simultaneous Long Distance Tropospheric Propagation Measurements at 560 Mc/s and 774 Mc/s over the North Sea

by

J. W. STARK, C.G.I.A.
(*Associate Member*)†

A paper to be presented at the Joint Conference on U.H.F. Television in London on 22nd–23rd November 1965.

Summary: Simultaneous field strength measurements on u.h.f. transmissions at 560 Mc/s and 774 Mc/s were carried out over the North Sea, on transmission paths ranging from 123 miles (198 km) to 591 miles (950 km). The results show that with the same meteorological conditions the long-term received field strengths tend to be higher, although not to a significant extent, for the 774-Mc/s transmission than for the 560-Mc/s transmission.

When meteorological conditions are favourable during anticyclonic weather, the signals received are, at times, very much in excess of the free-space value. These high signals are associated with horizontally stratified boundary layers at heights up to 500 metres resulting from subsidence in the lower atmosphere. Boundary layers at greater heights are thought to be partly responsible for the signals received at the greater distances during abnormal propagation conditions.

The field strength exceeded in each month for certain time-percentages, the types of signal received and the fading rate are also discussed.

1. Introduction

The sharing of v.h.f. and u.h.f. television channels by the United Kingdom and Continental countries is the inevitable consequence of the limited frequency spectrum allocated to broadcasting. Information was required on oversea propagation so that the distance separation between stations could be planned to limit the probability of mutual interference during periods of abnormal propagation.

During the past decade the B.B.C., with the co-operation of the Netherlands Postal and Telecommunications Services, have completed a series of long distance propagation measurements over the North Sea in the Broadcasting Bands II, III and IV. The results of these measurements were used in conjunction with data from other administrations to derive the C.C.I.R. (Geneva 1963)[1] oversea field-strength/distance curves. As a continuation of the oversea tests, Band V measurements at 774 Mc/s were commenced in the latter part of 1961.

At no time in the past had the oversea experiments been made simultaneously at two frequencies, and while a comparison of the final curves of the previous tests in each of the bands gives some indication of the effect of frequency in long distance propagation over the sea, part of the differences which appear between them may be attributed to the different meteorological conditions that prevailed during each test period. It was decided, therefore, that during part of the 774-Mc/s experiment, measurements would be made simultaneously on a frequency of 560 Mc/s. The measurements commenced on 13th October 1961 and terminated on 30th June 1962.

The transmitting station was at Scheveningen in Holland and five B.B.C. receiving stations were situated on the east coast of the United Kingdom at distances ranging from 123 miles (198 km) to 591 miles (950 km).

2. Transmitting and Receiving Sites

2.1. *Transmitting Site*

B.B.C. Research Department transmitters utilizing frequencies of 560 Mc/s and 774 Mc/s were installed and operated by the Netherlands Postal and Telecommunications Services at Scheveningen Radio Station. Each transmission was square-wave modulated at 1000 c/s to a depth of 100%. The modulation was cut off for two seconds every minute for identification purposes at the receiving sites.

The 560-Mc/s transmitting aerial was a two-stack five-element Yagi with a reflector screen. Its intrinsic gain relative to a $\lambda/2$ dipole was 13 dB, and its half-power beamwidth $\pm$ 23 deg. The 774-Mc/s aerial was a corner reflector with an intrinsic gain of 13·5 dB, the half-power beamwidth being $\pm$ 24 deg. Each aerial was horizontally polarized and was

† British Broadcasting Corporation, London, W.1.

Table 1

Transmitting site details

Location	Frequency	E.R.P. in direction of maximum radiation	Direction of maximum radiation	Site height above mean sea level		Latitude	Longitude
	Mc/s	kW	True bearing	ft	m		
Scheveningen	560	1·95	320°	43	13·1	52° 06′ N	04° 16′ E
Scheveningen	774	0·95	320°	43	13·1	52° 06′ N	04° 16′ E

mounted on a separate mast at a height of 155 feet (47 metres) above ground level. For all transmission paths the radio horizon was the sea. Further transmitting site details are given in Table 1.

The daily schedule of transmission was 0830–2300 hours, British local time.

2.2. *Receiving Sites*

The receiving sites were at Happisburgh (Norfolk), Flamborough Head (Yorkshire), Newton-by-the-Sea (Northumberland), Bridge of Don (Aberdeen) and Lerwick (Shetland Islands). Figure 1 shows the geographical distribution of the sites and Table 2 gives additional receiving site details.

The main features of the u.h.f. receiver were its high sensitivity and stability of calibration. The recording law was approximately logarithmic with a signal range of about 50 dB, but it was found that this range was insufficient during abnormal propagation conditions. Accordingly, a 30-dB attenuator, which came into circuit at high levels of signal, was introduced between the signal- and intermediate-frequency units. This was operated by a 1-milliampere relay in series with the recording milliammeter, whose full scale deflection was also 1 milliampere. Thus, when the meter deflection approached its maximum, the relay operated and attenuated the signal output, bringing the metering current within recording range. The circuit remained in this condition for about three hours, and the attenuator was then switched out. If the signal had in the meantime dropped in level, recording continued normally; if, however, the signal level was still high, the attenuator was again brought into circuit.

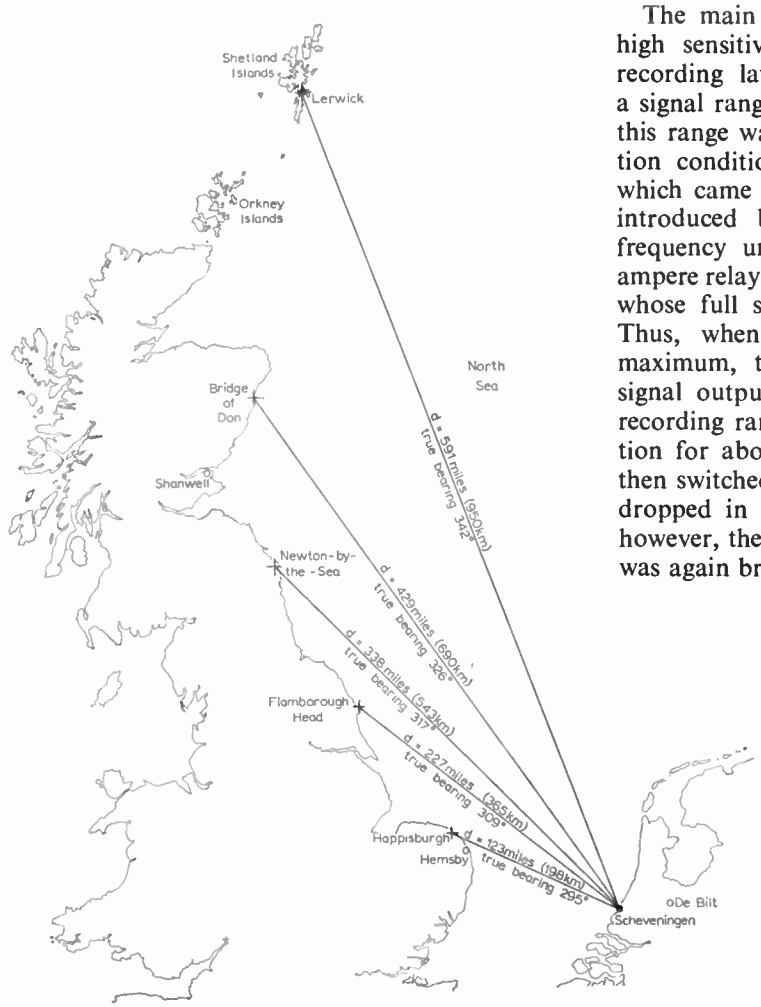

Fig. 1. Geographical distribution of sites.
- ● Transmitting site
- \+ Receiving sites
- ○ Weather stations

Table 2
Receiving site details

Location	Distance from transmitter		Site height above mean sea level		Aerial height above ground level				True bearing of site from transmitter	Latitude	Longitude
					560 Mc/s		774 Mc/s				
	ml	km	ft	m	ft	m	ft	m			
Happisburgh	123	198	50	15·2	32	9·8	28	8·5	295°	52° 49′ 42″ N	01° 31′ 38″ E
Flamborough Head	227	365	150	45·7	32	9·8	28	8·5	309°	54° 07′ 39″ N	00° 05′ 40″ W
Newton-by-the-Sea	338	543	70	21·3	32	9·8	28	8·5	317°	55° 31′ 06″ N	01° 37′ 05″ W
Bridge of Don	429	690	30	9·1	32	9·8	28	8·5	326°	57° 10′ 40″ N	02° 05′ 00″ W
Lerwick	591	950	300	91·5	32	9·8	28	8·5	342°	60° 08′ 00″ N	01° 10′ 20″ W

The 560-Mc/s and 774-Mc/s receiving aerials were of the Yagi two-stack ten-element type and each had an intrinsic gain in the region of 12 dB, relative to a $\lambda/2$ dipole and a half-power beamwidth of approximately $\pm$ 18 deg.

At the most distant sites, the receiver sensitivity, the aerial and its associated feeder were checked by a sweep-frequency calibration oscillator at the close of each day's recording. The oscillator signal, radiating from a test dipole situated in the vicinity of the receiving aerial, swept through a frequency band of several megacycles centred on the frequency to which the receiver was tuned. The recorder trace is thus a check on the overall pass-band and the sensitivity of the receiver. The 560-Mc/s and 774-Mc/s systems had separate oscillators and test dipoles. At the nearer sites where no automatic checks had been installed the receiving system parameters were checked during routine visits.

The recorder charts were run at a speed of 3 in (7·6 cm) and 6 in (15·2 cm) per hour depending upon the type of fading normally received at the site.

3. Results

3.1. *Analysis*

The field strength recording charts were analysed on a daily basis, grouped into months and finally the months' results were assembled to give the overall data for each transmission path.

The records of the measurements were analysed to determine the length of time during which signal levels exceeded various values of field strength at each of the receiving sites. These time durations, expressed as percentages of the overall valid recording time, were then plotted against field strength in decibels relative to 1 μV/m (dB(μV/m)) for an e.r.p. of 1 kW. The field strength exceeded for 0·1%, 1%, 10% and 50% of the overall time was plotted against each of the distances at which the recordings were made. A family of curves was then constructed to show the variation of field strength against distance.

3.2. *Variation of Field Strength with Time*

Figures 2(A) and 2(B) give the results of the measurements made at each of the east coast sites and are plotted as field strength exceeded against percentage of total time for the 560-Mc/s and 774-Mc/s transmissions. The Newton-by-the-Sea 560-Mc/s curve has been extrapolated to the 0·01% time value as no record of field strength above 47 dB was attained owing to a receiving equipment fault. The accompanying table for these curves gives the total hours recorded at each site and the appropriate free-space field strength for each path.

Table 3, derived from Fig. 2, gives the field strengths exceeded for 0·1%, 1%, 10% and 50% of the total time. It will be observed that a few of the values listed in Table 3 have been obtained by extrapolation. These extrapolations were carried out to give further points for comparison.

The field strength ratios of the signals received at the two frequencies at each site are listed in Table 4. It is seen there that all but one of the ratios for the 0·1%, 1% and 10% values show the 774-Mc/s signal to be higher. For 50% of the time at Happisburgh and Flamborough Head, however, the 774-Mc/s signal was the lower by a small amount. These ratios are consistent with assumptions that the 50% field strengths are predominantly due to scattering in turbulent conditions whereas the modes of propagation for the smaller time-percentages are refraction or specular reflection.

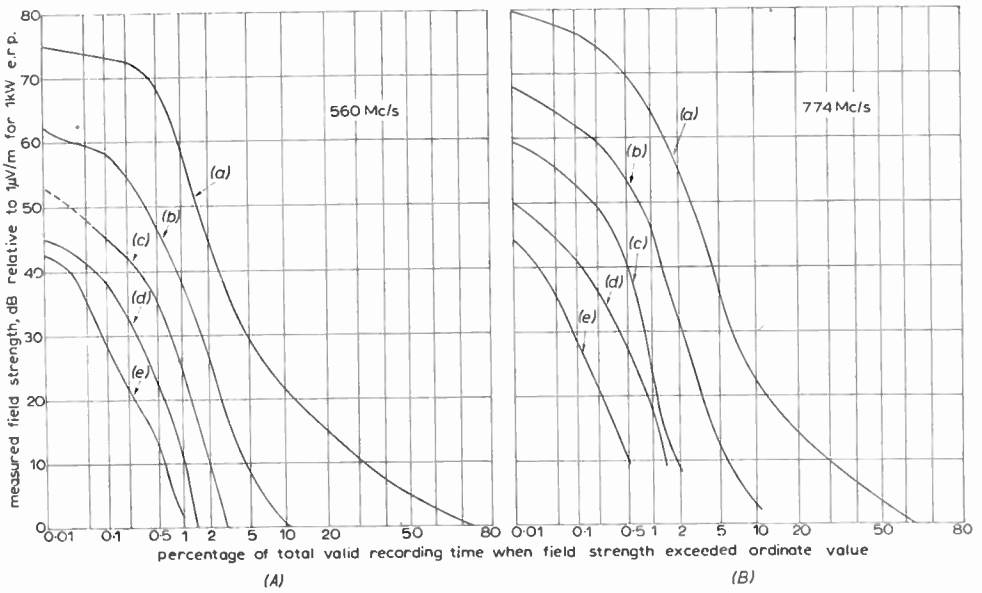

Curve	Receiving site	Distance		Total hours recorded		Free space field for 1 kW e.r.p. dB
		miles	km	560 Mc/s	774 Mc/s	
(a)	Happisburgh	123	198	3513	3683	61·0
(b)	Flamborough Head	227	365	3708	3685	55·6
(c)	Newton-by-the-Sea	338	543	3637	3472	52·2
(d)	Bridge of Don	429	690	3685	3688	50·2
(e)	Lerwick	591	950	3630	3714	47·3

Fig. 2. Variation of field strength with time.

Table 3

Scheveningen results—560 Mc/s and 774 Mc/s

Curve	Receiving site	Distance	Field strength, dB(μV/m) for 1 kW E.R.P.							
			560 Mc/s				774 Mc/s			
		km	0·1%	1%	10%	50%	0·1%	1%	10%	50%
(a)	Happisburgh	198	73·0	59·0	21·5	5·0	76·5	64·0	22·5	3·5
(b)	Flamborough Head	365	58·5	38·5	0·5	−17·0†	62·0	46·0	3·0	−18·0†
(c)	Newton-by-the-Sea	543	45·0	24·5	−18·0†	NL	52·5	24·0	−16·0†	NL
(d)	Bridge of Don	690	38·0	11·5	NL	NL	41·0	18·0	NL	NL
(e)	Lerwick	950	28·5	2·0	NL	NL	28·5	2·0†	NL	NL

† Extrapolated value. NL—below noise level.

Table 4

Ratio of 774-Mc/s to 560-Mc/s field strengths at each receiving site

Receiving site	Distance	Ratio in dB of 774-Mc/s to 560-Mc/s field strengths			
	km	0·1%	1%	10%	50%
Happisburgh	198	3·5	5·0	1·0	−1·5
Flamborough Head	365	3·5	7·5	2·5	−1·0
Newton-by-the-Sea	543	7·5	−0·5	2·0	—
Bridge of Don	690	3·0	6·5	—	—
Lerwick	950	0	0	—	—

Table 5 gives the range of fading† between the 0·1% and 1%, 1% and 10% and 10% and 50% of the overall time for the signals at the two frequencies at each of the receiving sites. This table reveals that there is a trend for the range of fading between time-percentages to increase with distance. Another interesting feature is that the range of fading between the 1% and the 10% values is very much greater than for the 0·1% and 1%, and the 10% and 50% values. This shows that in a temperate climate such as is experienced in the United Kingdom, the transition to the abnormal type of propagation over long periods of time occurs between the 1% and 10% field strength values.

3.3. *Field Strength/Distance Curves*

The field strengths listed in Table 3 are used to derive, by the method of least squares, the best-fit curves for the 0·1%, 1%, 10% and 50% time values. Separate best-fit lines are calculated for the 560-Mc/s, 774-Mc/s and the combined 560-Mc/s and 774-Mc/s measurements using an inverse power-law relationship. They are shown in Fig. 3. Field strength, E, is assumed to vary with distance, d, in the form $E = k/d^m$ where k is a parameter related to the transmission path and the transmitter power, and m is the slope of the best-fit line.

The 0·1% and 1% best-fit lines for the separate 560-Mc/s and 774-Mc/s measurements show that there is a difference at the two frequencies of about

† i.e. the difference in dB between the field strength exceeded for the smaller time-percentage and that exceeded for the larger time-percentage.

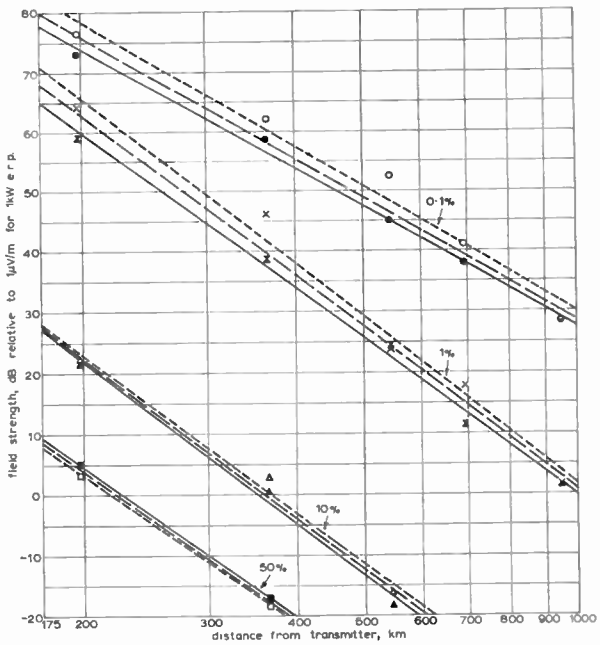

Fig. 3. Variation of field strength with distance.

- – – – – 774 Mc/s
- — — — Combined 560 Mc/s and 774 Mc/s
- ——— 560 Mc/s
- ● 0·1% 560 Mc/s ○ 0·1% 774 Mc/s
- ▼ 1·0% 560 Mc/s × 1·0% 774 Mc/s
- ▲ 10% 560 Mc/s △ 10% 774 Mc/s
- ■ 50% 560 Mc/s □ 50% 774 Mc/s

Table 5

Range of fading between various time-percentages

Receiving site	Distance	Range of fading in dB between various time-percentages					
		0·1–1·0%		1·0–10%		10–50%	
	km	560 Mc/s	774 Mc/s	560 Mc/s	774 Mc/s	560 Mc/s	774 Mc/s
Happisburgh	198	14·0	12·5	37·5	41·5	21·0	19·0
Flamborough Head	365	20·0	16·0	38·0	43·0	17·5	21·0
Newton-by-the-Sea	543	20·5	28·5	42·5	40·0	—	—
Bridge of Don	690	26·5	23·0	—	—	—	—
Lerwick	950	26·5	26·5	—	—	—	—

5 dB at 200 km, reducing to 2 dB at 1000 km, the 774-Mc/s line being the higher of the two. In the case of the 10% and 50% lines, the difference is approximately 1 to 2 dB for distances up to at least 600 km, both pairs of lines being nearly parallel; but whereas the 774-Mc/s line is higher than the 560-Mc/s for the 10% time, it is the lower for the 50% time curves. It should be borne in mind, however, that two of the four 50% field strength plots were extrapolated. The separate best-fit lines for each time-percentage show that, under the same meteorological conditions, there is little difference between the propagation of a signal in Band IV and one in Band V. For all practical purposes, therefore, the results of the simultaneous 560-Mc/s and 774-Mc/s transmissions are combined to give the appropriate best-fit lines, as shown in Fig. 3. The field strength/distance curves of Fig. 3 are given for the sake of completeness, but the main object of the work described in this paper is to compare propagation on the two frequencies involved, rather than to measure the absolute value of field strength as measurements were made over a period of only 9 months.

3.4. *Monthly Field Strength Variations*

The Happisburgh and Flamborough Head 560-Mc/s and 774-Mc/s field strengths exceeded in each month for selected time-percentages are shown in Fig. 4. The Flamborough Head 50% plots are not measurable because the signal is below the noise level of the receiver. There is not enough information to produce similar graphs for Newton-by-the-Sea, Bridge of Don and Lerwick, as signals at these sites are below the noise level of the receivers for the majority of the time.

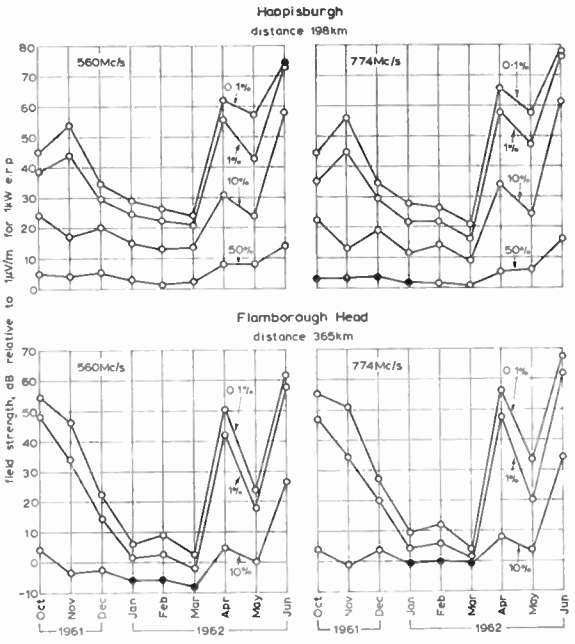

Fig. 4. Field strength exceeded in each month for selected time-percentages.

○ Measured value ● Extrapolated value

Table 6

Standard deviation of field strength exceeded in each month for different time-percentages

Receiving site	Path distance	Standard deviation in dB of field strengths exceeded in each month for different time-percentages							
		560 Mc/s				774 Mc/s			
	km	0·1%	1%	10%	50%	0·1%	1%	10%	50%
Happisburgh	198	17·8	17·2	14·1	3·8	19·9	19·6	16·3	4·7
Flamborough Head	365	22·8	22·1	10·5	—	23·4	21·7	11·2	—

Table 7

Range of monthly field strengths October 1961–June 1962

Receiving site	Path distance	Range of monthly field strengths in dB for stated time-percentages							
		560 Mc/s				774 Mc/s			
	km	0·1%	1%	10%	50%	0·1%	1%	10%	50%
Happisburgh	198	50·5	52·0	45·0	12·5	57·5	60·0	52·5	15·5
Flamborough Head	365	59·0	59·5	34·5	—	63·5	60·0	35·0	—

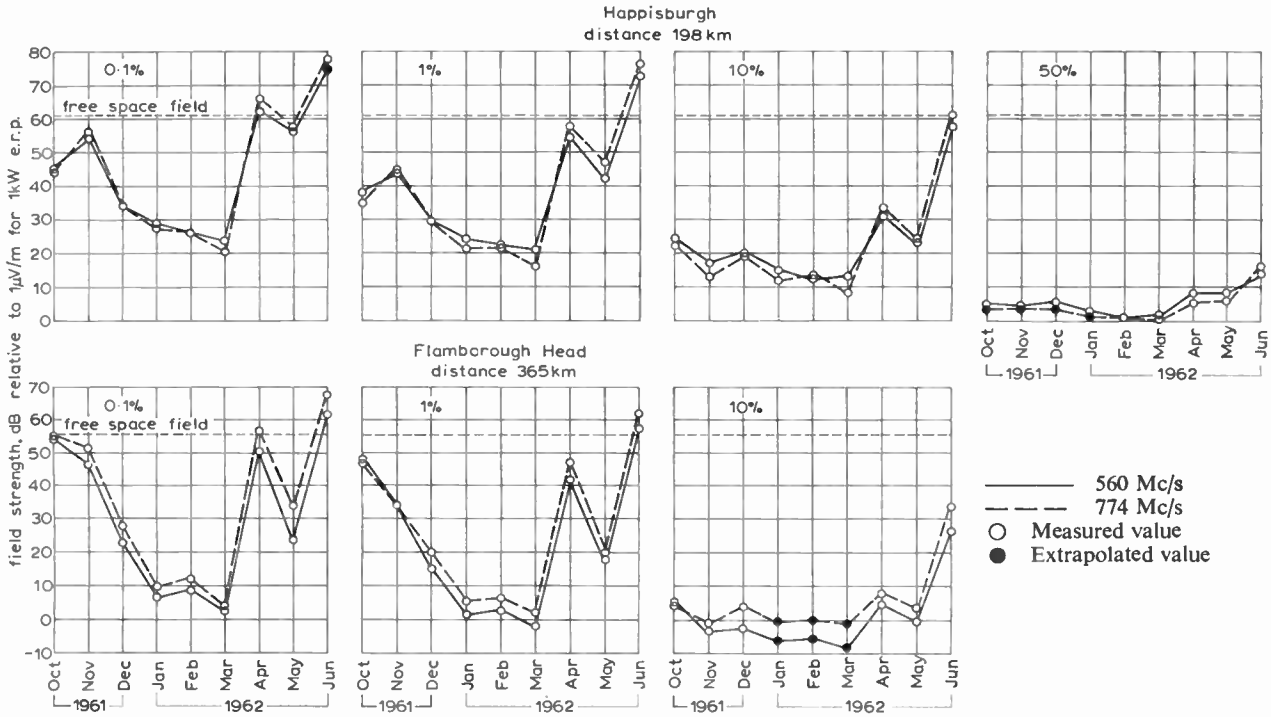

Fig. 5. Comparison of 560-Mc/s and 774-Mc/s field strengths exceeded in each month.

Figure 4 shows that for Happisburgh and Flamborough Head, the month-to-month variations in the field strengths exceeded at the different time-percentages increase with decreasing time-percentage. This also appears in Table 6 where the standard deviations of the monthly figures are given. Table 6 also shows that, for the majority of cases, the 774-Mc/s standard deviation is greater than the 560-Mc/s standard deviation. A comparison of the figures for the two sites indicates that the 0·1% and 1% standard deviations increase with distance at both frequencies, whereas the 10% values decrease. Information of a similar nature is given in Table 7 where the range of field strength exceeded in each month for each time-percentage is given for the nine-month period. The exceptionally high variations of field strength from one month to another for the 0·1%, 1% and 10% values emphasize the necessity for data on long distance tropospheric propagation to be obtained over extended periods of time.

The variations of the 560-Mc/s and 774-Mc/s monthly field strengths received over the same transmission path are seen in Fig. 4 to follow the same pattern. On comparing different paths, however, the pattern may be dissimilar. The Happisburgh and Flamborough Head 0·1% and 1% plots for October and November 1961 show this effect. The Happisburgh 560-Mc/s and 774-Mc/s values are higher in November than in October, whereas at Flamborough Head the October signals are higher. This is due to the position of the high pressure system relative to the transmission path. During October, when signals were abnormal, the centre of the high pressure system was situated over the North Sea, east of Flamborough Head, and then it moved towards South Denmark, presumably affecting the Flamborough Head path to a greater extent. In November, the high pressure systems were centred either over Central Europe or the Baltic region, extending over the North Sea and having a greater influence on the Happisburgh path. On the other hand, the 10% monthly field strength values at both sites follow the same trend, because for these values the signals approach normal propagation conditions. There are occasions, however, when the 10% value is influenced by a prolonged period of abnormal propagation and such a period occurred during the month of June 1962.

The graphs of Fig. 4 are reproduced in Fig. 5 in order to make a clearer comparison of the monthly field strength variations for the two transmissions at the same receiving site. Generally the Happisburgh 774-Mc/s field strengths exceed the 560-Mc/s value only during the months when abnormal propagation is prevalent. The Flamborough Head results, however, show that with two exceptions the 774-Mc/s field strengths are higher than the 560-Mc/s values during both abnormal and normal propagation conditions.

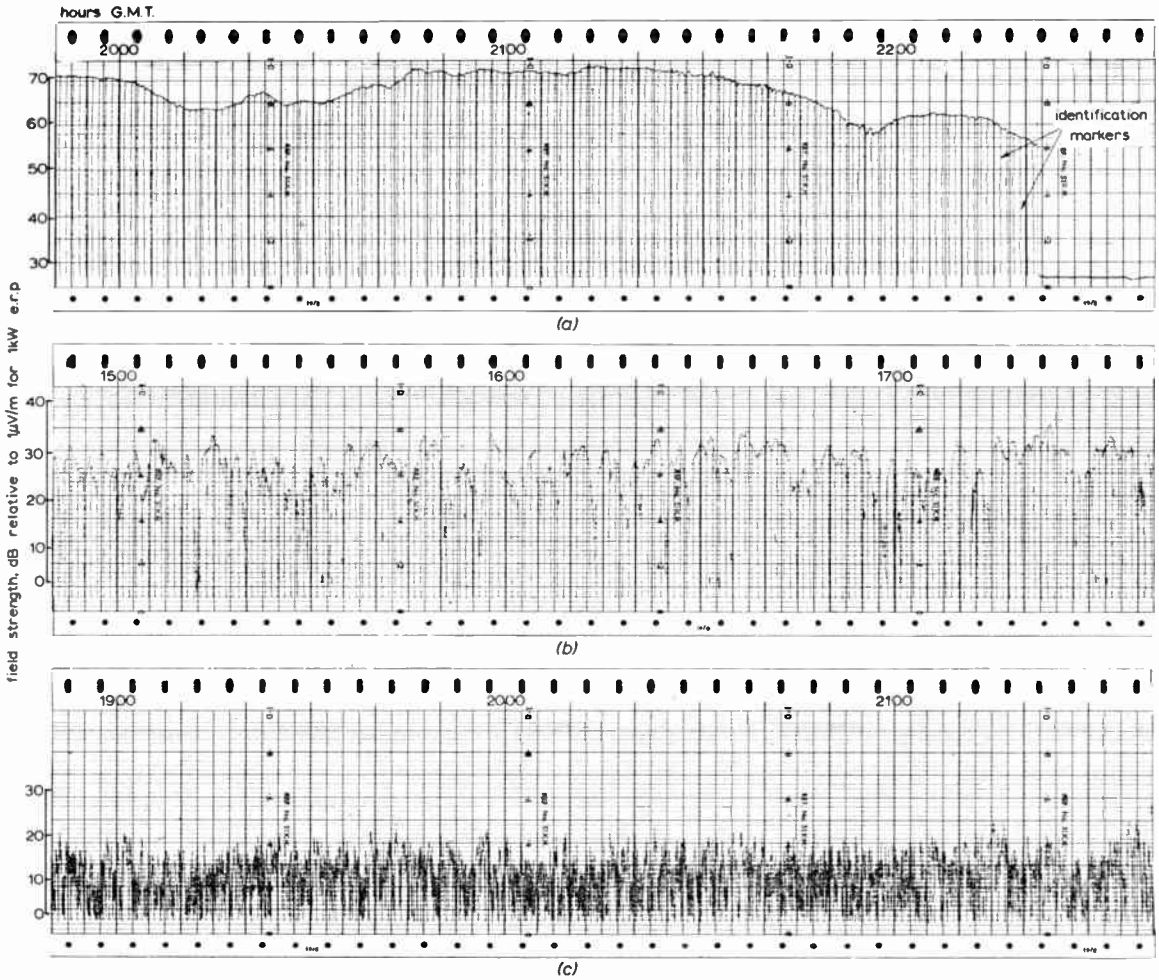

Fig. 6. Types of signals received at Happisburgh.

(a) Type I signal—8th June 1962. (b) Type II signal—23rd April 1962. (c) Type III signal—18th March 1962.

3.5. *Types of Signals and Fading Rate*

Signals received over long distances may be classified into three main groups, as follows:

Type I. Signals which are affected by comparatively little fading.

Type II. Signals which are affected by fading over periods of minutes.

Type III. Signals which are affected by rapid fading.

Figure 6 shows selected samples of Happisburgh recorder charts illustrating the types of signals. Types I and II are normally associated with the high-level signals which occur during anticyclonic weather, although there are instances in which Type II is associated with low-level signals. Type III is associated with the low-level signals which are received during cyclonic weather.

An examination of the recorder charts for the period October 1961 to June 1962 revealed that, in general, the type of signal received at each site for both the 560-Mc/s and 774-Mc/s transmissions was similar. It was decided, therefore, that the Happisburgh 560-Mc/s recorder charts would be inspected in order to obtain the proportion of the total time in which the various types of signals were received. The charts for the more distant sites were not inspected, as in most instances the signals were received only during abnormal propagation conditions.

The type of signal and fading rate during the periods 1000 to 1030, 1400 to 1430 and 2100 to 2130 hours local time were noted. Table 8 gives the percentage of the time, for the appropriate half-hourly period, in which each type of signal was received. These half-hourly periods were then grouped to give an overall percentage as listed in the

right-hand column of Table 8. The table reveals that there is very little difference in the percentage values between the 1000 to 1030 hours period and the 1400 to 1430 hours period. The percentages for the 2100 to 2130 hours period, however, show that Types I and II signals have higher values when compared with the other periods. As the Types I and II signals are generally associated with abnormal propagation, this indicates that these signals are more prevalent in the evening.

Table 8

Percentage of the time during which the various types of signals were received at Happisburgh (560 Mc/s)

Type of signal	Period of observation			
	1000–1030 hours	1400–1430 hours	2100–2130 hours	Combined periods
I	0·8%	0·8%	1·6%	1·1%
II	5·0%	5·8%	6·7%	5·9%
III	94·2%	93·4%	91·7%	93·0%

The overall percentages for the various types show that, in general, the fast-fading low-level type of signal occurs for 93% of the time, whereas the slow-fading, high-level type of signal occurs for the remaining period. These figures confirm the statement made in Section 3.2, that the transition to abnormal propagation occurred for the field strength values between 1% and 10% of the total time.

The fading rate is defined in this paper as the number of times the signal crosses the median value in the positive direction per minute, the fading rate being obtained from the previously mentioned three half-hourly periods in each day. Table 9 gives the approximate fading rate for the different types of signal. A more detailed analysis could not be given because of the relatively slow recorder chart speed used for the continuous measurements. Table 9 shows that the fading rate ratios of the three types of signal are approximately 1 : 10 : 100.

Table 9

Fading rate for the various types of signals—Happisburgh (560 Mc/s)

Type of signal	Fading rate
I	0·04
II	0·4
III	4·5

3.6. *Abnormal Propagation*

Figure 4 shows that the highest signals received during this series of measurements were in June 1962, and the results for this month are used to illustrate abnormal propagation. These June values are listed in Table 10, where they are quoted relative to the free-space field strength. Table 10 shows that at Happisburgh, Flamborough Head and Newton-by-the-Sea signals approaching or in excess of the free-space field were received for the 0·1 and 1 time-percentages. At Bridge of Don and Lerwick the signals approach, but do not reach, the free-space field. It is also interesting to note that the Happisburgh 0·1 time-percentage signal for the 560-Mc/s transmission is 13·5 dB above the free-space value, while for the 774-Mc/s transmission it is 17·0 dB. An inspection of the June 1962 Happisburgh recorder charts showed that the peak signals for the 560-Mc/s and 774-Mc/s transmissions are 76 and 81 dB(μV/m), respectively. These signals are exceptionally high for a path length of 198 km being 15 and 20 dB above the free-space value. The peak signals at the other

Table 10

Received field strengths relative to free-space value—June 1962

Receiving site	Free-space field dB (μV/m) for 1 kW E.R.P.	Received field strength, dB relative to free-space value for stated time-percentage							
		560 Mc/s				774 Mc/s			
		0·1%	1%	10%	50%	0·1%	1%	10%	50%
Happisburgh	61·0	13·5	12·0	−3·0	−47·0	17·0	15·5	0·5	−44·5
Flamborough Head	55·6	5·9	1·9	−29·1	—	11·9	6·4	−21·1	—
Newton-by-the-Sea	52·2	4·8	−9·3	−47·2	—	7·8	−0·2	−43·2	—
Bridge of Don	50·2	−3·2	−13·7	—	—	−0·2	−11·2	—	—
Lerwick	47·3	−3·3	−21·3	—	—	−2·8	−19·8	—	—

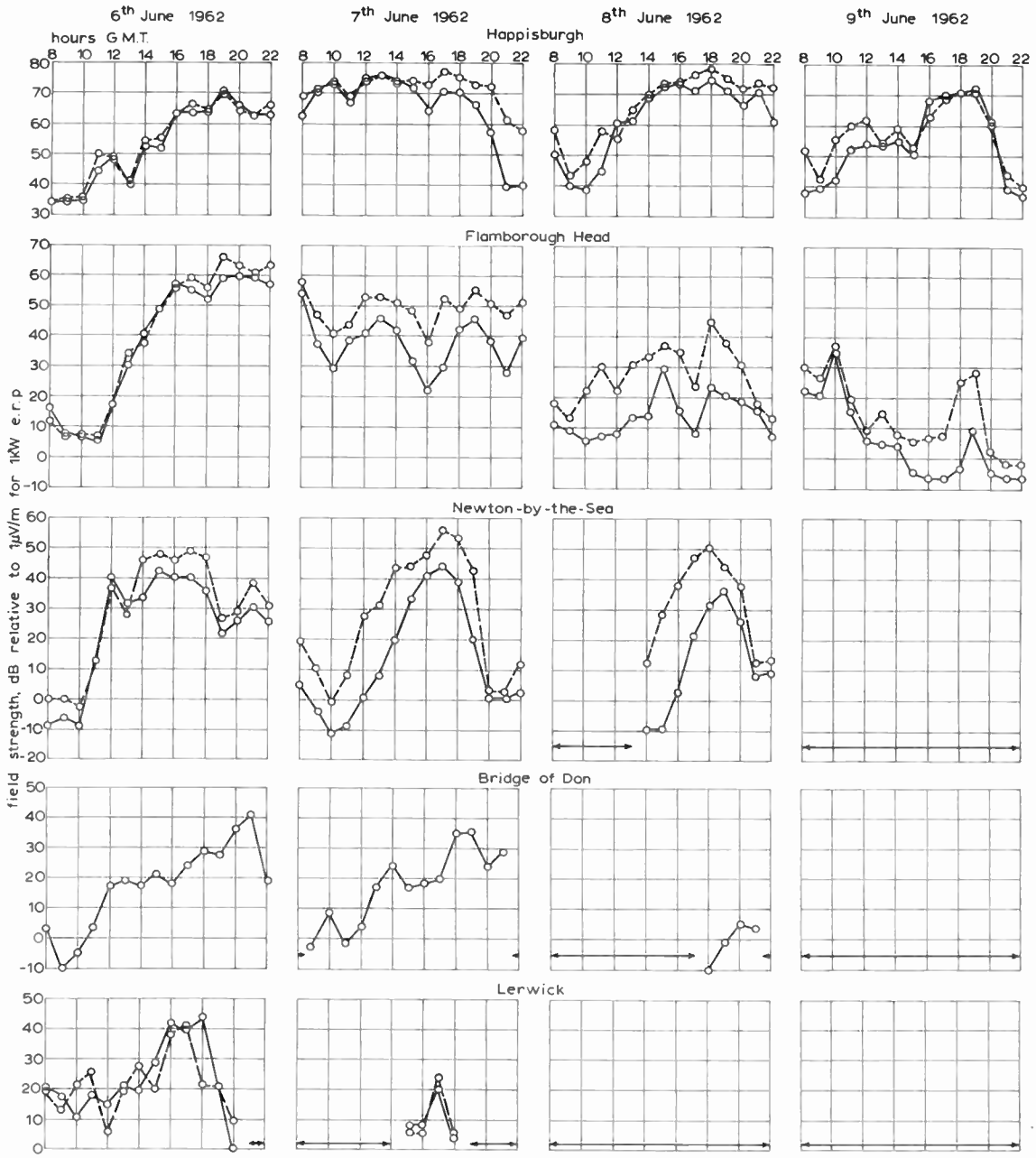

Fig. 7. Variation of hourly median signals 6th to 9th June 1962.

— — — — 774 Mc/s
———— 560 Mc/s
O Measured value ←→ No measurable signal

receiving sites also approach, and sometimes exceed the free-space value, the peak signals being approximately the same or slightly higher than the 0·01% field strength given for each site in Fig. 2.

The abnormally high signals occurred from 6th to 9th June 1962 and the recorder charts for these days were analysed to obtain the variation of hourly median signals. The hourly median signals are plotted in Fig. 7. The 774-Mc/s signals at Bridge of Don could not be accurately obtained during these days because of an intermittent fault on the receiving aerial system.

Figure 7 reveals that during the abnormal conditions prevalent at the time, the 774-Mc/s signal generally exceeded the 560-Mc/s signal. This effect is most noticeable at Flamborough Head and Newton-by-the-Sea. Another interesting feature, notably at Newton-by-the-Sea on 7th and 8th June, is that the diurnal variation of signal reaches its peak at approximately 1800 hours. This effect is discussed in the next sub-section.

It is seen in Fig. 7 that exceptionally high signals were received on consecutive days close to peak television viewing periods, the high levels being maintained for several hours continuously each day. The severity of the interference that will occur between co-channel transmitters in such conditions will be appreciated when it is remembered that the field strengths quoted in Fig. 7 are for an e.r.p. of 1 kW whereas u.h.f. transmissions with an e.r.p. of up to 1000 kW are envisaged.

3.7. *Meteorological Factors*

It is well known that when the weather is anticyclonic, that is, at times of high barometric pressure, u.h.f. signals may be received at distances much greater than normal. The anomalous propagation occurs when meteorological conditions in the lower atmosphere produce a layer of dry, warm air over cooler, moist air. At the boundary between the dry and moist air a negative refractive-index gradient occurs. This gradient, being much greater than normal, causes the radio waves which are usually lost in space to be refracted back to the earth's surface. Should a large change in the refractive-index gradient extend down to the earth's surface, a 'ground based duct' may be formed and within this duct signals are propagated with little attenuation. Similarly, a large negative refractive-index variation with height in the lower atmosphere may act as an 'elevated duct'.

Anomalous propagation tends to be more widespread and continuous on oversea than on overland paths. The main reason is that the sea has no marked diurnal temperature variation and hence the air above it tends to remain cool and moist. The air from higher levels of the atmosphere in a high pressure area subsides and settles as a warm, dry layer over the cool, moist air. The junction of the two masses which is known as a 'subsidence boundary layer' or a 'temperature inversion' gives a sharp negative refractive-index gradient. Similar conditions occur over land, but in these instances, the air in the vicinity of the earth's surface is heated by the sun's rays, and there is not usually such a marked discontinuity in the refractive index as on oversea paths, at least during the day. In addition, the undulations of the terrain tend to break up any tendency to stratification. Another characteristic of oversea propagation is that air from neighbouring land masses may drift over the sea in late afternoon and early evening and accentuate any temperature inversion that already exists. This may partly account for the tendency of the diurnal variation of signal to be at its peak in the late afternoon and evening as shown in Fig. 7. The Newton-by-the-Sea signals on 7th and 8th June are outstanding examples of this effect. On the other hand, the signals on 6th and 7th June at Lerwick were also at a maximum in the late afternoon even though the land mass of the Shetland Islands is not extensive.

3.7.1. Potential refractive index (K)

The refractive index, n, of the troposphere varies with temperature, humidity and pressure. The refractive index is often given in terms of the co-index, N, where

$$N = (n-1)\times 10^6 = \frac{77{\cdot}6}{T}\left(P + \frac{4810e}{T}\right)$$

where T is the absolute temperature (°Kelvin),
P is the atmospheric pressure in millibars,
e is the water vapour pressure in millibars.

There is a better parameter than the co-index, N, for representing pictorially the structure of the atmosphere. The normal changes of N with height tend to obscure phenomena which give rise to abnormal propagation. A parameter which removes altitude dependence from the expression for refractive index is 'potential refractive index'.[2,3] This is denoted by K. The potential refractive index is defined as the value which the normal refractive index of a sample of air would acquire if this sample were taken adiabatically to a pressure of 1000 mb.

In order to derive K, the variation of temperature, humidity and pressure is used in conjunction with a meteorological temperature-entropy chart known as a 'tephigram'.[2] The Daily Aerological Records issued by the Meteorological Office list the temperatures, dew points and pressures from their daily measurements. This information is obtained from the 'radiosonde' ascents which are carried out twice daily at the main weather stations. As the ascents are primarily intended to assist meteorologists in weather forecasting, the fine structure of the atmosphere is generally not measured. To investigate the reception of high signals from Scheveningen the atmospheric region of interest is that over the North Sea. Unfortunately there are no weather ships in the North Sea and consequently there is no alternative but to use the data from the nearest weather station situated on the coastal areas. The records chosen for the investigation are those taken at Lerwick (Shetland Islands),

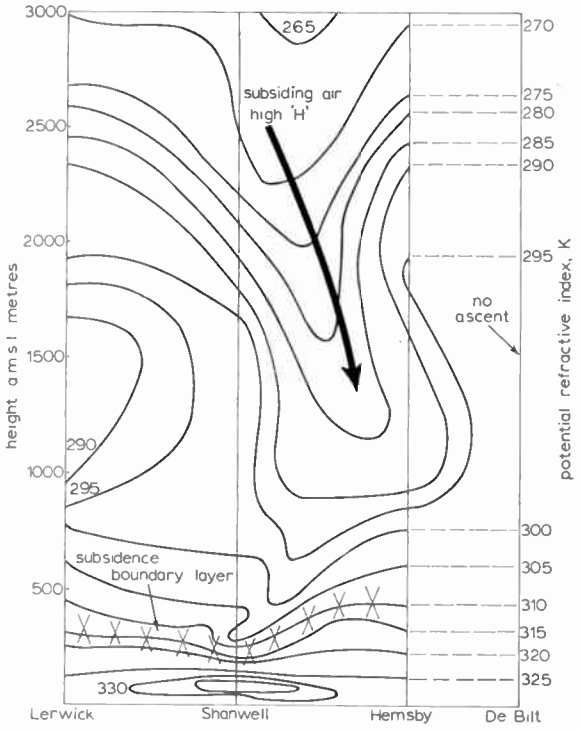

(a) 0001 hours 6th June 1962

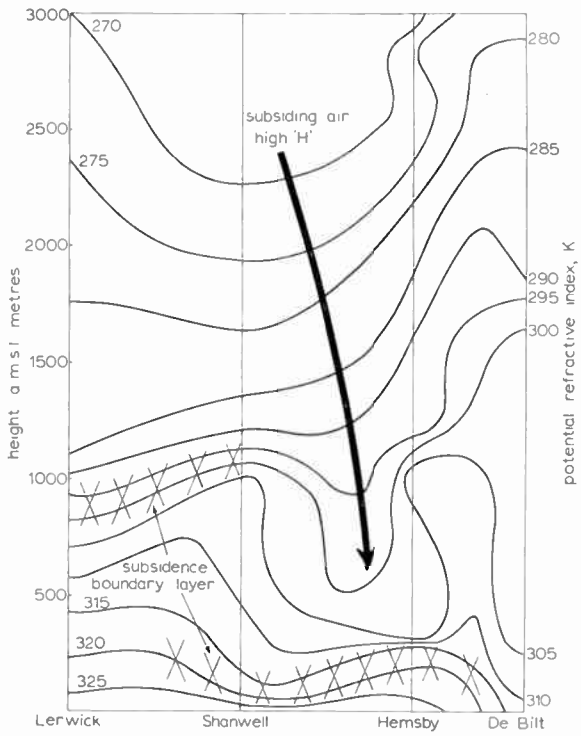

(b) 1200 hours 6th June 1962

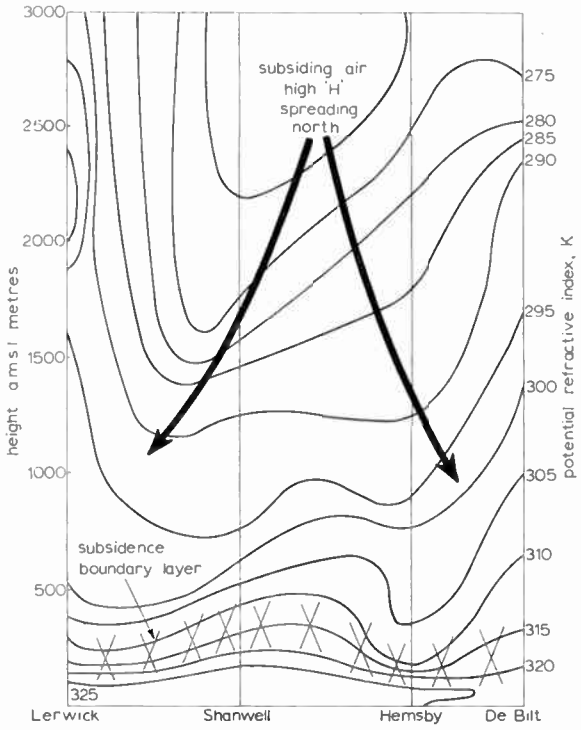

(c) 0001 hours 7th June 1962

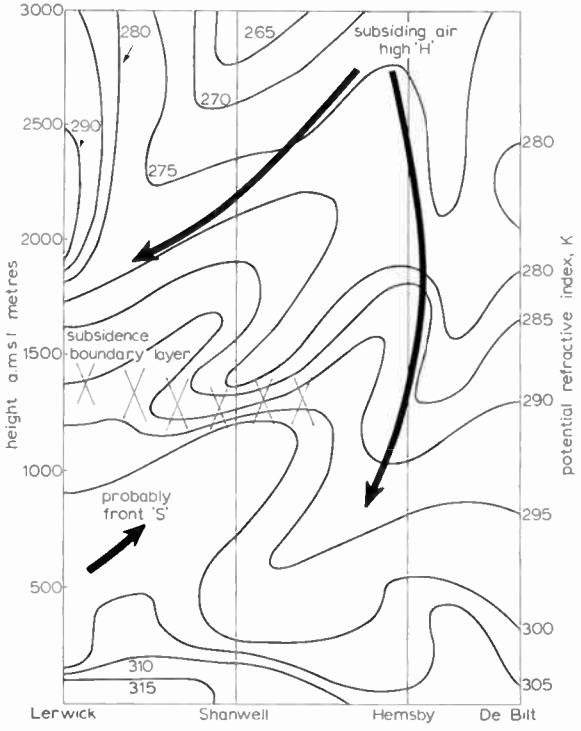

(d) 1200 hours 7th June 1962

Fig. 8. Potential refractive index cross-sections.

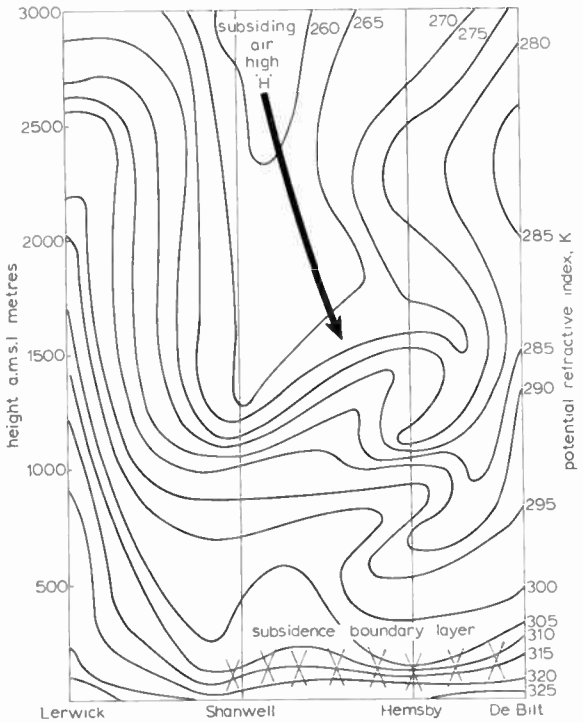

(e) 0001 hours 8th June 1962

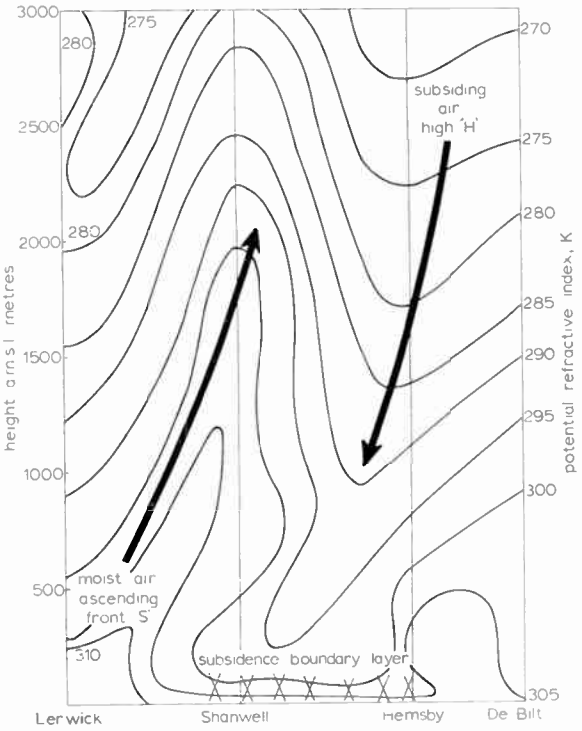

(f) 1200 hours 8th June 1962

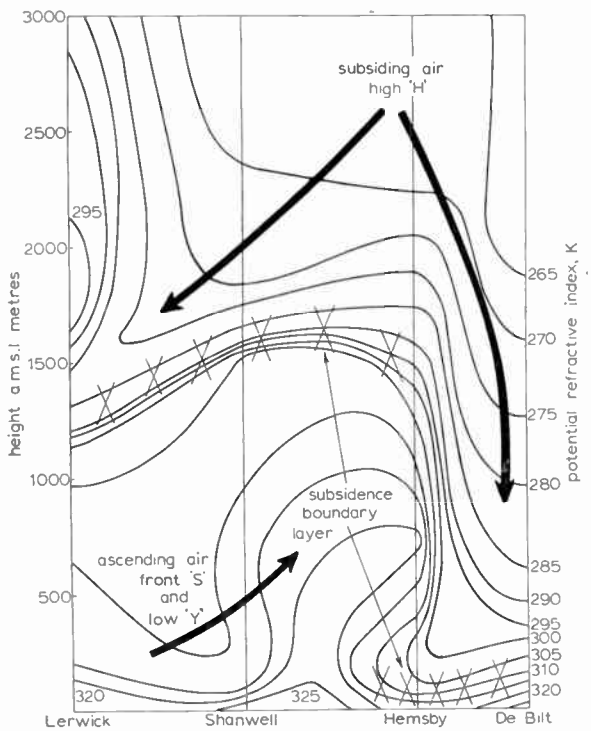

(g) 0001 hours 9th June 1962

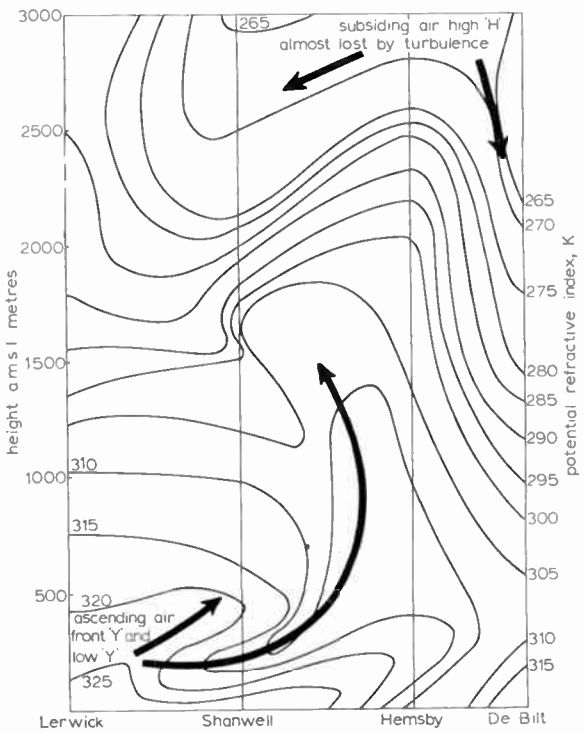

(h) 1200 hours 9th June 1962

Fig. 8. Potential refractive index cross-sections.

Shanwell (Fife), and Hemsby (Norfolk) in the United Kingdom, and at De Bilt in the Netherlands. The geographical position of these stations is shown in Fig. 1. It will be observed that they do not all lie on the same straight line.

3.7.2. Examples of effect of meteorological factors on propagation

The period 6th to 9th June 1962 already referred to in Fig. 7 is used to illustrate potential refractive-index cross-sections. These are shown in Fig. 8(a) to (h). The *K* cross-sections are related to the appropriate Daily Weather Map (also issued by the Meteorological Office) by the alphabetical codes used to identify the 'pressure systems' and 'fronts'.

Figure 8(a) shows the *K* cross-section for 0001 hours on 6th June 1962. In this instance only Lerwick, Shanwell and Hemsby records were available as there was no radiosonde ascent at De Bilt. The steep refractive-index gradients occur where the *K* contours are closest to each other, that is, between 200 and 500 metres in this figure. This region marked by crosses is clearly a subsidence boundary. The subsidence boundary layer extends from Lerwick to Hemsby and is more intense at Shanwell.

Figure 8(b) gives the 1200 hour cross-section for the same day. This shows that the subsidence results in two layers, one at heights between 50 and 350 metres and the other between 800 and 1150 metres. The two layers overlap in the region of Shanwell. Signals (as shown in Fig. 7) were received at all the east coast sites at 1200 hours on 6th June, although they were not exceptionally high for the less distant paths.

The *K* cross-section in Fig. 8(c) shows that the boundary layer which previously existed at the 950-metre level has disappeared. The lower boundary layer now extends from Lerwick to De Bilt varying between 100 and 500 metres. This boundary layer is now more intense and no doubt accounts for the exceptionally high signals which were received towards the late evening of 6th June.

An inconsistency occurs at 1200 hours on 7th June as Fig. 8(d) reveals. At this time, very high signals were received at Happisburgh and Flamborough Head, although no well defined subsidence boundary layer is apparent in the region of Hemsby and De Bilt. It would appear therefore that no boundary layer existed over Hemsby and De Bilt, although it may be assumed, with little doubt, that one existed over the North Sea. The layer existing in the region of Lerwick and Shanwell at an approximate height of 1350 metres was probably partially responsible for the signal received at Bridge of Don.

The distribution of the contours at Lerwick in Fig. 8(e) indicates that the air is well mixed, and this probably accounts for the fact that no signals were received at Bridge of Don and Lerwick at 2200 hours on 7th June.

The cross-section of Fig. 8(f) for 1200 hours on 8th June shows that ascending moist air from front 'S' is predominant in the area between Lerwick and Shanwell. There is a weak subsidence layer up to a height of 150 metres between Shanwell and Hemsby but this does not extend over De Bilt. Despite this, reasonably high signals were received at Happisburgh and Flamborough Head at this time.

Figure 8(g) shows the subsiding air from High 'H' once again forming a high elevated layer. The layer height in this instance varied from 1200 to 1700 metres between Lerwick and Hemsby. Between Hemsby and De Bilt a lower layer also extends up to a height of 200 metres. It will be noted (Fig. 7) that at Happisburgh in the late evening of 8th June, signals well above the free-space value were received. Signals were also received at this time at Flamborough Head and Newton-by-the-Sea, although these were not particularly high.

No well-defined inversion layers appear in Fig. 8(h). Despite this, the signals at Happisburgh were high. It may be conjectured, therefore, that a boundary layer existed over the North Sea between Happisburgh and Scheveningen which was not apparent in the radiosonde measurements at Hemsby and De Bilt. It is interesting to note that the Happisburgh signals had increased in level still more by the late afternoon before dropping.

The *K* cross-sections are constructed from measurements taken at only four points on the abscissa, namely Lerwick, Shanwell, Hemsby and De Bilt. All the information appearing in Fig. 8 between these points is interpolation, arrived at both by reference to the positions of the *K* values on the four ordinates, as well as the information published in the weather charts. While a large part of the *K* cross-sections appears to be dependent on interpolation, it must be remembered that it is usual for anticyclonic weather conditions to extend over great distances with little variation, and the cross-sections may therefore be relied on to give a reasonably good picture of the structure of the lower atmosphere at the time for which they are constructed. It may therefore be justifiably concluded from Fig. 8 that when high signals are received, a subsidence boundary layer exists up to heights of 500 metres over the coastal regions. It is assumed that such layers extend over the North Sea at the same heights. The exceptionally high signals received are, on occasions, well above the free-space values, and it is assumed that they occur when ducts are in existence over the North Sea. Subsidence boundary layers also occur at heights ni the

region of 800 to 1700 metres, and it is probable that these layers are partly responsible for the signals received at the greater distances.

4. Conclusions

Simultaneous measurements at 774 Mc/s and 560 Mc/s reveal that, in general, the field strengths over distant sea paths are greater for the higher frequency but the difference is not significant, and may be neglected in the planning of a u.h.f. television service.

The field strengths exceeded in each month varied over a greater range at the lower time-percentages than at the higher time-percentages.

The slow-fading type of signal received at Happisburgh occurred for approximately 7% of the total time and the fast-fading type of signal for 93% of the time. The slow-fading type of signal is normally associated with the higher levels of field strength prevalent during anticyclonic weather, whereas the fast-fading type is associated with low-level field strength values received during cyclonic weather.

Signals approaching or exceeding the free-space value are likely to be received when intense high pressure systems are situated in the region of the transmission paths. The exceptionally high signals may persist for prolonged periods of time and during these periods the diurnal variation of signal tends to reach its peak value in the late afternoon and evening.

The potential refractive-index cross-sections indicate that when high signals are received over a transmission path a horizontally stratified subsidence boundary layer exists at heights up to 500 metres. The received signals on these occasions invariably approach or are above the free-space value. Boundary layers at heights of 800 metres and 1700 metres, in conjunction with the layers at heights up to 500 metres, are thought to be responsible for the below free-space signals received at the more distant sites.

5. Acknowledgments

The British Broadcasting Corporation acknowledges with grateful thanks the facilities most willingly provided by the Netherlands Postal and Telecommunications Services and in particular by the staff of Scheveningen Radio who were responsible for installing and maintaining the transmitting systems. Thanks are also due for the assistance and facilities given by the Superintendent and technical staff at Lerwick Meteorological Observatory. Acknowledgment is also made to the Ministry of Transport for permission to use its coastguard stations and for the valuable help given by the coastguard officers.

The author gratefully acknowledges the assistance given in this work by his many colleagues of the Research Department, British Broadcasting Corporation.

Finally, the author wishes to express his thanks to the Director of Engineering of the British Broadcasting Corporation for permission to publish the paper.

6. References

1. Documents of the C.C.I.R. Xth Plenary Assembly, Recommendation 370, Geneva 1963, Volume II, p. 36.
2. R. G. Flavell and J. A. Lane, "The application of potential refractive index in tropospheric wave propagation", *J. Atmos. Terrest. Phys.* **24**, pp. 47–56, 1962.
3. R. G. Flavell, "Further radio-meteorological analysis using potential refractive index", *J. Atmos. Terrest. Phys.* **26**, pp. 44–49, 1964.

Manuscript received by the Institution on 28th April 1965. (Paper No. 1006/T33.)

# of current interest . . .

Research Contract for Computer Typesetting

A research contract worth £95,000—the first to be placed with a university by the Ministry of Technology —has been awarded to the University of Newcastle-upon-Tyne for a 3–4 year programme of work on the application of electronic digital computers to type composition and printing.

One of the objects of the work is to provide the printing industry with a series of adaptable computer programs which will perform all the operations of copy preparation, editing and actual type composition. An equally important aim is to provide a wholly automatic system of preparing material from computers for publication in an improved, readable form without running the risk of introducing errors by human data handling.

This work should reduce book production costs and shorten the time taken in the publication of new work. This is particularly important in the academic field where technical innovation is proceeding rapidly and where revision and the introduction of new material is hampered by limited demand and rising costs.

The new processes are likely to have an effect on the working habits of everyone concerned with publication from authors to distributors of printed matter. For this reason the work is to be carried out in the fullest collaboration with unions, printers and publishers.

The first two years will be spent on improving existing programs and in investigating keyboard input instruments. A fast photocomposing machine will be installed later which will offer an experimental service for selected printing tasks, particularly those from computing laboratories and organizations processing statistics.

Transistors in G.P.O. Telephone Network

The British Post Office is increasing its use of transistors for medium and long distance links in the inland telephone network. Previously these links required valve amplifiers at intervals of between 3 and 6 miles, and reliable power supplies and well constructed buildings sited near the cable routes.

The use of transistor amplifiers has reduced size and power requirements to such an extent that amplifiers can now be housed in footway boxes at the roadside and be energized by power fed to them over the cable using safe values of current.

Several 300-circuit line systems using 0·174 in. diameter coaxial cable are already in use and others with a capacity of 960-circuits will shortly be ready. A few 12-circuit carrier systems using two unloaded audio pairs, are also in use. By early 1965 some 13 transistorized line systems were operating and approximately 200 are planned to be in use by 1969.

For distances between 15 and 40 miles pulse code modulation—p.c.m.—systems have been developed. These use wires in cables of a type already existing in large quantities. Using only four wires to provide 23 circuits such systems promise greater use of existing underground plant: without pulse code modulation systems the same four wires would provide only two circuits. The principle of p.c.m. is that speech amplitudes are coded at the sending end into a sequence of pulses. These are transmitted over the line to the receiving terminal at which speech signals are decoded. Repeaters employing transistors and housed in watertight containers sited in manholes along the route are energized from the terminals, using safe current values, via the same wires used to bear the coded speech channels.

Since at the repeaters and receiving terminals it is necessary to recognize only the presence or absence of pulses, p.c.m. systems can be made very resistant to the disturbing effects of crosstalk and noise.

The features make p.c.m. systems very suitable for use in urban areas, and trials are being conducted on three routes.

Research into Circuit Techniques

The Department of Electrical Engineering in the University of Newcastle upon Tyne has been awarded a grant of £19,650 by the Science Research Council in support of work on the synthesis and sensitivity of active and passive circuits under the general direction of Dr. A. G. J. Holt (Associate Member). In association with an earlier grant, this brings the investment in this topic to £24,500. In addition to the special equipment which will be required, provision has been made for the appointment of a Research Fellow.

The introduction of micro-circuitry and the development of thin film techniques presents the problem of designing circuits without inductances, but which have the same electrical performance as the more orthodox circuits containing coils.

As a related topic, a study will also be made of the reduction of sensitivity of circuits to errors brought about by variations in component values. A closer understanding of the problems could lead to cheaper circuits if it enables wider tolerance components to be used.